

# Study of the Sensitivity of CMS to the Lepton Flavour Violating Neutrinoless $\tau$ Decay $\tau \rightarrow \mu\mu\mu$

Von der Fakultät für Mathematik, Informatik und Naturwissenschaften  
der RWTH Aachen University zur Erlangung des akademischen Grades  
eines Doktors der Naturwissenschaften genehmigte Dissertation

vorgelegt von

Diplom-Physiker Manuel Giffels  
aus Würselen

Berichter: Universitätsprofessor Dr. rer. nat. Achim Stahl  
Universitätsprofessor Dr. rer. nat. Michael Krämer

Tag der mündlichen Prüfung: 27. Februar 2009

Diese Dissertation ist auf den Internetseiten der Hochschulbibliothek  
online verfügbar.

# Zusammenfassung

Der weltgrößte Proton-Proton-Speicherring, der Large Hadron Collider (LHC) am Forschungszentrum CERN in der Nähe von Genf, wird im Sommer 2009 seinen Betrieb aufnehmen. Bei einer Schwerpunktsenergie von 14 TeV beträgt der totale Wirkungsquerschnitt für die Produktion von  $\tau$ -Leptonen im CMS-Experiment (Compact Muon Solenoid) etwa  $140 \mu\text{b}$ . Unter Annahme einer integrierten Luminosität von mindestens  $10 \text{ fb}^{-1}$  pro Jahr, die während der Phase geringer Luminosität von  $\mathcal{L} = 2 \times 10^{33} \text{ cm}^{-2} \text{ s}^{-1}$  erwartet wird, werden ungefähr  $10^{12}$   $\tau$ -Leptonen pro Jahr erzeugt. Damit bietet der LHC hervorragende Voraussetzungen für die Untersuchung von neutrinolessen und damit leptonzahlverletzenden  $\tau$ -Zerfällen.

Bereits seit der experimentellen Entdeckung der Neutrinoszillationen ist bekannt, dass die Erhaltung der Leptonfamilienzahl nicht streng gelten kann. Dies hat natürlich einige Auswirkungen auf das Bild der Leptonen im Standard Model, die Neutrinos haben eine von Null verschiedene Masse, wodurch sich die Masseneigenzustände von den schwachen Eigenzuständen unterscheiden und eine ähnliche Mischungsmatrix wie im Quarksektor einzuführen ist. Dies macht auch das Auftreten von neutrinolessen  $\tau$ -Zerfällen im Rahmen des Standard Models möglich. Allerdings sind diese Zerfälle, wie auch der  $\tau \rightarrow \mu\mu\mu$  Zerfall, durch den GIM-Mechanismus sehr stark unterdrückt ( $\mathcal{B}_r \sim 10^{-50}$ ). Damit würde ein Nachweis dieses Zerfalls in den mit heutigen Experimenten zugänglichen Regionen ein eindeutiges Zeichen für die Existenz neuer Physik sein. Eine große Anzahl von Modellen, die Physik jenseits des Standard Models postulieren, sagen dabei teils Verzweigungsverhältnisse für den  $\tau \rightarrow \mu\mu\mu$  Zerfall nahe der aktuellen Ausschlußgrenze von  $\mathcal{B}_r(\tau \rightarrow \mu\mu\mu) < 3.2 \cdot 10^{-8}$  voraus. Der  $\tau \rightarrow \mu\mu\mu$  Zerfall bietet also eine interessante Alternative, um nach neuer Physik zu suchen.

Nach einer kurzen Vorstellung einiger dieser Modelle, sowie des Large Hadron Colliders und des CMS-Experiments, werden die in dieser Arbeit verwendeten Monte Carlo Simulationstechniken beschrieben. Im Anschluß daran werden die, für die Untersuchung des  $\tau \rightarrow \mu\mu\mu$  Zerfalls notwendigen Rekonstruktionsalgorithmen und Trigger behandelt. Eine Verbesserung der Rekonstruktion von  $\tau \rightarrow \mu\mu\mu$  Ereignissen unter Verwendung einer alternativen Identifikation von Myonen, sowie eine mögliche Steigerung der Triggereffizienz durch einen dedizierten  $\tau \rightarrow \mu\mu\mu$  Trigger werden dabei detailliert erörtert. Im weiteren Verlauf dieser Arbeit wird eine Monte Carlo Studie des Einfluss verschiedener Modelle auf die Rekonstruktion der  $\tau \rightarrow \mu\mu\mu$  Ereignisse vorgestellt, sowie eine mögliche Differenzierbarkeit der Modelle diskutiert. Die Ergebnisse dieser Studie wurden dabei in enger Zusammenarbeit mit der Theorie erzielt. Im letzten Teil dieser Arbeit werden eingehend die Produktion von  $\tau$ -Leptonen bei CMS, mögliche Untergründe dieser Studie, die Signalselektion, sowie die Bestimmung der Sensitivität beschrieben.

# Abstract

The word largest proton-proton collider, the Large Hadron Collider (LHC), which was built up at CERN in the near of Geneva, will start its operation in summer 2009. The total  $\tau$  lepton production cross-section for the CMS experiment, at a center-of-mass energy of 14 TeV, is about  $140 \mu\text{b}$ . Assuming an integrated luminosity of  $10 \text{ fb}^{-1}$  per year, which is expected to be reached in the low luminosity phase of  $\mathcal{L} = 2 \times 10^{33} \text{ cm}^{-2} \text{ s}^{-1}$ , about  $10^{12} \tau$  leptons are produced in total. This copious  $\tau$  production at the LHC provides an excellent potential for the search of neutrinoless and therefore lepton flavour violating  $\tau$  decays.

It is already known since the experimental discovery of neutrino oscillations, that the conservation law of the lepton family number is not strict. The neutrino oscillations have dramatic consequences for the picture of leptons in the Standard Model. The neutrinos become massive particles, the mass eigenstates differ from the flavour eigenstates and a mixing matrix similar to the CKM matrix in the quark sector is introduced. The neutrino mixing also gives rise to neutrinoless  $\tau$  decays in the Standard Model. However, the  $\tau \rightarrow \mu\mu\mu$  decay is heavily suppressed by the GIM mechanism ( $\mathcal{B}_r \sim 10^{-50}$ ) and therefore not measurable with current experiments. The observation of such a lepton flavour violating  $\tau$  decay will be an unambiguous sign of new physics beyond the Standard Model. There are a large number of models beyond the Standard Model which give rise to the lepton flavour violating  $\tau \rightarrow \mu\mu\mu$  decay, partially with branching ratios close to the current experimental upper limit of  $\mathcal{B}_r(\tau \rightarrow \mu\mu\mu) < 3.2 \cdot 10^{-8}$ . The  $\tau \rightarrow \mu\mu\mu$  decay is an alternative option in search of new physics.

After a brief introduction of some of these models, the Large Hadron Collider, as well as the CMS experiment, and the Monte Carlo simulation methods used in this thesis are described. Furthermore the reconstruction algorithms and trigger paths, which are required for the study of the  $\tau \rightarrow \mu\mu\mu$  decay, are presented. A possible improvement of the reconstruction of  $\tau \rightarrow \mu\mu\mu$  events using an alternative muon identification, as well as a possible increase of the trigger efficiency using a dedicated  $\tau \rightarrow \mu\mu\mu$  trigger algorithm are pointed out. Moreover a Monte Carlo study of the influence of different models on the reconstruction of  $\tau \rightarrow \mu\mu\mu$  events is presented and also a possible separation of the models is discussed. The results of this study have been achieved in close collaboration with the theory department. In the last part of this thesis, the production of  $\tau$  leptons in CMS, possible backgrounds of this study, the signal selection and the determination of the sensitivity are described.

# Contents

<b>1</b>	<b>Introduction</b>	<b>1</b>
1.1	The Standard Model of Particle Physics	1
1.2	Lepton Flavour Violation in the Standard Model	2
1.3	LFV in Models Beyond the Standard Model	4
1.3.1	Supersymmetric Model with See-Saw Mechanism	5
1.3.2	Supersymmetric Model with $R$ -Parity Violation	5
1.3.3	Littlest Higgs Model with $T$ -Parity	6
1.3.4	Topcolour-assisted Technicolour	7
1.3.5	Models with Doubly-Charged Higgs Bosons	8
<b>2</b>	<b>LHC and the CMS Experiment</b>	<b>9</b>
2.1	The Large Hadron Collider	9
2.2	The Compact Muon Solenoid	12
2.2.1	The Silicon Pixel Detector	13
2.2.2	The Silicon Strip Detector	14
2.2.3	The Electromagnetic Calorimeter	15
2.2.4	The Hadron Calorimeter	17
2.2.5	The Solenoid	18
2.2.6	The Muon System	18
<b>3</b>	<b>Monte Carlo Simulation</b>	<b>21</b>
3.1	Monte Carlo Techniques	21
3.2	The Monte Carlo Production Chain	22
3.2.1	Event Generation	23
3.2.2	Detector Simulation	23
3.2.3	Digitization	23
3.2.4	Trigger	24
3.2.5	Reconstruction	24
3.3	The LHC Computing Grid	24
3.4	Software Tools	26
3.4.1	Grid Analysis Tool	26
3.4.2	Job Monitor	27
3.4.3	Official Tools	28
<b>4</b>	<b>Reconstruction</b>	<b>29</b>
4.1	Track Reconstruction	29
4.1.1	Hit Reconstruction	30

4.1.2	Track Seeding . . . . .	30
4.1.3	Pattern Recognition . . . . .	30
4.1.4	Trajectory Cleaner . . . . .	31
4.1.5	Track Fitting and Smoothing . . . . .	31
4.1.6	Performance . . . . .	31
4.2	Secondary Vertex Reconstruction . . . . .	32
4.2.1	Kalman Vertex Fitter . . . . .	33
4.2.2	Adaptive Vertex Fitter . . . . .	33
4.2.3	Performance . . . . .	34
4.3	Muon Reconstruction and Identification . . . . .	34
4.3.1	Local Reconstruction . . . . .	35
4.3.2	Standalone Muon Reconstruction . . . . .	37
4.3.3	Global Muon Reconstruction . . . . .	38
4.3.4	Performance . . . . .	38
4.4	Alternative Muon Identification . . . . .	39
4.4.1	Track Propagation . . . . .	40
4.4.2	Energy Deposition in the ECAL . . . . .	41
4.4.3	Energy Deposition in the HCAL . . . . .	41
4.4.4	Energy Deposition in the HO . . . . .	42
4.4.5	Number of Reconstructed Muon Segments . . . . .	43
4.4.6	Likelihood Ratio . . . . .	43
4.5	Trigger . . . . .	45
4.5.1	Level 1 Trigger . . . . .	45
4.5.2	High Level Trigger . . . . .	46
<b>5</b>	<b>Implementation of <math>\tau \rightarrow \mu\mu\mu</math> in the Event Generator</b>	<b>49</b>
5.1	Adding the Decay $\tau \rightarrow \mu\mu\mu$ . . . . .	49
5.2	The Matrix Element . . . . .	50
5.3	Treatment of the $\tau$ Polarization . . . . .	53
5.4	Implementation into CMSSW . . . . .	55
5.4.1	Implementation of the $\tau$ Polarization . . . . .	55
5.4.2	Implementation of the Matrix Element . . . . .	56
5.5	Results for Various Models . . . . .	57
5.5.1	Influence on the Detection Power . . . . .	58
<b>6</b>	<b>The Decay <math>\tau \rightarrow \mu\mu\mu</math></b>	<b>63</b>
6.1	The Production of $\tau$ Leptons at the LHC . . . . .	63
6.2	Signal and Background Datasets . . . . .	64
6.3	Study on Generator Level . . . . .	67
6.4	Monte Carlo Truth Matching . . . . .	72
6.5	Selection of $\tau \rightarrow \mu\mu\mu$ Signal Events . . . . .	73
6.5.1	Skimming of Background Samples . . . . .	73
6.5.2	Preselection . . . . .	77
6.5.3	Event Selection and Background Rejection . . . . .	77
6.6	The Remaining Background Event . . . . .	84
6.7	Uncertainties of the Study . . . . .	85
6.8	Determination of an Upper Limit . . . . .	88

CONTENTS	iii
<b>7 Summary and Outlook</b>	<b>93</b>
<b>A Physics Add-Ons</b>	<b>95</b>
A.1 CMSSW Configurations . . . . .	95
A.1.1 $\tau \rightarrow \mu\mu\mu$ Implementation . . . . .	95
A.2 Muon Resolution . . . . .	96
A.3 Limit Calculation . . . . .	97
<b>Bibliography</b>	<b>103</b>
<b>Acknowledgment</b>	<b>109</b>



# Chapter 1

## Introduction

### 1.1 The Standard Model of Particle Physics

According to the current state of knowledge, the Standard Model of particle physics consists of 12 fermions with spin- $1/2$ , which represent the matter. These 12 fermions can be divided into 6 quarks and 6 leptons, which are grouped into three so-called families, with each family consisting of two quarks and two leptons. Fermions of the second and third family are heavier copies of the first family fermions, they are unstable and decay into fermions of the first family. Therefore, all stable matter which surrounds us consists of fermions of the first family. The existence of the apparently “needless” second and third family is one of the as-yet unsolved mysteries of particle physics.

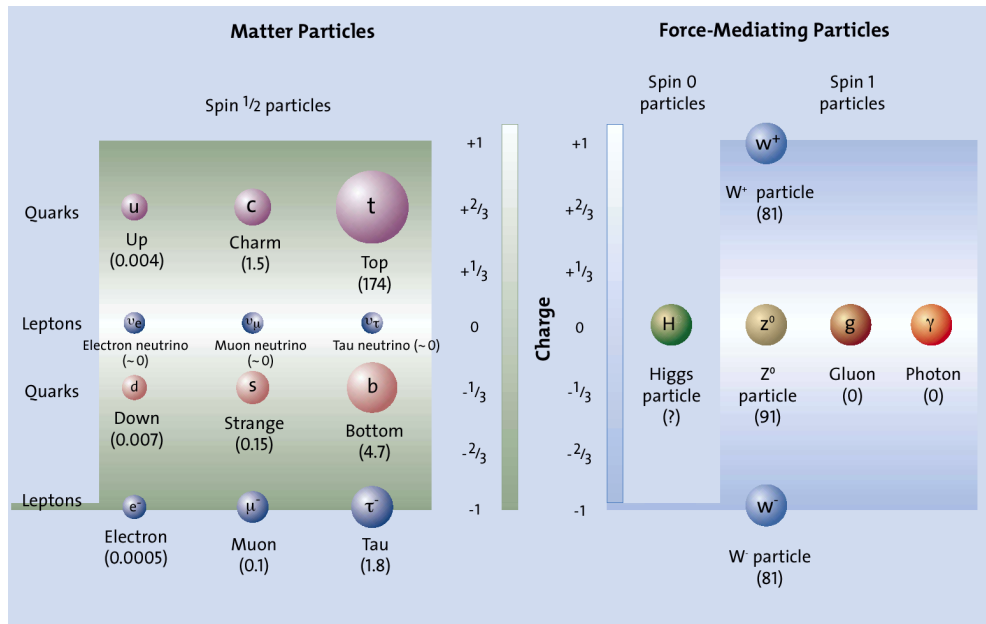


**Figure 1.1:** Particles of the Standard Model and their masses in GeV. [1]

The interactions in the Standard Model are described by quantum field theories. The requirement of local gauge invariance automatically leads to the existence of force mediating gauge fields. The quanta of these gauge fields are bosons carrying an integer

spin. These bosons are the mediators of the 3 forces described by the Standard Model.

- electromagnetic interaction,
- weak interaction,
- strong interaction.

The mediator of the electromagnetic interaction is the photon ( $\gamma$ ), the mediators of the weak interaction are the  $W^{+}$ -,  $W^{-}$ - and the  $Z^0$ -boson, and the strong interaction is mediated by 8 gluons.

Symmetry plays an important role in physics, so mathematically the Standard Model is described as a gauge theory with a combined symmetry group  $SU(3)_C \times SU(2)_L \times U(1)_Y$ . The electromagnetic and the weak interaction are unified in the GSW (Glashow-Salam-Weinberg) theory of the electroweak interaction. It is desirable to unify all forces in a Grand Unified Theory (GUT), but currently there is no experimental evidence for a single unified field describing all forces.

Beside the 12 bosons mediating the forces, there is one additional boson, the scalar Higgs boson. Local gauge invariance requires massless gauge bosons, therefore the Higgs field was introduced into the Standard Model to create the masses of the heavy gauge bosons, mediating the weak interaction, by a spontaneous symmetry breaking. Additionally, it can explain the fermion masses through its Yukawa couplings. The Higgs boson is the only still undiscovered particle in the Standard Model of particle physics.

### Physics Beyond the Standard Model

The Standard Model has been tested with high precision up to present reachable energies. There are no significant deviations between the theoretical predictions and the experimental measurements. But nevertheless an extension of the model seems to be necessary. The fourth known force in nature, gravity is not included in the Standard Model. Gravity is admittedly negligible at current experiment energies, but it plays an important role in cosmology and for the genesis of the universe. Furthermore, the origin of mass is opaque. All fermion and boson masses are free parameters in the Standard Model. Additionally, there is no explanation for the dark matter in the universe, which can be astronomically observed. According to the current state of knowledge, the universe only consists of matter, which cannot be explained by the observed asymmetry between matter and antimatter in the Standard Model. To solve these open questions an extension of the current model seems to be reasonable.

## 1.2 Lepton Flavour Violation in the Standard Model

According to the Noether's theorem [2] any symmetry of the action in a physical system leads to a corresponding conservation law. Beside fundamental conserved quantities having a corresponding symmetry, like for example energy, momentum and charge, some conserved quantities have been introduced to the Standard Model without having

an obvious corresponding symmetry. They have been introduced to account for the absence of some reactions which are in principle allowed in the Standard Model. Such a artificially conserved quantity is the lepton number. The law of conversation of lepton number was proposed in 1953 by Konopinski and Mahmoud [3] to introduce a simple rule to determine which reactions are allowed and which are not. The lepton number  $L = +1$  is assigned to the  $e^-$ ,  $\mu^-$ ,  $\tau^-$ ,  $\nu_e$ ,  $\nu_\mu$  and  $\nu_\tau$ , and the lepton number  $L = -1$  to their antiparticles. All other particle have a lepton number of zero. For example the reaction

$$\nu_e + n \rightarrow p^+ + e^-$$

is allow, whereas

$$\bar{\nu}_e + n \rightarrow p^+ + e^-$$

is not possible.

But the conservation law of the lepton number is not enough to explain why for example the decay

$$\tau^- \rightarrow \mu^- \gamma$$

has been never observed. The solution is to require that the lepton number of each family is conserved separately. This results in the law of conservation of lepton family number [4].

Today, it is known that the conservation law of the lepton family number is not strict. Already in the late sixties, Davis observed a deficit in the solar neutrino flux in a neutrino experiment at the Homestake mine [5]. One of the explanations is an oscillation between the neutrino flavours, since the Homestake experiment was only sensitive to electron neutrinos. Meanwhile the theory of neutrino oscillation is experimentally confirmed by the SNO (Sudbury Neutrino Observatory) experiment [6], which is able to measure the total solar neutrino flux as well as the flux of solar electron neutrinos. The results are showing that there is a deficit of electron neutrinos originated by the sun, but the total flux of solar neutrinos is consistent to the expectations of the solar model. Meanwhile many experiments have confirmed the existence of neutrino oscillations. For example, neutrino oscillations have been measured with atmospheric neutrinos in the Super Kamiokande experiment [7]. The results support the prediction of a  $\nu_\mu - \nu_\tau$  oscillation.

The neutrino oscillations have enormous consequences for the picture of leptons in the Standard Model. The conservation law of the lepton family number is not compatible with the observed neutrino oscillations, the neutrinos become massive particles and a mixing matrix, analogue to the CKM matrix<sup>1</sup> in the quark sector, has to be introduced. The mass eigenstates  $\nu_1$ ,  $\nu_2$  and  $\nu_3$  differ from the flavour eigenstates  $\nu_e$ ,  $\nu_\mu$  and  $\nu_\tau$ . The relation between them is given by equation 1.1.

$$\begin{pmatrix} \nu_e \\ \nu_\mu \\ \nu_\tau \end{pmatrix} = \begin{pmatrix} U_{e1} & U_{e2} & U_{e3} \\ U_{\mu 1} & U_{\mu 2} & U_{\mu 3} \\ U_{\tau 1} & U_{\tau 2} & U_{\tau 3} \end{pmatrix} \cdot \begin{pmatrix} \nu_1 \\ \nu_2 \\ \nu_3 \end{pmatrix} \quad (1.1)$$

---

<sup>1</sup>Cabibbo-Kobayashi-Maskawa matrix, quark mixing matrix.

The unitary matrix  $U$  is the neutrino mixing matrix or PMNS<sup>2</sup> matrix. The neutrino mixing also gives rise to lepton flavour violation in charged lepton sector of the Standard Model. In figure 1.2 the Standard Model Feynman diagram for the lepton flavour violating decay  $\tau \rightarrow \mu\mu\mu$  is depicted.

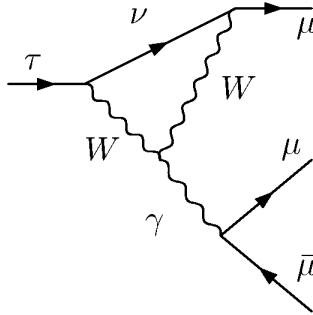


**Figure 1.2:** Feynman diagram for the lepton flavour violating decay  $\tau \rightarrow \mu\mu\mu$  in the Standard Model with massive neutrinos [8].

However there is an almost complete cancellation of the amplitudes coming from the 3 contributing indistinguishable diagrams (namely  $\nu_1$ ,  $\nu_2$  and  $\nu_3$  in the loop), due to the unitarity of the mixing matrix and the resulting GIM mechanism. The rates in the Standard Model are proportional to  $(m_\nu/m_W)^4$ . The corresponding branching ratio is therefore very low, roughly in the order of  $10^{-50}$  [9], which can obviously not be observed in current experiments. The observation of such a lepton flavour violating  $\tau$  decay will be an unambiguous sign of new physics beyond the Standard Model.

### 1.3 LFV in Models Beyond the Standard Model

There are a large number of models beyond the Standard Model which give rise to lepton flavour violation in the reach of current and future experiments. Mass-dependent couplings prefer the occurrence of lepton flavour violation in the third generation with respect to lighter leptons. The sensitivity to new physics is different for  $\tau \rightarrow lll$  and  $\tau \rightarrow l\gamma$ . The decay channel  $\tau \rightarrow l\gamma$  has in general a better sensitivity, if the decay  $\tau \rightarrow lll$  is mediated by a photon exchange ( $\tau l\gamma$  vertex), since a diagram with a further  $yll$  vertex is suppressed by a factor of  $\alpha$  (i.e. see figure 1.2). However, if the mediation is done by a new heavy particle, the  $\tau \rightarrow lll$  decay channel can be favoured [8].

To search for lepton flavour violating  $\tau$  decays at the Large Hadron Collider (LHC), muons in final state provide a clean signature. But nonetheless the decay  $\tau \rightarrow \mu\gamma$  is difficult to observe at the LHC, due to the backgrounds coming from  $\pi^0$  decays and the more stringent trigger thresholds for single muons. So it is reasonable to focus on the decay  $\tau \rightarrow \mu\mu\mu$  in this study.

Therefore, the following introduction is focussed on models where the  $\tau \rightarrow \mu\mu\mu$  decay is mediated by a new heavy particle.

<sup>2</sup>Pontecorvo-Maki-Nakagawa-Sakata matrix

### 1.3.1 Supersymmetric Model with See-Saw Mechanism

The Minimal Supersymmetric Standard Model (MSSM) is a possible extension of the Standard Model. The Supersymmetry (SUSY) is a symmetry between bosons and fermions. The MSSM contains beside the well-known Standard Model particles also their supersymmetric partners [10]. A detailed introduction into Supersymmetry can be found in [11].

In the Standard Model, neutrinos are given mass through the Yukawa coupling of the fermions to the Higgs boson. In principle the strength of these couplings are free parameters of the Standard Model, but there is no explanation for the large difference between the couplings to neutrinos and to charged leptons. The see-saw mechanism, which gives an explanation for the tiny neutrino masses, introduces heavy right-handed sterile neutrinos, which are assumed to be Majorana particles. The mass scale of these new particles is of the order of  $10^{14}$  GeV. The see-saw mechanism can be also used in the MSSM to generate the neutrino masses [8, 10].

Depended on the model parameters, lepton flavour violation can occur in the couplings of the neutral Higgs bosons. This effect is strongly enhanced for large  $\tan \beta$ . The contributing Feynman diagrams are depicted in figure 1.3. A prediction of the branching ratio of the  $\tau \rightarrow \mu\mu\mu$  decay for specific assumptions on the model parameters is

$$\mathcal{B}_r(\tau \rightarrow \mu\mu\mu) \simeq 1 \times 10^{-7} \left( \frac{\tan \beta}{60} \right)^6 \times \left( \frac{100 \text{ GeV}}{m_A} \right)^4.$$

A detailed description of the calculation and the assumed model parameters can be found in [12].

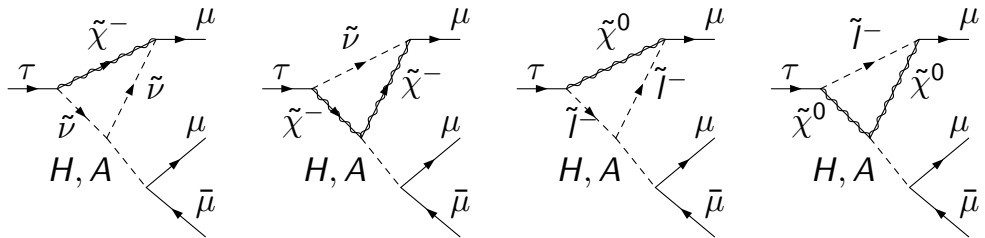


**Figure 1.3:** Contributing Feynman diagrams to the decay  $\tau \rightarrow \mu\mu\mu$  in a SUSY model with See-Saw mechanism [8].

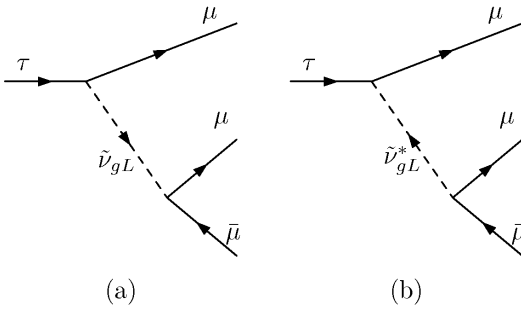
### 1.3.2 Supersymmetric Model with *R*-Parity Violation

The discrete *R*-parity has been introduced into Supersymmetry to avoid baryon number and lepton number violating terms in the Superpotential, which can contribute to the decay of the proton which has not been observed. Additionally, it guarantees that the lightest supersymmetric particle is stable and therefore a good candidate for dark matter.

$$R\text{-parity} \quad R_p = (-1)^R = \begin{cases} +1 & \text{for Standard Model particles (R-even)} \\ -1 & \text{for supersymmetric particles (R-odd)} \end{cases}$$

The  $R$  is defined as  $R = 3B + L + 2S$ , with  $B$  being the baryon number,  $L$  the lepton number and  $S$  the spin of the particle.

In supersymmetric models with  $R$ -parity violation which are still possible with respect to the present experimental bounds, an additional non-diagonal Yukawa coupling between the charged leptons and sneutrinos allows lepton flavour violation in the charged lepton sector [8, 10, 13]. The contributing Feynman diagram to the decay  $\tau \rightarrow \mu\mu\mu$  is depicted in figure 1.4.



(plus diagrams with the muons crossed.)

**Figure 1.4:** Contributing Feynman diagrams to the decay  $\tau \rightarrow \mu\mu\mu$  in a SUSY model with  $R$ -parity violation [8].

### 1.3.3 Littlest Higgs Model with $T$ -Parity

The Littlest Higgs model is an alternative approach to generate the electroweak symmetry breaking and to solve the little hierarchy problem [14]. The Little Higgs models have a problem with large anomalous couplings due to new “mirror” particles at the TeV scale. To avoid problems with the LEP electroweak precision measurements, a discrete  $T$ -parity has been introduced. Therefore, the “mirror” particles are exchanged only in loops and tree-level corrections to electroweak observables are forbidden. The Littlest Higgs model introduces additional gauge groups and fermion multiplets, which allow flavour changing in loops of  $T$ -odd particles [15]. Example Feynman diagrams contributing to the decay  $\tau \rightarrow \mu\mu\mu$  are depicted in figure 1.5.

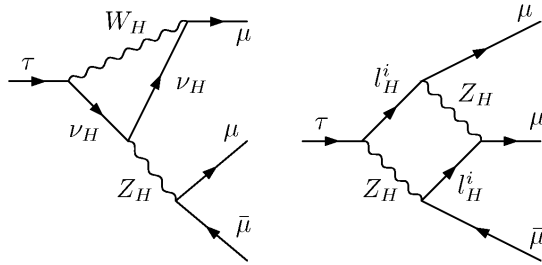


**Figure 1.5:** Contributing Feynman diagrams to the decay  $\tau \rightarrow \mu\mu\mu$  in the Littlest Higgs Model with  $T$ -parity [8].

A prediction for the expected branching ratio for the decay  $\tau \rightarrow \mu\mu\mu$  has been calculated in [16]. The expected branching ratio depends on the scale  $f$ . For  $f = 500$  GeV,

the expected branching ratio is

$$\mathcal{B}_r(\tau \rightarrow \mu\mu\mu) = 3 \times 10^{-8},$$

and for  $f = 1000 \text{ GeV}$  the expected branching ratio is

$$\mathcal{B}_r(\tau \rightarrow \mu\mu\mu) = 7 \times 10^{-10}.$$

### 1.3.4 Topcolour-assisted Technicolour

Technicolour is a dynamical model of electroweak symmetry breaking. This model introduces a QCD-like force at a higher mass scale and a new set of particles, the so-called techniquarks. The electroweak symmetry is broken by condensate analogous to mesons in the QCD. Three of the Goldstones bosons, the so-called technipions, become the longitudinal components of the  $W$  and  $Z$  [17, 18].

Topcolour is new QCD-like interaction which couples preferentially to the third generation of quarks: an additional strong  $U(1)$  interaction, giving rise to a non-universal  $Z'$ , which excludes the formation of  $b$ -quark condensates. Topcolour is also an alternative model to describe the electroweak symmetry breaking in a dynamical way due to a condensate of top quarks [18, 19].

Both models are combined together as Topcolour-assisted Technicolour (TC2) to solve the shortcomings of each other. These models typically predict large non-universal couplings to the third generation mediated by the non-universal  $Z'$  [20]. The top condensate, the so-called top-pion, can also mediate lepton flavour violation [21]. The contributing diagrams to the decay  $\tau \rightarrow \mu\mu\mu$  in TC2 models are depicted in figure 1.6 [8].

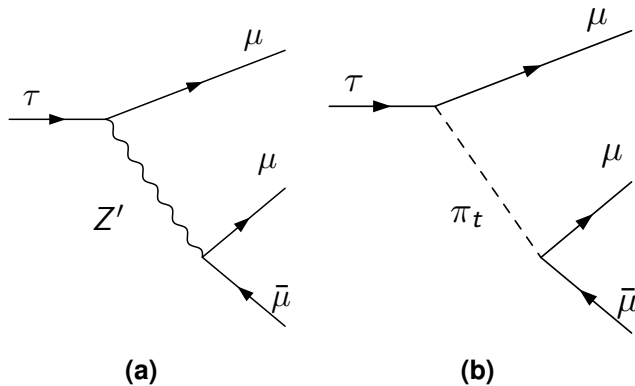


**Figure 1.6:** Contributing Feynman diagrams to the decay  $\tau \rightarrow \mu\mu\mu$  in the Topcolour-assisted Technicolour model [8].

The expected branching ratio of the  $\tau \rightarrow \mu\mu\mu$  decay, according to [20], for the  $Z'$  mediated lepton flavour violation is

$$\mathcal{B}_r(\tau \rightarrow \mu\mu\mu) = 8.7 \times 10^{-7}.$$

### 1.3.5 Models with Doubly-Charged Higgs Bosons

Models with doubly-charged Higgs bosons can also give rise to lepton flavour violation resulting in the decay  $\tau \rightarrow \mu\mu\mu$  through Feynman diagrams such as shown in figure 1.7. Two models have been discussed in the context of lepton flavour violation in  $\tau$  decays in [22]. The Higgs Triplet model [23] and the Zee-Babu model [24, 25].

Those models are extension of the Standard Model with doubly-charged Higgs bosons. They give Majorana masses to the neutrinos without the introduction of right-handed neutrinos. As depicted in figure 1.7, the lepton flavour violation occurs by a tree-level exchange of a doubly-charged Higgs boson [8, 22].

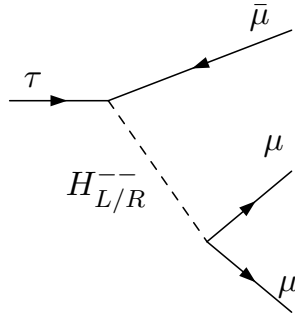


**Figure 1.7:** Contributing Feynman diagram to the decay  $\tau \rightarrow \mu\mu\mu$  in models with doubly-charged Higgs bosons [8].

The expected branching ratios for the  $\tau \rightarrow \mu\mu\mu$  decay, according to [22], is in the order of

$$\mathcal{B}_r(\tau \rightarrow \mu\mu\mu) \simeq 10^{-7} \rightarrow 10^{-9}.$$

# Chapter 2

## LHC and the CMS Experiment

### 2.1 The Large Hadron Collider

The Large Hadron Collider (LHC) was installed during the last eight years in the 27 km long tunnel of the former Large Electron Positron Collider (LEP) at CERN<sup>1</sup> in Geneva (Switzerland). The LHC was already approved in 1994 by the CERN council to be the successor of the LEP experiment, which was switched off in November 2000. Therefore, most of the already existing infrastructure could be used also for the LHC (see figure 2.1). The LHC is a proton-proton collider with a center-of-mass energy up to 14 TeV and a design luminosity of  $\mathcal{L} = 10^{34} \text{ cm}^{-2} \text{ s}^{-1}$ . For this reason it is currently the world's best collider, which will provide access to energies never reached before by any other experiment. The LHC will have its first proton collisions in 2009.

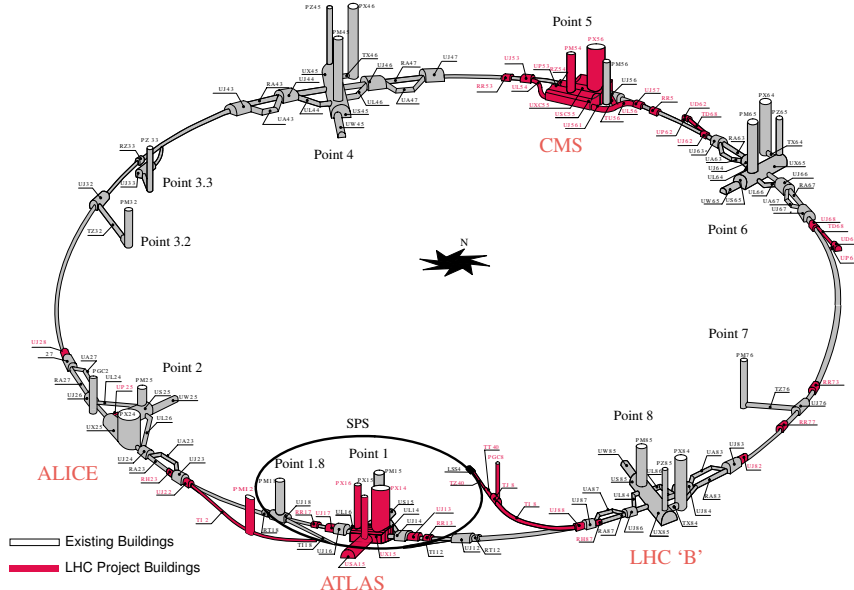


**Figure 2.1:** The Large Hadron Collider with its four large experiments ALICE, ATLAS, CMS and LHCb [26].

After a commissioning phase the LHC will be ramped up to an initial luminosity of

<sup>1</sup>CERN is an acronym for Conseil Européenne pour la Recherche Nucléaire and today it is well-known as European Organization for Nuclear Research.

$\mathcal{L} = 10^{32} \text{ cm}^{-2} \text{ s}^{-1}$  followed by a low luminosity phase ( $\mathcal{L} = 2 \times 10^{33} \text{ cm}^{-2} \text{ s}^{-1}$ ). A high luminosity phase with  $\mathcal{L} = 10^{34} \text{ cm}^{-2} \text{ s}^{-1}$  will start at a later date and last for a period of several years.

Beside the acceleration and storage of protons it is also foreseen to operate LHC with heavy ions (i.e. lead) at a later date. The parameters for both scenarios are very different, so the following section is focussed on the operation of LHC with protons.

The LHC injection chain starts at the linear accelerator LINAC2, where the protons will be accelerated to 50 MeV. Next step is the Proton Synchrotron Booster (PSB), which accelerates the protons to 1.4 GeV. Followed by the Proton Synchrotron (PS) (acceleration to 25 GeV) and the Super Proton Synchrotron (SPS) (acceleration to 450 GeV). The final acceleration of the protons to the nominal beam energy of 7 TeV will be done in the LHC. Therefore superconducting radio frequency cavities are used to increase the proton energy by 0.5 MeV per turn. 1232 superconducting dipole magnets are responsible to keep the protons on the circular path. To bend 7 TeV protons a field of 8.33 T is necessary in contrast to 0.535 T for protons having an energy of 450 GeV. So the dipoles have to be operated over a large range in the magnetic field. The nominal current of a dipole operated at 7 T is 11870 A. Both dipole magnets and cavities are cooled down by super fluid helium to an operation temperature of 1.6 K.

The two beam lines of LHC are filled with 2808 bunches each. A bunch contains  $1.15 \times 10^{11}$  protons. The bunch spacing is 24.95 ns, which corresponds to a interaction rate of about 40 MHz. The minimum total time needed to fill the LHC is about 16 minutes. The following ramp up to a beam energy of 7 TeV takes approximately additional 20 minutes. The ramp down of the dipoles for a new injection, after the beam was dumped, takes also around 20 minutes. Assuming a 10 minutes check of the main systems, the minimum turnaround time, the time between two physics runs, is around 70 minutes. Experiences from HERA<sup>2</sup> have shown, that there is roughly a factor of 6 between the theoretically and real turnaround time. The luminosity during a physics run is not constant, mainly due to the beam collisions. The luminosity life time, the time for a physics run, is expected to be 14.9 hours [27–31].

There are four interaction points foreseen for bunch crossings. At these points four main experiments of the LHC are located (see figure 2.1).

- ALICE (A Large Ion Collider Experiment) [32],
- ATLAS (A Toroidal LHC ApparatuS) [33],
- CMS (Compact Muon Solenoid) [34],
- LHCb (Large Hadron Collider Beauty Experiment) [35].

ALICE is a dedicated heavy ion experiment. The peak luminosity is  $\mathcal{L} = 10^{27} \text{ cm}^{-2} \text{ s}^{-1}$  for nominal  $Pb - Pb$  collisions with a beam energy of 2.76 TeV per nucleon. The major goal of ALICE is the observation of the quark-gluon-plasma. The reachable energy densities at LHC should be larger than the deconfinement threshold, so it will be possible to probe for quark-gluon-plasma in its asymptotically free “ideal gas” form. Therefore heavy ion collisions at the LHC provide an excellent environment for the

---

<sup>2</sup>Hadron-Elektron-Ring-Anlage, which was operated until 2007 at DESY Hamburg.

study of strongly interacting matter and to understand what happened in the early universe [32].

LHCb is the other experiment having a dedicated task at the LHC. LHCb will concentrate on  $b$ -physics and it is aiming for a peak luminosity of  $\mathcal{L} = 10^{32} \text{ cm}^{-2} \text{ s}^{-1}$ . In particular the goal is the precise measuring the of CP violation in the interactions of  $b$ -hadrons. Additionally, LHCb will study rare  $B$ - and  $\tau$ -decays,  $D$ - $\bar{D}$  oscillations and  $B_c$ -meson decays [35].

ATLAS and CMS are two general purpose experiments at the LHC. They are aiming for a peak luminosity of  $\mathcal{L} = 10^{34} \text{ cm}^{-2} \text{ s}^{-1}$ . The expected cross-sections and the corresponding event rates for various real and hypothetical physics processes at  $\mathcal{L} = 10^{33} \text{ cm}^{-2} \text{ s}^{-1}$  are depicted in figure 2.2.

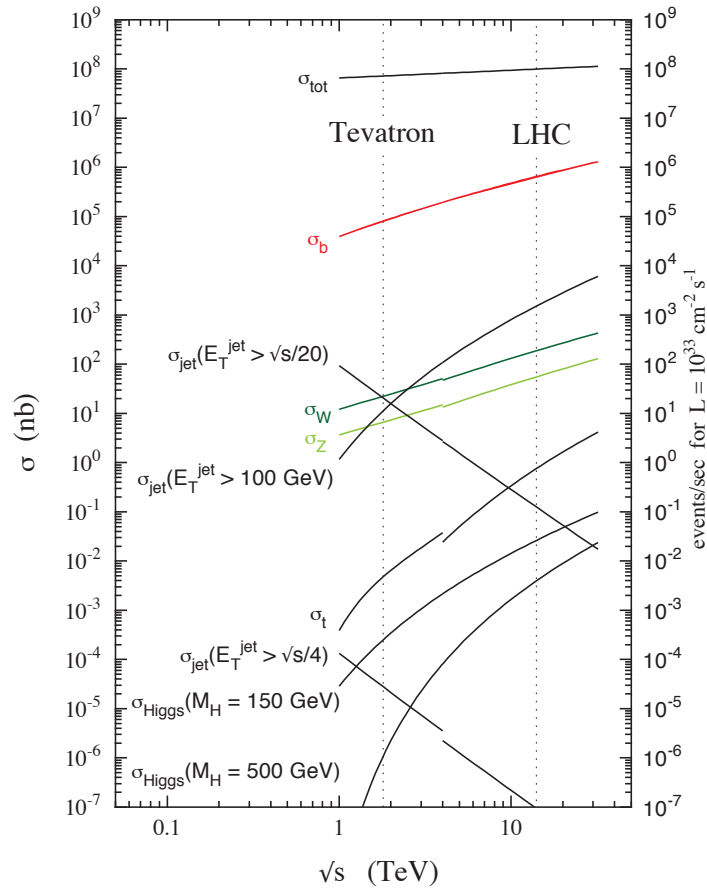


**Figure 2.2:** Cross-sections and event rates of various physics processes at the proton-antiproton collider Tevatron and the proton-proton collider LHC [36].

The expected integrated luminosity per year will be  $10-30 \text{ fb}^{-1}$  and  $100-300 \text{ fb}^{-1}$  for low and high luminosity phases, respectively [27]. One of the major goals of these general purpose detectors is the discovery of the Higgs boson. Additionally they will be searching for physics beyond the Standard Model like SUSY, extra dimensions, and other models. But also Standard Model physics is part of the physics program, for example detailed measurement of the properties of the top quark in the high statistics

environment of LHC.

There are two additional experiments at LHC. LHCf [37] and TOTEM<sup>3</sup> [38] are parasitic experiments at the interactions points of ATLAS and CMS, respectively. Both experiments are dedicated to forward physics. TOTEM aims to measure the total  $pp$  cross-section and protons from elastic and diffractive scattering at very forward angles. The purpose of the LHCf experiment is the measurement of the very forward production cross-sections and the energy spectra of neutral pions and neutrons. The parameters measured by TOTEM and LHCf can be used for example to make the simulation of airshowers more precise, since the total cross-section and the energy spectra at the primary vertices are the keys for the development of a phenomenological model for an airshower.

## 2.2 The Compact Muon Solenoid

The Compact Muon Solenoid (CMS) is a general purpose detector following the common concept of a collider detector in particle physics, it is built like a cylindrical onion. CMS has a length of 22 m, a diameter of 15 m and a total weight of 12500 t [39]. The name is originated by the following facts. CMS is compact compared to ATLAS, it has an excellent capability to measure muons and a magnetic field produced by an solenoidal coil. The task of the detector is to detect and identify the various particles coming from the hard interaction in the center, complicated by the high rate environment at the LHC. To detect almost all particles originated from the hard interaction, the detector is built hermetical around the interaction point having only a small gap for the beam pipe. To reach an almost hermetic coverage, CMS consists of a barrel part which is closed by two endcaps. The CMS detector and its different layers of the onion design are depicted in figure 2.3. The basic idea of the onion design is to measure the tracks of the charged particles in the first layer, which consists of a silicon pixel vertex detector (section 2.2.1) and a silicon strip detector (section 2.2.2) in case of CMS. During traversing the detector, charged particles are bended by a magnetic field to be able to measure their transverse momentum precisely and to determine the sign of their charge. At the next step, the energy of the particles is determined by stopping them in the layers from inside out according to their energy loss in matter. The adjoining layer to the tracker is the electromagnetic calorimeter (ECAL) described in section 2.2.3. Photons and electrons are stopped in the ECAL due to their high electromagnetic interactions with matter. Hadrons are stopped in the next layer, the hadronic calorimeter, due to their strong hadronic interaction with matter. Muons are the only particles that can traverse the whole detector, including the coil and return yoke, without getting stopped. Therefore, the final layer of the detector is the muon system, which is responsible for the identification of muons. In CMS, the muon system is also designed to do an additional momentum measurement of the traversing muons.

The coordinate system of CMS is centered at the nominal interaction point. The  $x$ -axis is pointing radially toward the center of the LHC, the  $y$ -axis is pointing vertically upward, and thus the  $z$ -axis is pointing toward the Jura mountains. The azimuthal angle  $\phi$  is measured in the  $x$ - $y$ -plane in range of  $-\pi < \phi \leq \pi$ . The angle  $\phi = 0$  is corre-

---

<sup>3</sup>Total Cross Section, Elastic Scattering and Diffraction Dissociation

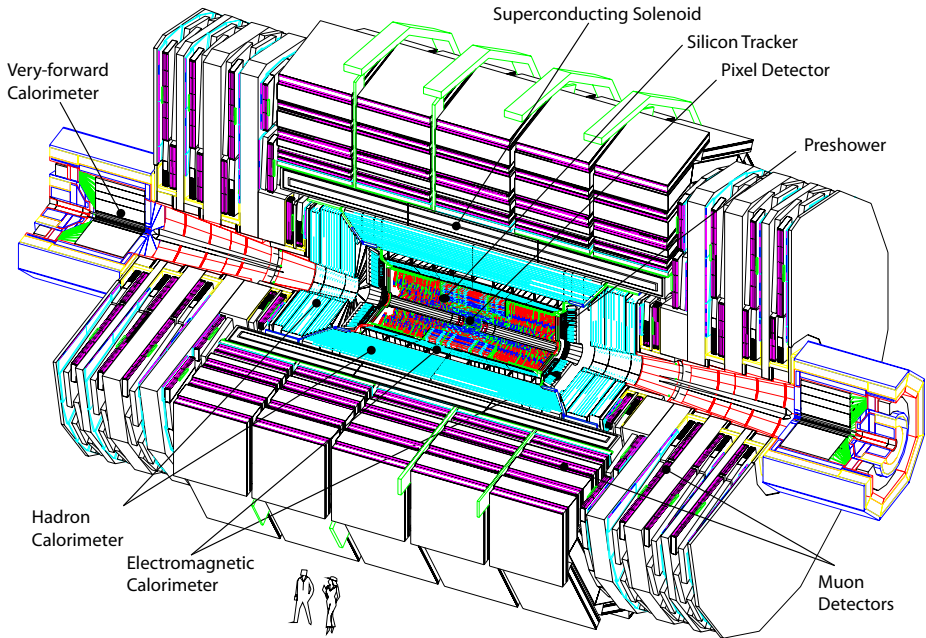


**Figure 2.3:** The CMS detector and its subdetector layers [27].

sponding to the  $+x$ -axis and  $\phi = \pi/2$  to the  $+y$ -axis. The polar angle  $\theta$  is measured with respect to the  $z$ -axis in the range of  $0 < \theta \leq \pi$ . The angle  $\theta = 0$  is corresponding to the  $+z$ -axis and  $\theta = \pi$  to the  $-z$ -axis. The sign of the pseudo-rapidity

$$\eta = -\ln \tan \frac{\theta}{2}$$

is equal to the sign of  $z$ . The pseudo-rapidity is a common variable to describe the angle of a particle to the beam axis. Differences measured in  $\eta$  are invariant under Lorentz boosts along the beam axis. There is one important variable in addition, which is commonly used in experimental particle physics  $\Delta R$ .

$$\Delta R = \sqrt{\Delta\eta^2 + \Delta\phi^2}$$

$\Delta R$  is also invariant under Lorentz boosts along the beam axis.

### 2.2.1 The Silicon Pixel Detector

The silicon pixel detector is the innermost subdetector in CMS. The high three dimensional resolution of the pixel detector is necessary for its major tasks.

- Tagging of heavy flavours like  $b$ -jets,  $c$ -jets and  $\tau$  leptons to distinguish them from light flavours like  $u$ -,  $d$ - or gluon jets,
- Primary, secondary and even tertiary vertex reconstruction,
- Confirmation or rejection of track segments proposed by the outer tracking systems.

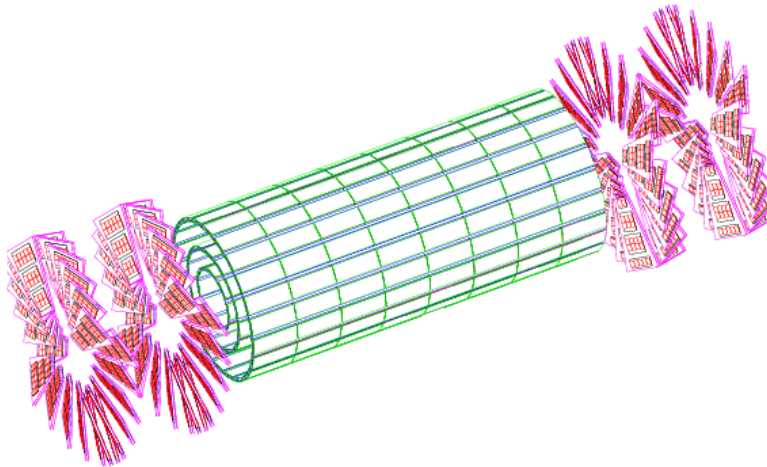


**Figure 2.4:** The layout of the silicon pixel detector used in the CMS detector [27].

The layout of the silicon pixel detector is depicted in figure 2.4. The pixel detector consists of three barrel layers located at the mean radii of 4.4 cm, 7.3 cm and 10.2 cm from the interaction point. The length of the barrel tubes is 53 cm. Two end disks are closing the barrel tubes on each side. The inner radius of the end disks is 6 cm and the outer radius is 15 cm. The end disks are located at  $|z| = 34.5$  cm and  $46.5$  cm. The pixel size is  $100 \times 150 \mu\text{m}^2$  in  $(r, \phi) \times z$  and the thickness is between  $200 \mu\text{m}$  and  $250 \mu\text{m}$ . The barrel consists of 768 pixel modules arranged into half-ladders and the end disks comprise 672 pixel modules arranged into a turbine-like geometry with 7 different modules on each blade. The pixel detector is covering a total area of about  $1 \text{ m}^2$  and comprises about 66 million channels. The readout chips, approximately 16000 are used, are bump-bonded directly to the detector modules [27, 40].

The spatial resolution is about  $10 \mu\text{m}$  in  $(r, \phi)$  and about  $20 \mu\text{m}$  in  $z$  obtained by test beam measurements. The resolution in  $r\text{-}\phi$  profits from the large Lorentz angle ( $23^\circ$ ) and the charge sharing involved between the pixels [27].

## 2.2.2 The Silicon Strip Detector

The tracker of the CMS detector consists of silicon strip modules. The inner radius of the silicon strip detector is 20 cm, its outer radius is 110 cm and its total length is 540 cm. The total area covered by the silicon strip detector is about  $200 \text{ m}^2$  and therefore it is the largest tracker based on silicon technology today. The layout of the silicon strip detector is depicted in figure 2.5. It is divided into four parts. The barrel comprises the Tracker Inner Barrel (TIB) and the Tracker Outer Barrel (TOB). The endcaps consists of the Tracker Inner Disks (TID) and the Tracker Endcap (TEC).

The TIB comprises four layers covering the region  $|z| < 65$  cm. The two innermost layers are made of stereo silicon sensors. A stereo sensor consists of two silicon modules with a stereo angle of 100 mrad in between. Those sensors provide a measurement in  $r\text{-}\phi$  and  $r\text{-}z$  with a single point resolution of  $23\text{-}24 \mu\text{m}$  and  $230 \mu\text{m}$ , respectively. The sensors having a thickness of  $320 \mu\text{m}$  and the pitch varies between  $80\text{-}120 \mu\text{m}$ .

The TOB is made of six layers covering the region  $|z| < 110$  cm. Also the two inner-

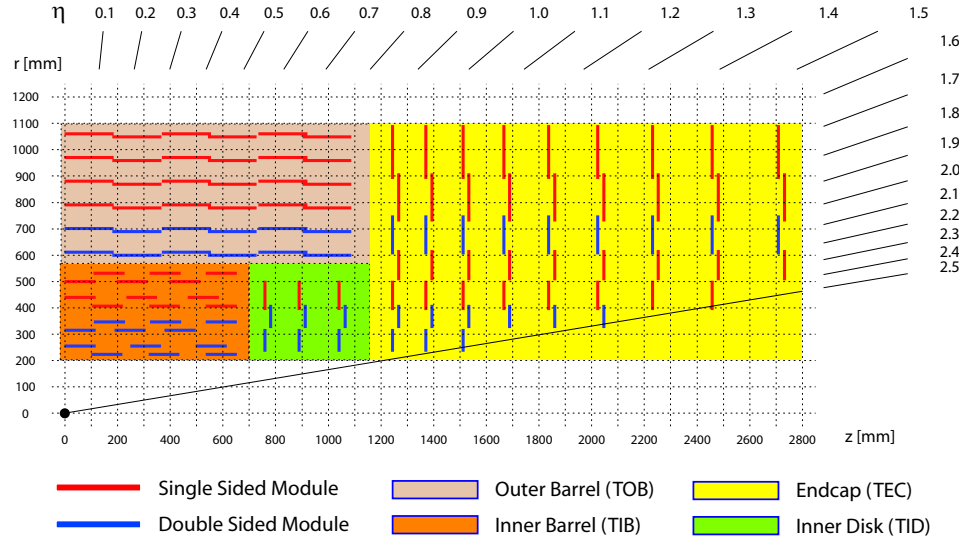


**Figure 2.5:** The layout of the Silicon Strip Detector of CMS. The  $r$ - $z$  view of one quarter is depicted. The different parts and module types are highlighted [26].

most layers of TOB consists of stereo sensors having the same stereo angle. The TOB sensors having a pitch varying between  $120\text{--}180\,\mu\text{m}$  and a thickness of  $500\,\mu\text{m}$ . Due to the wider pitch the single point resolution is worse, it varies from  $35\,\mu\text{m}$  to  $52\,\mu\text{m}$  in  $r\text{-}\phi$  and  $530\,\mu\text{m}$  in  $r\text{-}z$ , respectively.

Each TEC consists of nine disks covering the range of  $120\,\text{cm} < |z| < 280\,\text{cm}$ . The sensors of the endcaps are arranged in disks which are centered on the beam pipe, so that the strips are pointing towards the beam pipe. Therefore, each sensor has a variable pitch varying between  $96\,\mu\text{m}$  and  $143\,\mu\text{m}$  for the three innermost rings of TEC and  $143\,\mu\text{m}$  and  $183\,\mu\text{m}$  for the four outermost layers, respectively. The thickness of the sensors is  $320\,\mu\text{m}$  for the three innermost rings and  $500\,\mu\text{m}$  for the remaining rings. On the innermost two rings and on the fifth ring of TEC, stereo sensors are mounted.

Each TID is made of three small disks covering the gap between TIB and TEC. Also the disks of TID are centered on the beam pipe. The pitch of the TID sensors varies between  $96\,\mu\text{m}$  and  $143\,\mu\text{m}$ . The thickness of the TID sensors is  $320\,\mu\text{m}$ . The first two rings of TID are assembled with stereo sensors.

The silicon strip detector comprises around 15400 modules and roughly ten million channels in total. The silicon tracker covers the pseudo-rapidity region of  $|\eta| < 2.4$  and it is operated at a temperature of  $-20\text{ }^\circ\text{C}$  to avoid damages, due to the high radiation dose. A flux of  $1.6 \times 10^{14}$  1 MeV-equivalent neutrons per  $\text{cm}^2$  is expected, at a radius of 22 cm, for an operation over a period of ten years, which is equivalent to a dose of 70 kGy [27, 40].

The performance of the tracker is described in section 4.1.6.

### 2.2.3 The Electromagnetic Calorimeter

The electromagnetic calorimeter plays an essential role for the discovery of a possibly low mass Higgs boson ( $m_H < 130\,\text{GeV}$ ). The decay  $H \rightarrow \gamma\gamma$  is one of the bench-

mark channels in CMS. Therefore a high performance electromagnetic calorimeter was designed to measure electrons and photons with a high precision. The best energy resolution is offered by scintillating crystal calorimeters.

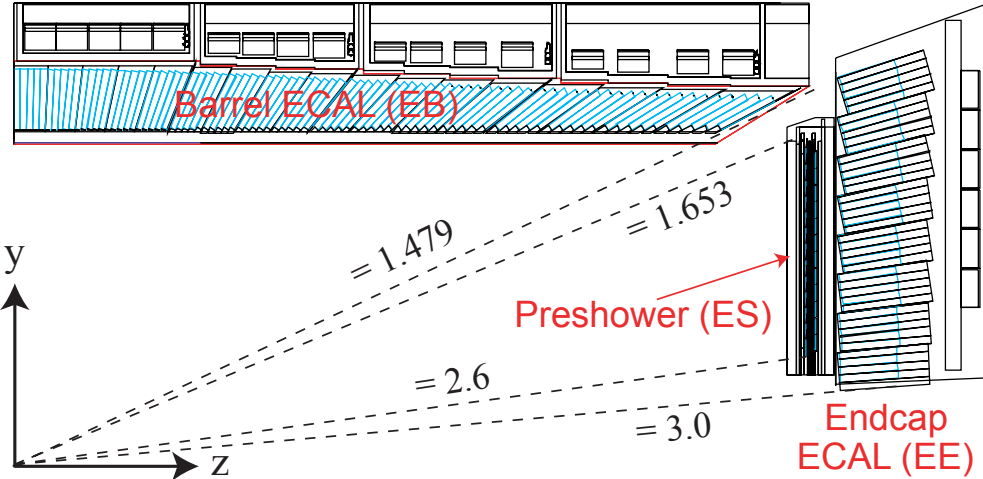


**Figure 2.6:** The layout of the electromagnetic calorimeter of CMS. The  $r$ - $z$  view of one quarter is depicted. The ECAL can be divided into the regions ECAL barrel, ECAL endcap and the ECAL preshower [27].

The electromagnetic calorimeter of CMS is based on lead tungstate ( $\text{PbWO}_4$ ) crystals. The lead tungstate crystals have a short radiation length<sup>4</sup> of  $X_0 = 0.89$  cm, a small Molière radius<sup>5</sup> of  $R_M = 2.19$  cm, they are fast and radiation hard.

The electromagnetic calorimeter of CMS is depicted in figure 2.6. It is made of three parts, the ECAL barrel comprising 61200 lead tungstate crystals, closed by two ECAL endcaps each consisting of 7324 lead tungstate crystals and the ECAL preshower each containing  $3X_0$  of lead. The ECAL barrel is covering a pseudo-rapidity interval of  $|\eta| < 1.479$  and the ECAL endcap an interval of  $1.479 < |\eta| < 3.0$ , respectively.

The front face of the used lead tungstate crystals is  $22 \times 22$  mm<sup>2</sup>, which is close to the Molière radius, and corresponding to a granularity of  $\Delta\eta \times \Delta\phi = 0.0175 \times 0.0175$  in the barrel region. The front face cross section of the end cap crystals is increased to  $28.6 \times 28.6$  mm<sup>2</sup>. The length of the crystal is 23 cm in the barrel region and 22 cm in the end cap, due to the additional preshower layer. This corresponds to a total radiation length of around  $25.8X_0$  at  $\eta = 0$ .

Silicon avalanche photodiodes are used to readout the scintillating crystals in the barrel region and vacuum phototriodes in the end cap region, respectively. The sensitive layers in the preshower are two planes of silicon strip detectors behind  $2X_0$  and  $3X_0$  of lead absorbers [27, 41].

A detailed performance study of the electromagnetic calorimeter, obtained by test beam measurements, can be found in [42]. The energy resolution of a  $3 \times 3$  crystal array covered uniformly by 120 GeV electrons is 0.5% after applying an energy correction scheme.

<sup>4</sup>A high energetic electron loses all but  $1/e$  of its energy in the range of a radiation length  $X_0$ .

<sup>5</sup>The Molière radius is material constant, which describes the radius of a cylinder, that contains 90% of the energy of an electromagnetic shower originated by a high energetic electron or photon.

## 2.2.4 The Hadron Calorimeter

The hadron calorimeter is an important subdetector of CMS, it measures the direction and the energies of quark and gluon jets, as well as the missing transverse energy (MET). MET is a typical signature for new physics, i.e. supersymmetry, but also important get information about neutrinos. In addition, the hadron calorimeter is very useful for the identification of electron, photons and muons, in cooperation with the electromagnetic calorimeter and the muon systems, respectively.

The hadron calorimeter of CMS is build as a sampling calorimeter to minimize the amount of space needed for the active medium and to increase the volume of the absorber material. The hadron calorimeter is divided into four parts, the HCAL barrel (HB), the HCAL endcap (HE), the hadron outer calorimeter (HO) (depicted in figure 2.7) and the hadron forward calorimeter (HF). Most parts of hadronic calorimeter are located inside the magnet coil and their design is constraint by the magnetic field. For example non-magnetic materials, copper alloy (brass) and stainless steel have to be used.

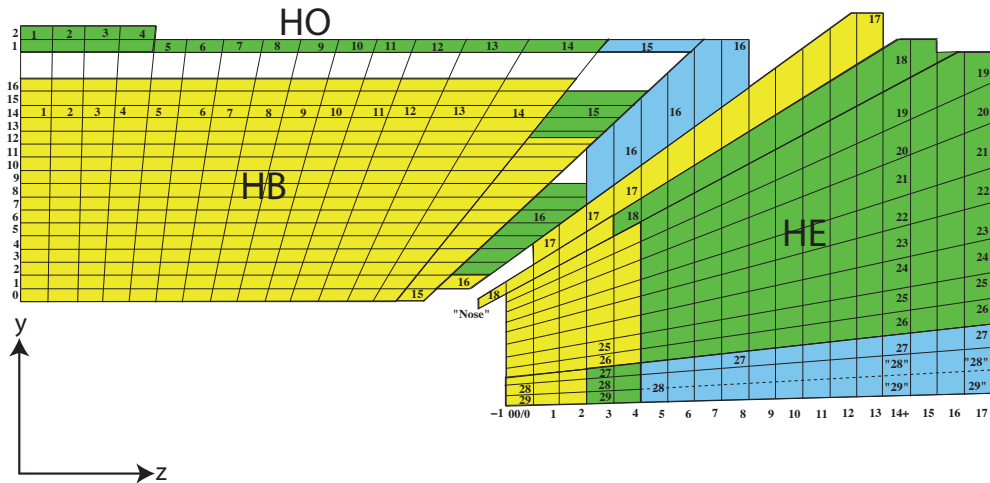


**Figure 2.7:** The layout of the hadronic calorimeter of CMS. The  $r$ - $z$  view of one quarter is depicted [43].

The HB covers the pseudo-rapidity region of  $|\eta| < 1.4$ . In total 2304 towers with a segmentation of  $\Delta\eta \times \Delta\phi = 0.087 \times 0.087$  are used. The HB consists of alternating layers of brass and plastic scintillator plates read out by wavelength shifting plastic fibers. There are 15 brass plates having a thickness of 5 cm. Additional two stainless steel plates are used for mechanical stability. The thickness of the scintillator adjoining to the ECAL is 9 mm and 3.7 mm for the remaining ones. The sampling depth at  $\eta = 0$  is 7.2 hadronic interaction lengths including the electromagnetic calorimeter.

The HO is located outside of the vacuum tank of the coil and inside of the muon system. It covers a pseudo-rapidity region of  $|\eta| < 1.26$  and is made of scintillator tiles with a thickness of 10 mm. The HO acts as a tail catcher for penetrating hadron showers and increases the effective thickness to ten hadronic interaction lengths.

The HE covers a pseudo-rapidity range of  $1.3 < |\eta| < 3.0$ . The thickness of the brass

absorbers is 8 cm rather than 5 cm in the HB, whereas the thickness of the scintillators is the same. The HE is made of 2304 towers in total. The five outermost towers having a  $\phi$  segmentation of  $5^\circ$  and a  $\eta$  segmentation 0.087. The eight innermost towers have  $\phi$  segmentation of  $10^\circ$  and a  $\eta$  segmentation of 0.09 to 0.35.

The HF is located 11.2 m away from the interaction point in the high radiation environment of the very forward direction. The HF extends the sensitivity to the pseudo-rapidity region of  $3.0 < |\eta| < 5.0$ . The depth of the HF is 1.65 m. The material of the absorber is steel and the active element are quartz fibers running parallel to the beam line. The HF is preferentially sensitive to Cerenkov light from pions [27, 44, 45].

The combined energy resolution of the hadron calorimeter and the electromagnetic calorimeter<sup>6</sup> for a incident energy of  $30 \text{ GeV} < E < 1 \text{ TeV}$  is

$$\frac{\Delta E}{E} = \frac{1}{\sqrt{E}} \oplus 0.045 \quad (\text{for } E \text{ given in GeV}) \quad (2.1)$$

[44].

## 2.2.5 The Solenoid

To measure the momentum and to determine the sign of a traversing charged particle a magnetic field is necessary the bend the trajectory. For the determination of the charge of a 1 TeV muon a momentum resolution of about  $\Delta p/p \approx 10\%$  is necessary. This was one of the requirements for the bending power.

The magnetic field of CMS is produced by a large superconducting solenoid. It has an inner radius of 5.9 m and length of 12.9 m. The solenoid is cooled down to 4.5 K using helium and its cold mass is about 220 t. The coil has 2168 number of turns and the stored energy is 2.7 GJ. The aluminum conductor cross-section is  $64 \times 22 \text{ mm}^2$ , since it has to carry a current of 19.5 kA to produce a magnetic field of about 4 T [27, 46].

## 2.2.6 The Muon System

As the name Compact Muon Solenoid implies, the muon system is an important sub-detector of CMS. One of the reasons is golden decay channel of a heavy Higgs boson ( $m_H > 180 \text{ GeV}$ )  $H \rightarrow ZZ \rightarrow 4\mu$ . This channel provides a extremely clean signature.

Three types of gaseous detectors are used in the muon system. Drift tubes (DT) are deployed in the barrel region covering a pseudo-rapidity range of  $|\eta| < 1.2$ , since the muon rate, the neutron induces backgrounds, and the remaining magnetic field are low. The two endcaps of the muon system have a coverage of  $|\eta| < 2.4$ . In the endcap region the muon and background rate as well as the magnetic field are high, therefore the endcaps are equipped with cathode strip chambers (CSC). In addition to the DTs and the CSCs, resistive plate chambers (RPC) are used in both barrel and endcap. RPCs provide a fast response and having a good time resolution, but the spatial resolution is worse. The RPC can be used to identify the correct bunch crossing belonging to the measured muon. The coverage of the RPCs is  $|\eta| < 1.6$  in the initial phase of the LHC

---

<sup>6</sup>Obtained by test beam measurements

and later on  $|\eta| < 2.1$ . All three detector technologies are used for the Level 1 trigger, providing independent and complementary information. The muon system as it is used during the initial phase of LHC is shown in figure 2.8.

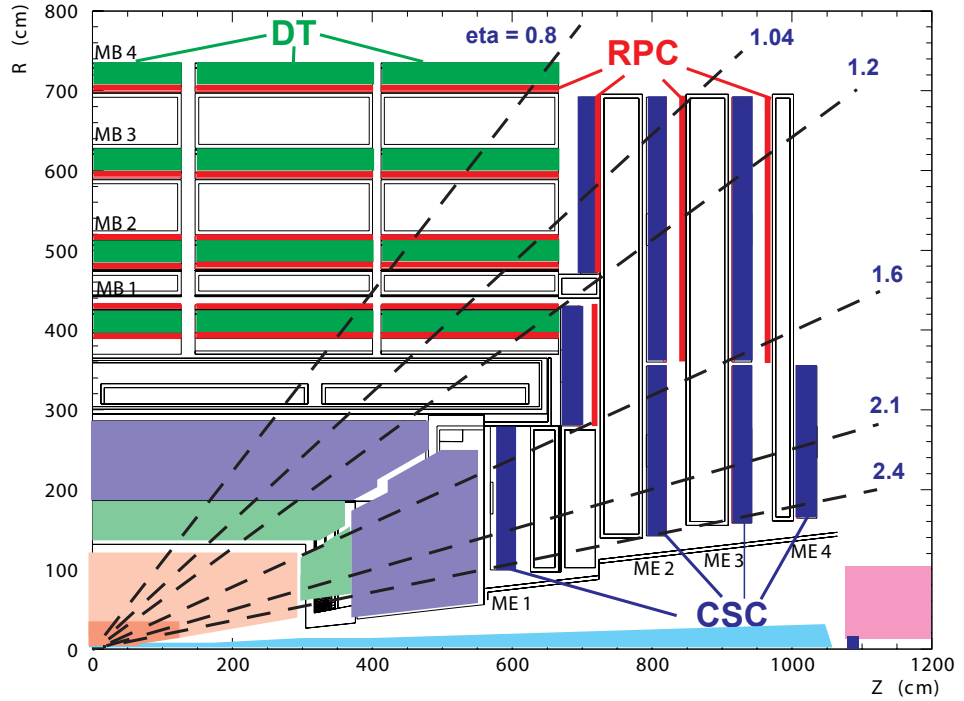


**Figure 2.8:** The  $r$ - $z$  view of a quarter of the CMS muon system with the different detector technologies used are drift tubes (DT), cathode strip chambers (CSC) and resistive plate chambers (RPC) [27].

The four layers of DTs and RPCs are mounted within the iron yoke in the barrel region, labelled MB1, MB2, MB3 and MB4. The DTs are located at radii of roughly 4.0, 4.9, 5.9 and 7.0 m from the interaction point. The DT chambers of the MB1–MB3 are made of three super layers, each consisting of four staggered drift tube layers. Two super layers are measuring the  $r$ - $\phi$  coordinate and the third one the  $z$  coordinate. The outermost station MB4 only consists of two super layers measuring the  $r$ - $\phi$  coordinate. The segmentation along the  $z$  axis follows the five wheels of the iron yoke. Each of those wheels is divided into twelve sectors. The barrel comprises 250 DT chambers in total, each providing a single point resolution in the order of  $200\ \mu\text{m}$ . The DTs in the innermost stations MB1 and MB2 are embedded in a “sandwich” of two RPCs, whereas the outermost stations MB3 and MB4 have only one layer of RPCs. In total there are 480 RPCs deployed in the barrel.

In the endcap region, the CSCs and the RPCs mounted on four disks perpendicular to the beam pipe, labelled ME1 to ME4. In the endcap, the CSCs are arranged in concentric rings around the beam line. The ME1 station is made of three rings (ME1/1, ME1/2 and ME1/3), while the other stations consists of two rings. Each ring is equipped with 36 chambers except the innermost rings of ME2–ME4 which have 18 chambers. In total the endcaps comprise 468 CSCs. The spatial resolution of the chambers is typically in the order of  $200\ \mu\text{m}$  and  $100\ \mu\text{m}$  for the ME1/1, respectively. The RPCs in the endcaps are only mounted in the outer rings for the first period of data taking. In total,

the entire muon system has about one million channels and its active material covers an area of about  $25000\text{ m}^2$  [27, 47].

The performance of the muon system is discussed later on in section 4.3.4.

# Chapter 3

## Monte Carlo Simulation

Computing and modern data communications becomes more and more important in life, that is also the case in high energy physics. One use case is the Monte Carlo simulation, which is essential to prepare an analysis, that is later on used on detector data. Since the amount of data for a modern high energy physics experiment like CMS is huge and detailed detector simulations are highly time consuming, world wide distributed computing systems become more and more important. In analogy to the power grid, this world wide distributed computing systems are called computing grid [48].

### 3.1 Monte Carlo Techniques

A Monte Carlo method uses sequences of random numbers for the calculation of probabilities and related quantities. There is no single Monte Carlo method, but the term describes a variety of numerical techniques using random numbers for their purposes. Monte Carlo methods can be applied, if the solution of a problem can be related to a parameter of a probability distribution. Therefore, they are widely used in computational simulations of complicated physical systems. In particle physics this is usually done in two steps, the event generation and detector simulation. Considering a simple scattering of electrons by a target and assuming a theory exists that describes the probability for an event to occur as function of the scattering angle, an event generator is nothing else than a Monte Carlo program generating values of the scattering angle. In particle physics, a variety of event generators have been developed over many years, that describe more complicate particle reactions more detailed than this simple example. The detector simulation works similarly, it simulates interactions of particles, while they are traversing the detector. For each interaction, there is a theoretical prediction expressible as a probability distribution, which can be used to randomly select a final state of the given particle. In addition, also the detector response is simulated using Monte Carlo methods [49].

#### The Hit-and-miss Method

One of the Monte Carlo methods is the so called hit-and-miss method, which was used for example to select events according to a given matrix element (see chapter 5). Considering a probability density function  $f(x)$ , which can be enclosed by a box within

the intervals  $x_{min} \leq x \leq x_{max}$  and  $0 \leq f(x) \leq f_{max}$  (see figure 3.1). Than following algorithm can be used to generate a distribution of random numbers according to  $f(x)$  [49].

- Generate a uniformly distributed random number  $x$  in the interval  $x_{min} \leq x \leq x_{max}$  and evaluate  $f(x)$
- Generate a second uniformly distributed random number  $y$  between 0 and  $f_{max}$
- If  $y \leq f(x)$  accept  $x$ , else reject  $x$  and restart

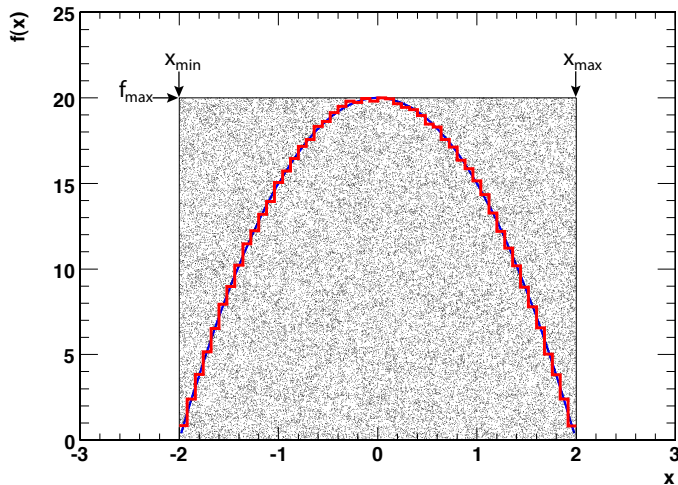


**Figure 3.1:** The dark colored curve shows the probability density function  $f(x)$  enclosed by a box with the intervals  $x_{min} \leq x \leq x_{max}$  and  $0 \leq f(x) \leq f_{max}$ . The generated pairs of random numbers are depicted as a scatter plot within the box. In light color the normalized histogram of accepted  $x$  values is shown.

## 3.2 The Monte Carlo Production Chain

The detailed entire production chain to produce fully simulated events is depended on the software version. The CMS software<sup>1</sup> release of the series CMSSW \_1\_6 was used for production and analysis of the events in this thesis. In that software release, the entire production chain is separated into four steps.

The production chain as it was used in the CSA07<sup>2</sup> is depicted in figure 3.2. For the generation and detector simulation step a release of the CMSSW \_1\_4 series has to be used. Its geometry is compatible with the geometry of the other steps in CMSSW \_1\_6, whereas the detector simulation within CMSSW \_1\_6 uses an incompatible geometry.

<sup>1</sup>The software framework of CMS was completely rewritten in 2006 and is called CMSSW.

<sup>2</sup>The Computing, Software and Analysis Challenge 2007 was a test run of the interplay of computing, software and analysis to be prepared for data taking.

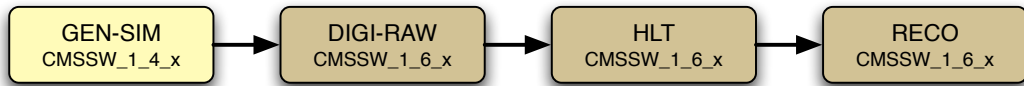


**Figure 3.2:** Production chain to produce fully reconstructed events with the CMSSW framework in the version 1\_6\_x.

### 3.2.1 Event Generation

The first step in the production chain is the event generation. The event generator uses the Monte Carlo technique to simulate a “raw“ event, that is originated by a proton-proton collision as it could be observed by an ideal detector. The type of events being generated can be controlled by parameters in a configuration file, also specific decay channels of a particle can be chosen and manipulated in that manner. For the simulation of the physics processes, an event generator uses theoretical and also empirical models to generate events, which approximate the behaviour of real data. That includes parton distribution functions, initial- and final state radiation, fragmentation, matrix elements and decays of particles. The default generator, that is used in CMSSW is PYTHIA 6.409, which is based on FORTRAN [50].

The event generator itself does not include interactions with matter in the detector or the beam pipe, it simulates only the decay of particles as long as there are marked “unstable“. The resulting set of “stable“ particles will be used as input for the succeeding detector simulation.

### 3.2.2 Detector Simulation

The detector simulation is the most time consuming step in the production chain. The detector simulation of CMS is based on the GEANT4<sup>3</sup> package [51], which is the standard package used to propagate particles through matter. Each “stable“ particle passed over from the event generator will be propagated through the detector, including interactions with the detector material, energy deposition in sensitive volumes, the magnetic field, and in-flight decays. The simulated hits and tracks will be stored and used by the digitization step.

To have a realistic detector simulation, the detailed geometry of CMS with various material and sensitive detector volumes has been made accessible to GEANT 4. The XML based language DDL<sup>4</sup> has been introduced for these purposes.

### 3.2.3 Digitization

After the detector simulation step is done, the detector response must be simulated. The digitization step is the simulation of the electronic readout used to acquire data.

<sup>3</sup>GEometry ANd Tracking (<http://cern.ch/geant4>)

<sup>4</sup>Detector Description Language (<https://twiki.cern.ch/twiki/bin/view/CMS/SWGuideDetectorDescription>)

Therefore the simulated hits and energy depositions passed over from detector simulation will be converted into “real” detector signal hits. At this stage the pile-up can be mixed with the signal event according to the expected number of parasitic collisions within a bunch crossing. This is done by the so called mixing module, which produces a crossing frame, that will be used as input for the digitization step [27]. After the digitization step is done, the produced data is converted into raw data, which have exactly the same structure as real data coming from the CMS detector.

### 3.2.4 Trigger

The trigger in CMS consists of two levels, the Level 1 (L1) trigger and the High Level Trigger (HLT). The L1 trigger is a hardware based trigger, that needs to be simulated by software as well. After this step, the structure of simulated data and “real” data are almost the same. The HLT algorithms are run on the raw data format to produce the HLT decision. In simulation there is also the possibility to store events, which are not triggered.

### 3.2.5 Reconstruction

The last step in the production chain is the reconstruction of physics objects like tracks and jets. The reconstruction starts from reconstructed hits or energy depositions in the specific subdetector. In case of the tracker, track finding algorithms are used to reconstruct the particle trajectories. Jets are formed by using jet algorithms on the grouped energy depositions in the calorimeter. Also a stand alone muon reconstruction is done based on reconstructed hits and track segments in the muon system.

Hereafter, high level physics objects like electrons, photons and muons are produced by combining informations of different subdetectors.

## 3.3 The LHC Computing Grid

The LHC will produce around 15 petabytes<sup>5</sup> of data per year, which will be accessed and analysed by thousands of scientist around the world. The analysis of this huge amount of data requires in the order of 100000 CPUs. The traditional approach of having all this services centralized at CERN, near the experiments, would be hardly realizable. The alternative is a worldwide distributed computing grid, which has several advantages compared to the centralized approach. The cost of maintaining and upgrading such a computing system can be more easily handled in a distributed environment. The institutes and national organizations can fund local resources and retain responsibility for them, while contributing to the whole computing grid. In addition, there are no single points of failure in a distributed computing system, because there is more then one copy of the data, that can be analysed at more then one computing center, including automatic assignment of jobs to free and available resources, except for the TIER 0. Nevertheless a distributed computing grid is a challenge, in terms of the network bandwidth between the centers, the synchronization and compatibility of the installed software versions, the interplay of different hardware architectures, data

---

<sup>5</sup>1 PB = 1000 TB = 1000<sup>2</sup> GB

safety and the authorization mechanism to provide access to a whole community. To provide access to the data and to ease the usage of the grid, different flavours of grid middlewares have been established. The middleware used for the LHC Computing Grid (LCG) is gLite<sup>6</sup> [52].

The LHC computing grid has a tiered architecture (see figure 3.3). The tasks of the various tiers for the CMS experiment are described in the following.

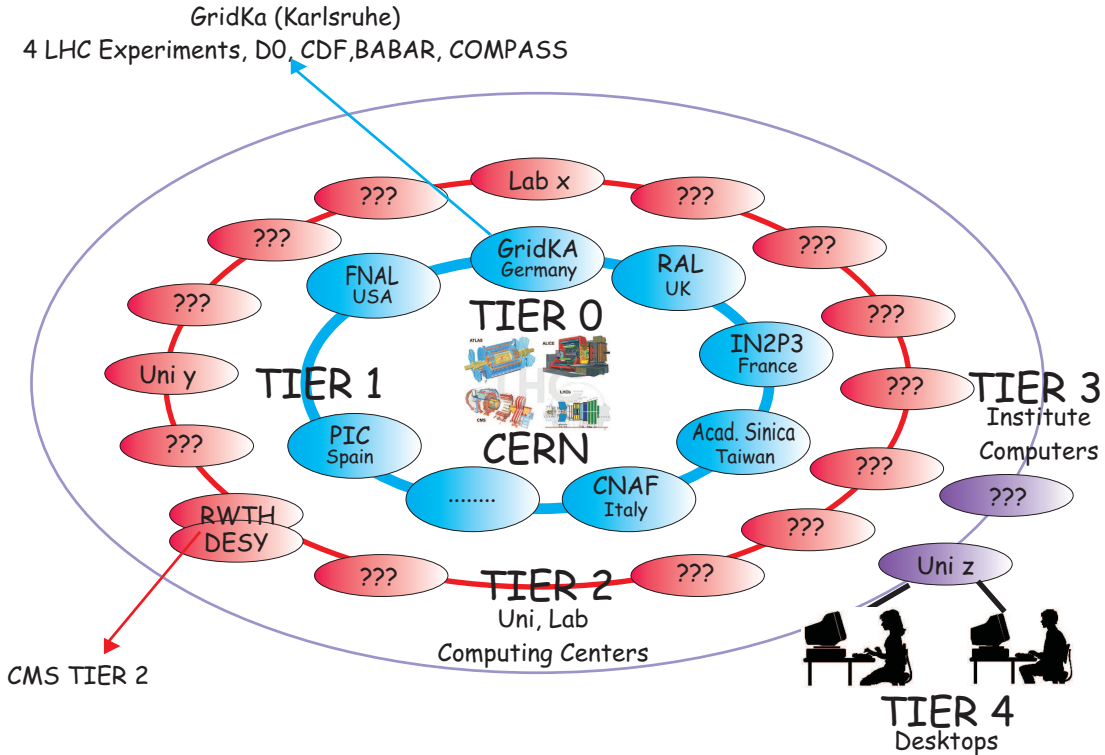


**Figure 3.3:** *Tiered structure of the LHC computing grid.*

## TIER 0

The TIER 0 is located directly at CERN. The tasks of the TIER 0 center are buffering data from the online systems at the CMS experimental site, performing a pseudo real time reconstruction of the raw data, stream the output into physics datasets and secure raw and reconstructed data on tape in the full event format. At the end a copy of the full event data must be reliably transferred to the TIER 1 centers. Therefore, the bandwidth must be high enough to ensure no significant backlog or latency [53].

## TIER 1

At the moment there are eight CMS TIER 1 centers distributed around the world, which are in all cases but one shared between the experiments. The TIER 1 centers are located at CERN (Switzerland), FNAL (USA), GridKa (Germany), PIC (Spain), IN2P3 (France), CNAF (Italy), RAL (UK) and ASCG (Taiwan). A crucial function of the

<sup>6</sup><http://glite.web.cern.ch/glite/>

TIER 1 is to store and provide access to the experiment raw and simulated event data. It is intended to have two copies of all raw data, one at TIER 0 and another distributed between the TIER 1 centers. Both copies will be used for reprocessing in order to optimize the overall efficiency. Therefore, the TIER 1 centers have to provide resources for running additional reconstruction or other large scale workflows with high throughput requirements. Selected CMS users may perform event selection, skims, reprocessing and other tasks at the TIER 1 centers on demand of CMS. But most of the CMS users will certainly use TIER 2/3 for their purposes. In addition to storing and processing CMS data, the TIER 1 centers have also the responsibility to distribute a selected fraction of the event data to TIER 2 centers for analysis purposes and to other TIER 1 centers for replication. The TIER 2 centers are also allowed to upload datasets to TIER 1 centers, including simulated data samples generated at TIER 2 centers, which are inefficient to reproduce in case of a TIER 2 storage failure [53].

## **TIER 2**

There are several TIER 2 centers distributed around the world. The only CMS TIER 2 center located in Germany is the federated TIER 2 Aachen/DESY. TIER 2 centers should provide large processing power, with less demanding storage systems (e.g. no tapes), availability and connectivity requirements than a TIER 1. The functions a TIER 2 center has to provide are fast and detailed Monte Carlo event generation, data processing for physics analysis and selected raw data processing for long term calibration, alignment tasks and detector studies. For the federated TIER 2 Aachen/DESY it is planned, that the main focus of Aachen will be Monte Carlo production, whereas DESY will be responsible for user analysis. The detector specific tasks will be shared between both locations [53].

## **TIER 3**

The main task of a TIER 3 center is to provide resources for physics analyses of a local community, since there are no official tasks required by CMS. Usually these are local batch systems available at the physics departments of universities, which are accessible via grid tools or in conventional ways.

## **3.4 Software Tools**

Job submission, monitoring and management is possible using built-in commands in the grid middleware. To manage a huge number of jobs, in particular for Monte Carlo production, the built-in tools are not completely adequate. Due to the crudity and lack of official tools during the beginning of this study, user friendly tools have been developed.

### **3.4.1 Grid Analysis Tool**

The first tool that was developed is the **Grid Analysis Tool** (GAT). The first version of the GAT was based on already existing shell scripts for automatic job submission and monitoring, but meanwhile it was completely revised.

The GAT consists of a set of Python and shell scripts, whereas the bookkeeping is done with a MySQL database. The Python part of the GAT is responsible for the communication with the grid middleware (Job submission, job status, fetching job output) and the MySQL database. Additionally, the CMSSW configuration can be manipulated, for example to use special random seeds for Monte Carlo production. A Python script updates the current status of a job and fetches the job output of already finished jobs and another one resubmits broken jobs. The shell script contains the workflow (i.e. to copy data to analyse from a storage element → analyse the input data → copy the output back to a storage element), which has to be executed on the worker nodes in the grid.

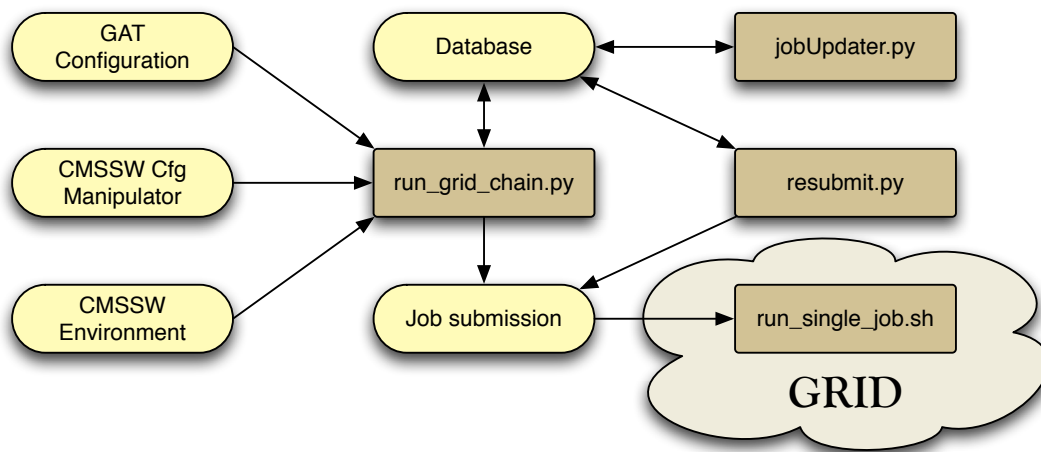


**Figure 3.4:** The structure of the GAT. The Python classes are marked in light colors and labelled by their function, whereas executables are marked in dark colors and denoted by their name.

The GAT can be used for private Monte Carlo production and for the analysis of these samples. The structure, depicted in figure 3.4, is rather flexible. Any CMSSW configuration can be executed on the grid, including getting input datasets as far as their location is stored in the MySQL database, copying output data back to a storage element and its registration to the MySQL database.

### 3.4.2 Job Monitor

A second tool developed to ease the job monitoring is the **Job Monitor** (JoMo). JoMo is **Graphical User Interface** (GUI) on the top of the QT application framework [54], which simplifies the setup of a GUI. A screen shot of the application is shown in figure 3.5. The Job Monitor provides the possibility to check the status of the job, to cancel a specific job and to get output of already finished jobs. Additionally, a configurable automatic job status update mechanism is implemented. The current status of a job is highlighted in color, so that the status is directly visible. In particular, failed or aborted jobs are identifiable by a red color. At the moment JoMo can only read job id's from a given text file, but an integration of the MySQL database is easily possible, since QT provides an excellent interface to access MySQL databases.

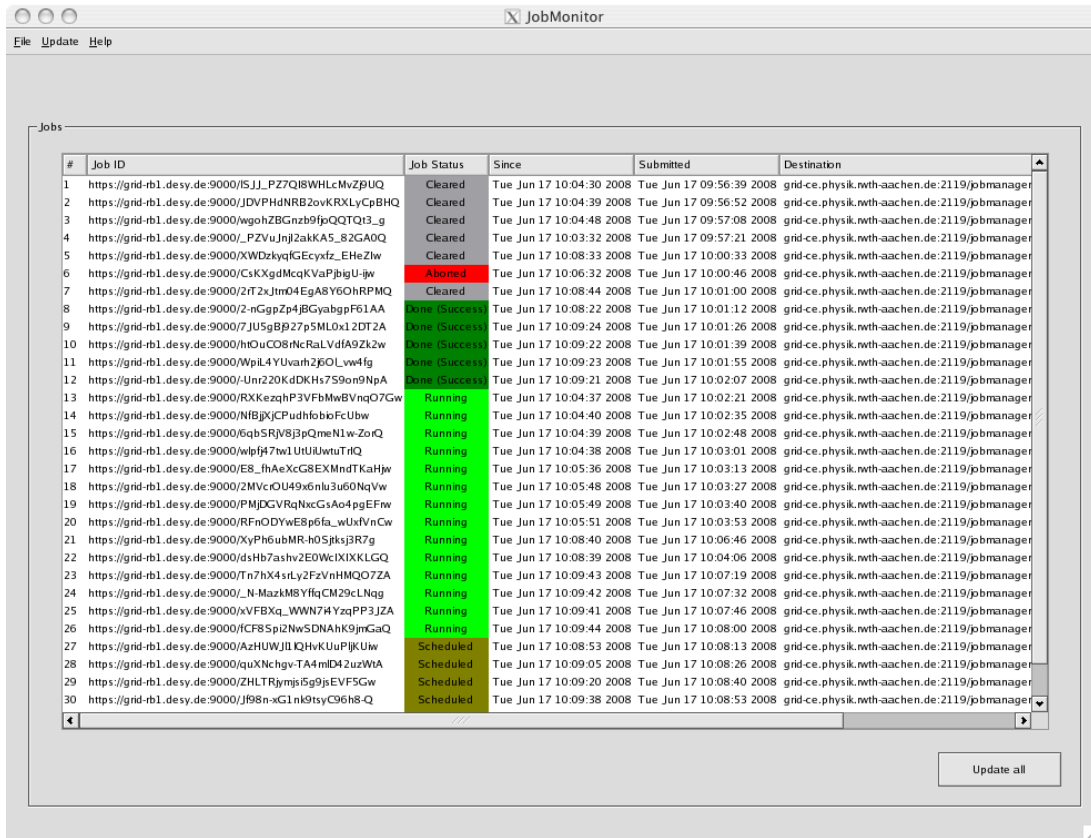


**Figure 3.5:** A screenshot of the Job Monitoring tool JoMo.

### 3.4.3 Official Tools

The official tool available for doing analysis on the grid, is called **CMS Remote Analysis Builder (CRAB)**<sup>7</sup>. The basic concept of CRAB is comparable to the concept of the GAT. CRAB hides the grid middleware from the user to provide a more user friendly way of using the grid. CRAB is suitable to analyse official and semi-official datasets, which are locatable by using the DBS/DLS<sup>8</sup> database services. CRAB also offers the possibility to run any CMSSW configuration on the grid. Using a recent version of CRAB, it is also possible to put information about the output datasets in a private DBS instance.

<sup>7</sup><http://cmsdoc.cern.ch/cms/ccs/wm/www/Crab/>

<sup>8</sup>Data Bookkeeping System (DBS) and Data Location Service (DLS) give access to a database where all necessary informations about a dataset is stored

# Chapter 4

## Reconstruction

In the reconstruction stage, physics objects for the final analysis are produced from the raw data. Independent from the subdetector, three different steps can be distinguished. The local reconstruction uses raw data to reconstruct basic objects like hits, energy depositions or segments in the local parts of the individual subdetectors. In the step of regional reconstruction these basic objects are combined to physics objects for each subdetector, for example tracks in the tracker or the muon system. The last step is the global reconstruction, where physics objects from the different subdetectors are combined to final physics objects of interest, like jets, tracks and vertices.

### 4.1 Track Reconstruction

There are two issues of track reconstruction in CMS caused by the dense hit environment. An efficient search for associated hits during the process of pattern recognition is required and a fast propagation of trajectory candidates. In the CMS tracker, the first issue can profit from the arrangement of the silicon modules in hermetic layers and the second one from the constant magnetic field of 4 Tesla. The typical step length for the propagation of track parameters during reconstruction is in the order of the distance between two adjacent silicon layers, therefore a helical track model is adequate.

For the reconstruction the detailed detector geometry of passive materials used in the simulation has been replaced by a list of material per layer. This approach simplifies the estimation of energy loss and multiple scattering, which can be done at the position of the sensitive elements without requiring additional propagation steps [55].

The track reconstruction is divided into five steps, which are described in the following subsections:

- Hit reconstruction consisting of clustering of strips/pixels and estimation of the position,
- Track seeding,
- Pattern recognition or trajectory building,
- Ambiguity resolution,
- Final track fit.

### 4.1.1 Hit Reconstruction

#### Silicon Strip Detectors

The reconstruction of clusters usually starts with gain calibrated zero-suppressed strip data. The clustering of the strips itself is done in the following way. Initially a seed strip is searched with a signal to noise ratio  $S/N > 3$ . The neighbors of that strip are included, if they have a  $S/N > 2$ . Holes inside the clusters are allowed only if there are assigned to highly inclined tracks. At last, the total signal size of the cluster has to exceed at least 5 times the size of the square root of the sum of the RMS noise squared of all involved strips.

The position of a cluster is usually determined by the center of gravity of the signal heights. To determine the position from the cluster edges is not trivial, due to the large interchannel coupling in the strip tracker. Nevertheless this method is applied for very large clusters containing at least 4 strips [27].

#### Silicon Pixel Detectors

The clustering for the pixel detector starts from a seed cluster, defined by a pixel with a signal to noise ratio  $S/N > 6$ . Pixels next to cluster pixels will be added to the cluster, if they have a  $S/N > 5$ . The cluster will be retained if its total charge has  $S/N > 10.1$ . The position of a cluster is determined for both directions independently. The used method is based on the relative charges of the pixels at the edge of the clusters and the associated reconstructed track angle. Details can be found in [27] and [56].

### 4.1.2 Track Seeding

The generation of a tracking seed provides an initial trajectory candidate for the full track reconstruction. The seed should define the initial five track parameters and their errors. These parameters should be close to their true value to allow the usage of a linear fit algorithm like the Kalman filter and the uncertainties should be small to allow a reasonable compact search region for hits [57].

The standard track seed in CMS is constructed from pairs of hits in the pixel detector and a vertex constraint. The seed finding efficiency is more than 99%. Alternatively the innermost layers of the strip detector can be used for track seeding as well as external seeds provided by the calorimeter or the muon detector [58].

### 4.1.3 Pattern Recognition

The pattern recognition is based on a combinatorial Kalman filter. The filter proceeds iteratively starting at the seed layer with coarse estimation of the track parameters and includes additional detection layers one by one. With each additional layer used, the track parameters are better constrained. In the extrapolation of the track from layer to layer effects like energy loss and multiple scattering are considered.

The trajectories are updated for each compatible hit, considering also a further trajectory candidate without using a measured hit to take care of the possibility, that the track did not leave a hit in treated detector layer. Afterwards the track parameters are

updated according to the Kalman filter algorithm. All trajectories are grown in turn up to the outer most layers until a stopping condition is reached. [55, 58]

#### 4.1.4 Trajectory Cleaner

Ambiguities in track finding can arise because a given track can be reconstructed from different seeds or a given seed can result in more than one track candidate. To avoid track double counting these ambiguities must be resolved [58].

The ambiguity resolution is based on the fraction of hits shared between two trajectories.

$$f_{\text{shared}} = \frac{N_{\text{shared}}^{\text{hits}}}{\min(N_1^{\text{hits}}, N_2^{\text{hits}})} \quad (4.1)$$

If the value of  $f_{\text{shared}}$  exceeds 0.5, the track candidate with the least number of hits is discarded. In the case of both track candidates having the same number of hits, the track candidate with the higher  $\chi^2$  is discarded. This is applied twice, once on all track candidates resulting from a single seed and once on the complete set of track candidates from all seeds [55].

#### 4.1.5 Track Fitting and Smoothing

The last step in track reconstruction is the track fitting and smoothing. After the building stage each track has its collection of hits and estimated track parameters. But, the complete information is only available after the last hit of the track is associated. The estimates are biased by the constraints applied during the seeding step. Therefore, the track is refitted using a least squares approach, which is a combination of a Kalman filter and a smoother. Whereas the Kalman filter runs from inside-out, the smoothing filter runs from outside-in in a second step. For each hit the updated parameters of the smoothing filter are combined with the predicted ones of the Kalman filter, to get an optimal estimation of the track parameters at the surface of each hit [58].

#### 4.1.6 Performance

The track finding efficiency has been evaluated for samples containing muons and pions with a  $p_T$  of 1, 10 and 100 GeV. The criteria for the definition of a successful reconstructed track is that at least 50% of the hits are shared with the simulated track and that the reconstructed tracks have at least 8 hits and a minimum  $p_T$  of 0.8 GeV. The results are depicted in figure 4.1. For muons the efficiency is more than 98% over most of the tracker acceptance. The drop at high  $\eta$  can be explained by the lack of coverage by the two pairs of endcap disks. The efficiency for hadrons is between 75 and 95% depending on the  $\eta$  region and the momentum. The efficiency is lower compared to the muons, because the hadrons interact with the tracker material.

A complete set of five parameters that describe a track are the transverse and longitudinal impact parameters  $d_0$  and  $z_0$ , the angular parameters  $\phi$  and  $\cot\theta$  and the transverse momentum  $p_T$ . The resolution in  $d_0$  and  $p_T$  are shown in figure 4.2. The impact parameter resolution at high momentum is nearly constant. It is dominated by the resolution

of the first hit in the pixel. At lower momentum, the  $d_0$  resolution drops due to multiple scattering. The resolution of the transverse momentum for high momenta is in the order of 1-2% up to  $|\eta| < 1.6$ . For higher values of  $\eta$  the lever arm of the measurement is reduced. The resolution at low momentum is dominated by multiple scattering and therefore by the amount of tracker material traversed by the track. [58]

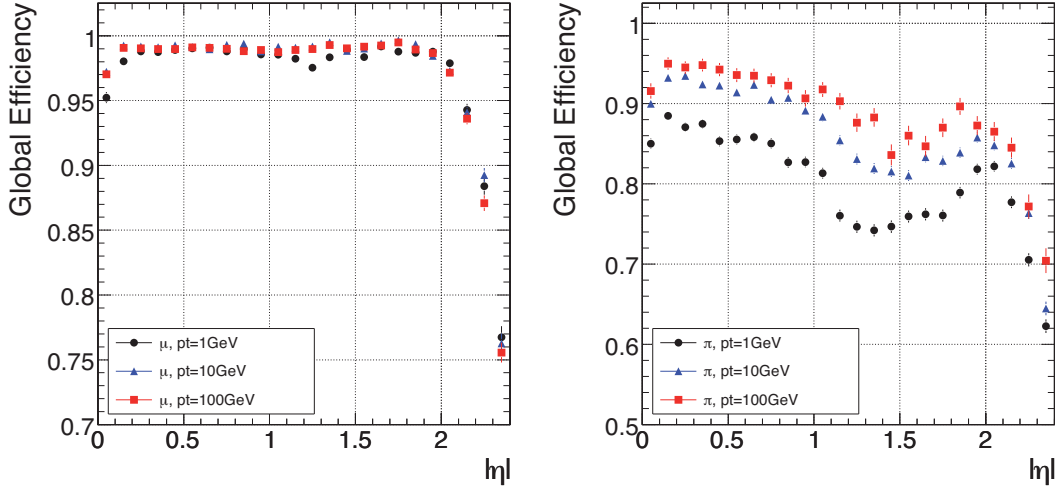


**Figure 4.1:** Track finding efficiency for muons (left) and for pions (right) with  $p_T = 1, 10$  and  $100\text{ GeV}$  as a function of  $\eta$  obtained by simulation [58].

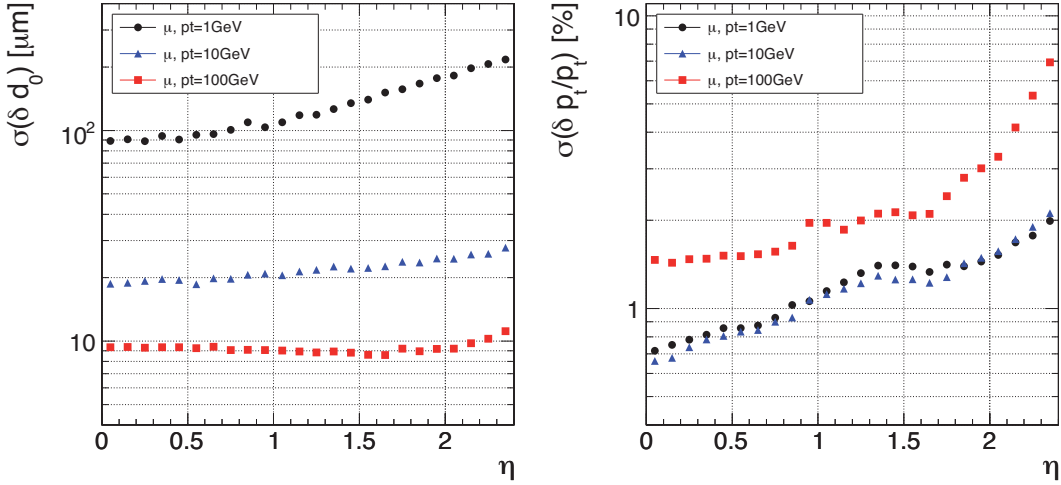


**Figure 4.2:** Resolution of the transverse impact parameter  $d_0$  (left) and in  $p_T$  (right) for muons with  $p_T = 1, 10$  and  $100\text{ GeV}$  obtained by simulation [58].

## 4.2 Secondary Vertex Reconstruction

There are several vertex fitting algorithms implemented in the CMS software. They can be divided into two classes, the least-square algorithms and the robust algorithms.

A least-square or linear algorithm uses all tracks with equal weights for the vertex fit. The Kalman vertex fitter is such a least-square algorithm. The robust or non-linear algorithms are able to down weight or discard tracks. For example, the adaptive vertex fitter is a non-linear vertex fitter. The main difference between this classes is the sensitivity to outlying tracks, which are either wrong reconstructed tracks or tracks from other vertices. The two fit algorithms used in this thesis will be described in the following.

### 4.2.1 Kalman Vertex Fitter

The Kalman Vertex Fitter, which is mathematically equivalent to a global least-square approximation, is the most often used algorithm for vertex reconstruction. To find the vertex position it minimizes the sum of the squared normalized distances of the tracks from the vertex position. For a linear model with gaussian random noise and no outlying measurements, it is the optimal estimator. For non-linear models or non-gaussian noise it is still the best linear estimator. On the other hand, least-square algorithms have a problem with the robustness. They always use all tracks with equal weights for the vertex estimation. Due to the quadratic form of the function that is minimized, outlaying tracks have a high influence on the estimation [59, 60].

### 4.2.2 Adaptive Vertex Fitter

The adaptive vertex fitter is a more robust vertex fitter. It is based on the standard Kalman fitter with some modifications to make it more robust. The adaptive vertex fitter has the possibility to down-weight outlying tracks with a weight  $w_i$ , which does not imply, that the algorithm is able to reject outlying tracks.

$$w_{i(\chi_i^2)} = \frac{e^{-\frac{\chi_i^2}{2T}}}{e^{-\frac{\chi_i^2}{2T}} + e^{-\frac{\chi_c^2}{2T}}} \quad (4.2)$$

The weight  $w_i$  depends on the compatibility of a track  $i$  with the vertex, measured by the normalized distance  $\chi_i^2$  to the vertex, and can be interpreted as the probability that the track belongs to the vertex. The constant  $\chi_c^2$  defines the threshold where  $w_i$  is equal to  $1/2$ . Beyond that point, a track is more likely an outlying track, than a track belonging to that vertex. The so called temperature  $T$  controls the functional dependence in eq. 4.2 (see figure 4.3). For a temperature of  $T = 0$ ,  $w_i$  results in a stepping function, which is equivalent to a hard cut on  $\chi_c^2$ . A geometric annealing has been introduced to prevent the algorithm from falling into a local minimum. The temperature is initialized by a pre-defined value  $T_{\text{ini}} > 1$  and will be lowered at each iteration by multiplying it with the annealing ratio  $r$  ( $r < 1$ ), until the temperature reaches a value of one. At each temperature value, the Kalman algorithm is used to fit the vertex, taking into account the weights of each track. The iteration stops as soon as the temperature is equal to one and the candidate vertex position has not changed by more than  $1 \mu\text{m}$ .

The advantage of the adaptive algorithm is that the weights can be assigned softly and they can be varied from each iteration to the next, until the fit converges. There is no prior estimated weighting of the tracks needed [59, 61].

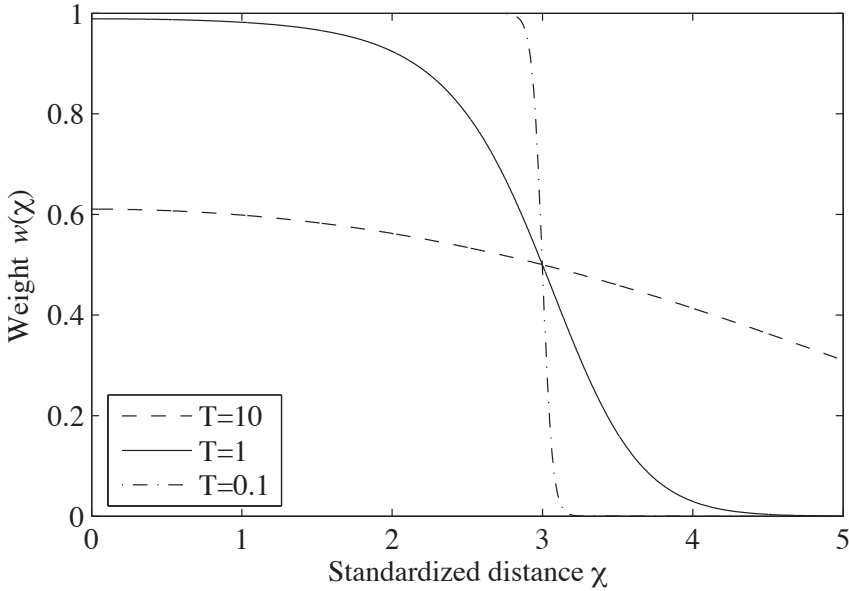


**Figure 4.3:** The weight function of eq. 4.2 at three different temperatures, with a cutoff of  $\chi_c = 3$  [61].

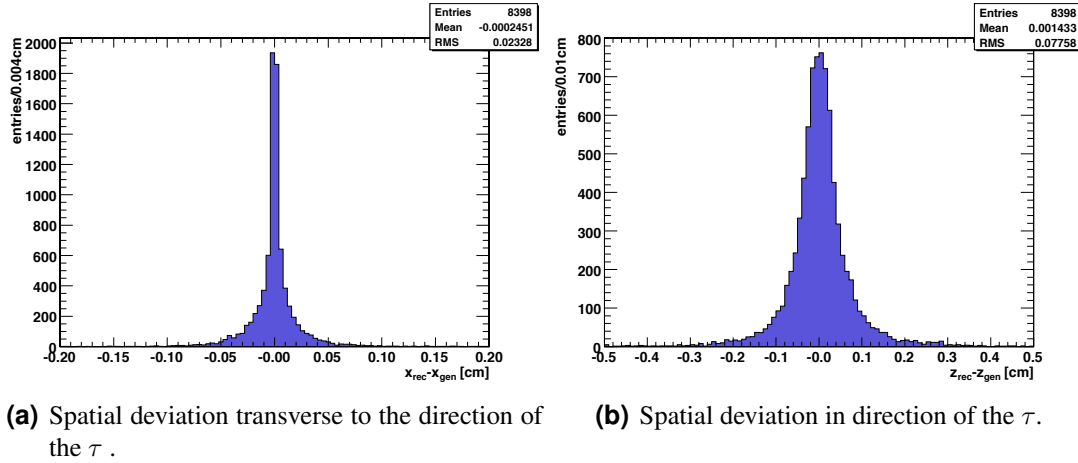
### 4.2.3 Performance

The performance of both algorithms is comparable [59]. The efficiency to reconstruct a secondary vertex for triggered and reconstructed  $\tau \rightarrow \mu\mu\mu$  events is  $\epsilon_{\text{adaptive}} = 99.4\%$  for the adaptive vertex fitter and  $\epsilon_{\text{Kalman}} = 99.9\%$  for the Kalman vertex fitter. The Kalman fit has the advantage, that it is possible to refit tracks using the new origin as a vertex constrain, but due to the high boost of the system, the impact on the track parameters is only marginal. On the other hand the adaptive vertex fitter is more robust and gives the possibility to cut on the number of tracks used to obtain the secondary vertex. In addition, the  $\chi^2$  value of the adaptive vertex fitter seems to be more reliable, due to the down-weighting of outliers. So, the adaptive vertex fitter was the preferable algorithm for the analysis. The spatial deviation of the generated vertex and reconstructed vertex is depicted in figure 4.4. The spatial deviation transverse to the  $\tau$  direction is nearly the same for  $x$  and  $y$ , namely in the order of  $233 \mu\text{m}$ . Whereas, the spatial deviation longitudinal to the  $\tau$  is  $776 \mu\text{m}$ .

## 4.3 Muon Reconstruction and Identification

For the identification of muons the outermost subdetector of CMS is used, the muon systems. Muons interact only weakly with the detector material, due to their high mass compared to electrons. Hence muons are able to traverse the detector while loosing only a small amount of their energy in the detector parts with a high density (e.g. the calorimeters, the magnet and the yoke).

The muon reconstruction software uses the muon system and the silicon tracker for the muon reconstruction. For the standalone muon reconstruction only the muon systems are used. The combined reconstruction in the muon system and the silicon tracker is called global muon reconstruction. The software has been designed for offline recon-



**(a)** Spatial deviation transverse to the direction of the  $\tau$ . **(b)** Spatial deviation in direction of the  $\tau$ .

**Figure 4.4:** *Spatial deviation of the fitted secondary vertex compared to the generated vertex in the direction of  $x$  (representative for the deviation transverse to the  $\tau$ ) and in direction of the  $\tau$ .*

struction and for the online event selection with the High Level Trigger. It uses the concept of regional reconstruction.

### 4.3.1 Local Reconstruction

The first step in the muon reconstruction is the local reconstruction in the Drift Tubes (DT), the Cathode Strip Chambers (CSC) and the Resistive Plate Chambers (RPC). The goal of the local reconstruction is the association of aligned hits and the obtainment of track segments.

#### Local Reconstruction in the Drift Tubes

In the barrel region the local reconstruction starts with the drift time. The conversion of the drift time into position requires the knowledge of the drift velocity. It depends on the magnetic field  $\vec{B}$  and on the impact angle of the muon with respect to the DT. The drift velocity can be obtained by two different approaches, one uses a constant drift velocity for each cell, which neglects the above mentioned dependencies. The default algorithm instead uses a parametrization, which depends on the magnetic field and the impact angle, obtained by a simulation of the cell behaviour.

The segment reconstruction in three superlayers (12 layers of drift tubes, see figure 4.5) works independently in the  $r - \phi$  and the  $r - z$  projections. The segment reconstruction, complicated by the left-right ambiguity in each cell, is done in three steps.

- Construction of a first segment candidate from a set of aligned hits,
- Selection of the best segments, resolution of conflicts and suppression of ghosts,
- Update of the reconstructed hits using the information of the reconstructed segments and eventually refitting of the segments.

The starting point in the first step are two hits in different layers, beginning with the most separated ones. The pair is kept, if the hits are compatible with a track coming

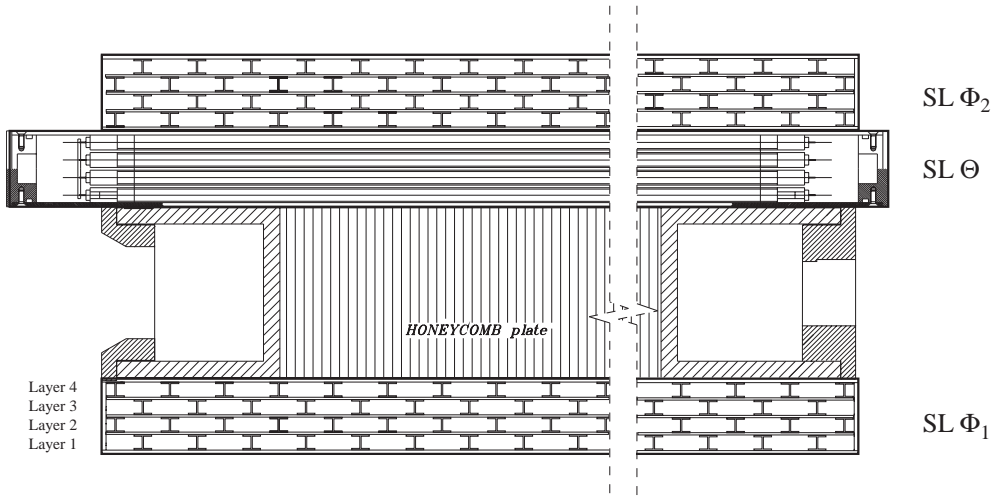


**Figure 4.5:** The layout of a DT chamber inside a muon barrel station [27].

from the nominal interaction point. Than additional compatible hits are searched for. For each collection of hits a linear fit is performed to obtain a segment candidate and the left-right ambiguity is solved through the best  $\chi^2$ . In the next step, a consistency check is done to test whether different segments are sharing the same hit. Possible conflicts are solved by using the number of hits and the  $\chi^2$  value of the involved segments. Hits belonging to the leftover candidates are updated considering the incidence angle reconstructed by the segment. Afterwards, the linear fit is redone using the collections of updated hits. At the end, the segments reconstructed in the two orthogonal projections are combined to get three dimensional segments from a final fit. The resolution of the reconstructed segments is in the order of  $\sigma_x \approx 100 \mu\text{m}$  for the position and  $\sigma_\theta \approx 1 \text{ mrad}$  for the direction. Details can be found in [27, 62, 63].

### Local Reconstruction in the Cathode Strip Chambers

For the local reconstruction in the CSCs, the detected signals from the cathode strips and the anodes wires are used. The charge distribution produced be a charged particle crossing a layer of a chamber is typically distributed over 3-5 strips.

At the beginning of the local reconstruction each of the six layers of a chamber is treated independently. The starting point is the fitting of clusters of strips. Starting from the strip, which has collected the highest charge, the cluster finding algorithm loops over all signal strips to calculate the charge centroid. To get an optimal position resolution from the strip, a Gatti distribution [64] is fitted on three adjacent strips, starting from the charge centroid, which is taken as hit position in case of a poor or failing fit. The missing coordinate to reconstruct a two dimensional hit in each layer can be obtained by searching for the intersection of each signal strip with a fired wire group. Therefore, it is required that the signal in the strips and the wire groups occur within two bunch crossings of each other.

Similar to the procedure for the barrel local reconstruction, the final step is the fitting of track segments for each CSC using the reconstructed hits in each of the six layers. The algorithm starts from the most separated hits in a chamber, connecting them with

a straight line, requiring that starting and endpoint have a  $r - \phi$  separation of not more than 1 cm. Then hits from the intermediate layers are added, if they are closer than 2.5 mm to the line in  $r - \phi$  and the  $\chi^2$  of the updated linear fit is reasonable. If more than one hit is compatible to the line, the hit which give the best fit is retained. The reconstructed track segment is kept, if there are least four hits associated with it. The associated hits are marked as used and the procedure starts again using the left over hits.

The resolution of the strip measurement for the innermost CSCs is about  $100\ \mu\text{m}$ . Due to the larger pitch of the other chambers, their resolution is about  $200\ \mu\text{m}$ . The resolution of the grouped wires with the width  $w$  is  $w/\sqrt{12}$ , which is approximately 0.7 cm [27, 62, 63].

### Local Reconstruction in the Resistive Plate Chambers

The result which can be obtained by the local reconstruction in the RPCs are just reconstructed points in the plane of the detector, since the barrel chambers have only strips in the direction of the beam pipe and the endcap chambers radially to the beam pipe. The starting point of the local reconstruction is the clusterization. All strips having a signal are considered and adjacent signal strips are combined to clusters. After the process of clusterization is finished, each reconstructed point is defined by the center of gravity of the corresponding cluster. Assuming a flat probability anywhere in the area covered by the strips of that cluster, the reconstructed point is the center of a rectangle at least for the rectangular strips in the barrel region. The errors are simply  $\sigma_i = L_i/\sqrt{12}$  ( $i = z, \phi$ ), where  $L_i$  is length of the corresponding side of the rectangle. The treatment of the endcap chambers is more complicated, due to the trapezoid structure with a variable shape [27, 63].

#### 4.3.2 Standalone Muon Reconstruction

The standalone muon reconstruction uses only the data coming from the muon system, data from the silicon tracker is not included. For the High Level Trigger, the standalone muon reconstruction is called Level 2 muon reconstruction. The reconstruction uses both muon systems, the DT and the CSC. Despite of the low spatial resolution, the reconstruction is complemented by the RPC in particular in regions with a problematic geometric coverage, which is mostly the case in the barrel-endcap overlap region.

The standalone muon reconstruction starts with the reconstructed track segments in the muon chambers, from the local reconstruction. An algorithm based on the Kalman filter technique is working from inside out. The predicted state vector (track position, momentum and direction) in next detector layer is compared with the existing measurement. The track parameters as well as their errors are updated accordingly. For the DT chambers, the reconstructed track segments obtained by the local reconstruction are used as measurements in the Kalman filter algorithm. Whereas in the endcap CSC, the reconstructed hits of the segments are used, due to the inhomogeneities of the magnet field in that region. Likewise for the RPC only reconstructed hits are included. A reasonable  $\chi^2$  cut is applied to reject fake track hits, mostly caused by showering, delta rays and pair production. If no hits or segments are found in a detector layer, e.g. due to detector inefficiencies, that station is skipped and the search is continued in the next

detector layer. To propagate the state vector from one detector layer to another, the GEANE package [65] is used. It takes into account the muon energy loss in material, the multiple scattering and the variation of the magnetic field in the muon systems. The procedure is repeated until the outermost detector layer is reached. Afterwards the procedure is reversed, working from outside in, to define the track parameters at the inner most layer of the muon system. In the last step, the track is extrapolated to the nominal interaction point and a vertex constrained fit is applied to the track parameters [27, 63].

### 4.3.3 Global Muon Reconstruction

In contrast to the standalone muon reconstruction the global muon reconstruction uses also information from the silicon tracker. The starting point of the global muon reconstruction are the standalone reconstructed muons. The muon trajectory is extrapolated from the innermost muon system to the outermost tracker layer, using the GEANE package [65]. Afterwards a region of interest in the silicon tracker is determined, taking into account track parameters and uncertainties of extrapolated muon trajectory. Additionally, it is assumed that the origin of the muon is the nominal interaction point. This constraint impacts the reconstruction efficiency, fake rate, and CPU time. Well-measured muons will be reconstructed faster and with a higher efficiency, than poorly measured ones.

Starting point for the tracking algorithm, which is based on a Kalman filter, is a regional seed formed by two hits in two different tracker layers. The following procedure of track fitting in the region of interests is same as already described in section 4.1. In the final step all reconstructed tracker tracks are fitted with the reconstructed hits from the reconstructed standalone muons and the global muons are selected by a  $\chi^2$  cut. The resulting muon tracks are called global muons or combined muons, and in case of the High Level Trigger, Level 3 muons [27, 63].

### 4.3.4 Performance

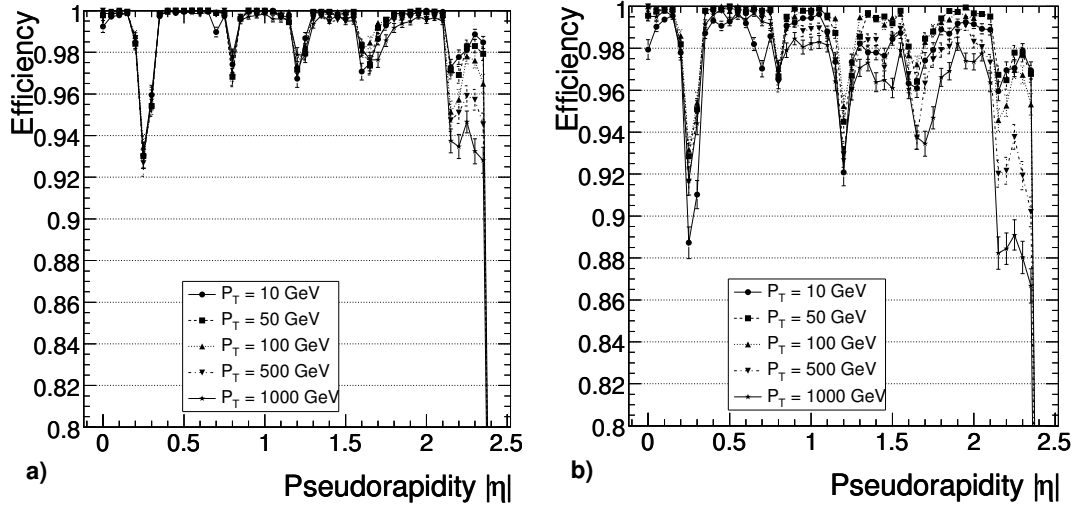
Figures 4.6 and 4.7 were obtained from an ideal detector, ignoring misalignment, miscalibration, neutron background or pile-up. Single muon datasets in the  $p_T$  range of 1-1000 GeV and with a flat distribution in  $\phi$  and  $\eta$  were used.

Figure 4.6 shows the muons reconstruction efficiency as function of  $\eta$  for different values of  $p_T$ . The reconstruction efficiency is between 95-98%, except for the gap around  $|\eta| = 0.25$ , which is the region between two wheels, the overlap region between the DT and CSC chambers around  $|\eta| = 1.2$ , and at the edge of muon system in the regions beyond  $|\eta| = 2.1$ .

The resolution of the transverse momentum, obtained by fitting a Gaussian to the distribution of the quantity

$$\frac{q^{\text{rec}}/p_T^{\text{rec}} - q^{\text{gen}}/p_T^{\text{gen}}}{q^{\text{gen}}/p_T^{\text{gen}}} \quad (4.3)$$

for standalone and global reconstructed muons is shown in figure 4.7. The resolution of the standalone muons is dominated up to 200 GeV by multiple scattering in the material before the first muon station. The resolution strongly depends on the measurement of the muon bending angle at the exit of the 4 T coil, taking the interaction



(a) Standalone muon reconstruction using only hits in the muon detectors with a vertex constraint.  
(b) Global muon reconstruction using hits from muon detectors and the tracker.

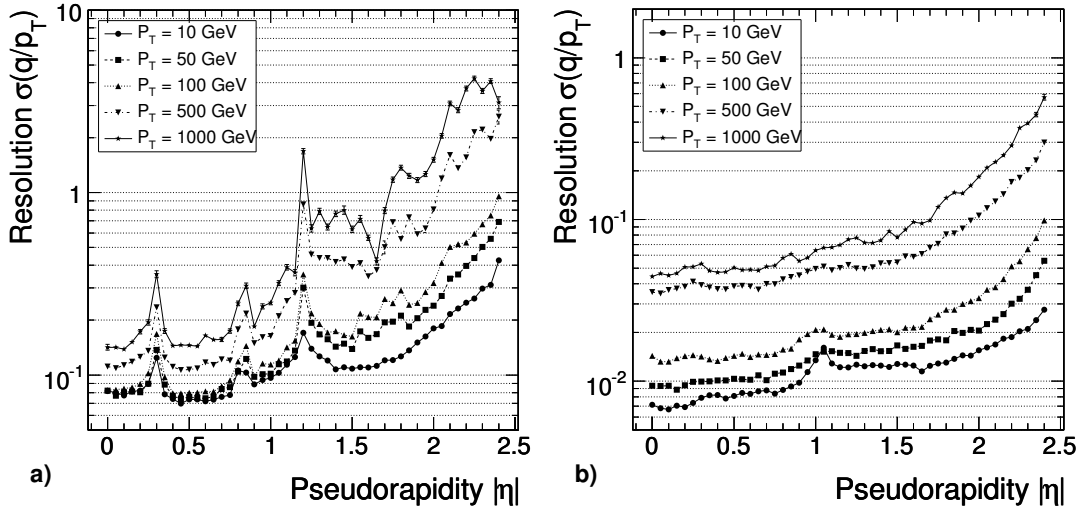
**Figure 4.6:** Muon reconstruction efficiency as a function of  $\eta$  for various values of  $p_T$  [27].

point as origin of the muon. For muons with a higher transverse momentum, the spatial resolution of the chambers is dominating (see figure 4.7(a)). For low  $p_T$  muons, the best momentum resolution can be obtained in the silicon tracker. The momentum resolution using the muons can be improved by a factor of 10 (see figure 4.7(b)) by the global reconstruction. An other important issue is the correct charge assignment to the muon. For global muons the probability to misassign the charge is below 0.1% for a muon with  $p_T = 100$  GeV. Additional plots can be found in the Appendix A.2 [27,63].

## 4.4 Alternative Muon Identification

The standard procedure of identifying muons has been discussed in the previous section. The standard algorithms always have their starting point in the muon system and are working from outside-in. That leads to a reduced reconstruction efficiency of low  $p_T$  muons and muons which are really close together in space. It is likely that low  $p_T$  muons loosing their energy already in the dense material of the calorimeters before reaching the outer muon systems. The number of the reconstructed hits in the muon system is small and a reconstruction using the standard approach is hardly possible. The issue with muons which are close together in space is a different one. The problem in this case is the matching between the reconstructed track segment in the muon system and the reconstructed track in the silicon tracker. Sometimes the assignment fails and the reconstructed segment is matched to a wrong track. That leads to a poor  $\chi^2$  of the combined fit and often to a lower  $p_T$  of the reconstructed muon.

The alternative muon identification is working in the opposite direction. It starts from a reconstructed track in the silicon tracker which is propagated through the entire detector. Various detector informations are associated with the propagated track, including energy depositions in the ECAL, HCAL and the HO. The number of matched track segments in muon system is used to calculate a muon compatibility based on a likelihood



(a) Standalone muon resolution using only hits in the muon detectors with a vertex constraint. (b) Global muon resolution using hits from muon detectors and the tracker.

**Figure 4.7:** The resolution  $(q/p_T)$  of standalone and global muons as function of  $\eta$  [27].

ratio.

The first alternative approach on muon identification was originally introduced in the last version of the old CMS software framework ORCA [66]. The muon identification presented in the following was developed because an official tool was not available in the earlier versions of CMSSW. Meanwhile a new type of muons called Tracker-Muons<sup>1</sup> have been implemented in CMSSW using a similar approach.

#### 4.4.1 Track Propagation

The reconstructed track from the silicon tracker is propagated through the entire detector using the TrackAssociator<sup>2</sup>. It includes the technical details about track propagation and it ensures that the correct geometry of the detector is used to identify all detector elements. The TrackAssociator provides access to various detector informations. In particular the energy depositions of the track in the ECAL, HCAL and HO, and the information about assigned muon segments.

The type of object used for the association of energy depositions can be chosen. Two objects are available, the high level objects called CaloTowers, used for jet reconstruction, and the RecHits, which provide low level detector information. For each type the energy deposition in the crossed cell and in a  $\Delta R$ -cone around the track direction can be calculated. Additionally, the sum of energy depositions in  $N \times N$  clusters around the crossed cell and around the maximal energy deposition can be evaluated.

To perform the association of a track with the subdetectors it is necessary to specify a track propagator. By default the SteppingHelixPropagator<sup>3</sup> is used. It is the best tested propagator in CMSSW working outside of the tracker. Beside the magnetic field, the SteppingHelixPropagator takes into account the energy loss, multiple scattering, and

<sup>1</sup><https://twiki.cern.ch/twiki/bin/view/CMS/SWGuideTrackerMuons>

<sup>2</sup><https://twiki.cern.ch/twiki/bin/view/CMS/TrackAssociator>

<sup>3</sup><https://twiki.cern.ch/twiki/bin/view/CMS/SWGuideSteppingHelixPropagator>

energy loss fluctuations. All interactions have been tuned with GEANT and theoretical predictions available. The accuracy of the propagator is limited by the modelling of the tracker and the muon chambers as diffuse material, which means that all materials are averaged over the entire volume, and the hardcoded assumption that the propagated track is a muon.

#### 4.4.2 Energy Deposition in the ECAL

The first input variable of the alternative muon identification is the energy deposition in cells of the electromagnetic calorimeter crossed by the propagated track. In order to suppress noise hits a cut of 10 MeV has been applied. Energy depositions from muons are mainly contained in the crossed cell in contrast to energy deposits of showering particles, which distribute the energy over several cells. Therefore, it is reasonable to use only energy deposits in the crossed cells as input for the likelihood ratio. The distribution of the energy deposition is depicted in figure 4.8 separately for the barrel and endcap region.

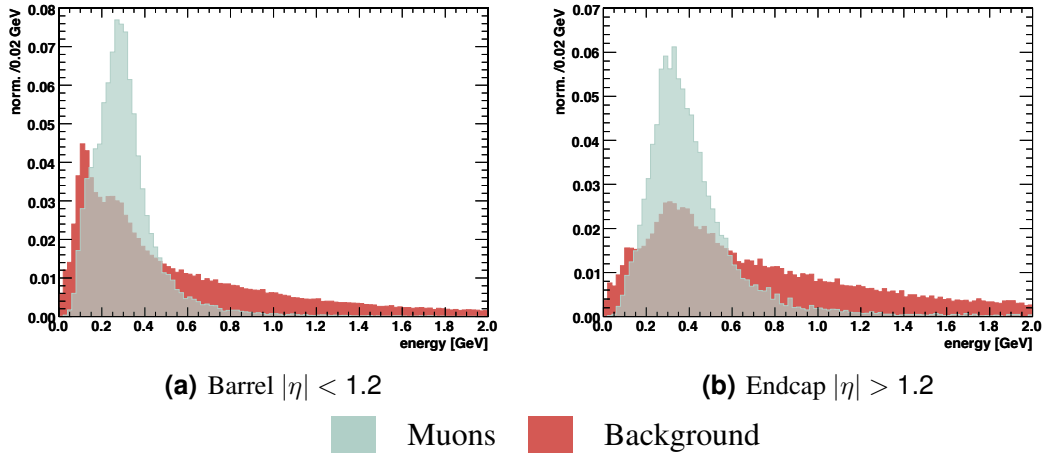


**Figure 4.8:** Associated energy deposition (normalized to integral one) of the propagated track in the electromagnetic calorimeter (crossed cells) separated into the barrel and endcap region of the detector.

A energy deposition of 300 MeV in the barrel and 400 MeV in the endcap region is expected for a minimum ionizing particle like the muon [66]. Exactly this behaviour is visible in the distributions shown in figure 4.8.

#### 4.4.3 Energy Deposition in the HCAL

The energy deposition in a cell of the hadronic calorimeter crossed by the propagated track is shown in figure 4.9. As for the electromagnetic calorimeter a cut of 10 MeV has been applied to reduce the number of noise hits.

Again, the energy deposition of the minimum ionizing muons should be contained in the crossed cell and therefore it is natural to use this observable as an input variable for the likelihood ratio.

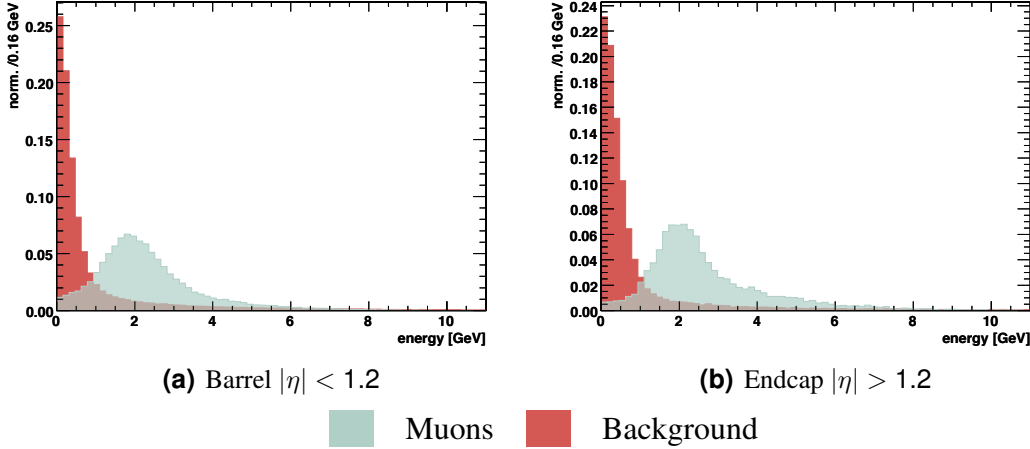


**Figure 4.9:** Associated energy deposition (normalized to integral one) of the propagated track in the hadronic calorimeter separated into the barrel and endcap region of the detector.

A muon loses about 2 GeV on average in the hadronic calorimeter, whereas background tracks loose significantly less energy in a single cell.

#### 4.4.4 Energy Deposition in the HO

In the barrel region an additional observable can be used as input variable for the likelihood ratio, the energy deposition in the outer hadronic calorimeter. Particles reaching the outer hadronic calorimeter have already passed the electromagnetic and the hadronic calorimeter as well as the coil. Most likely they are minimally ionizing.

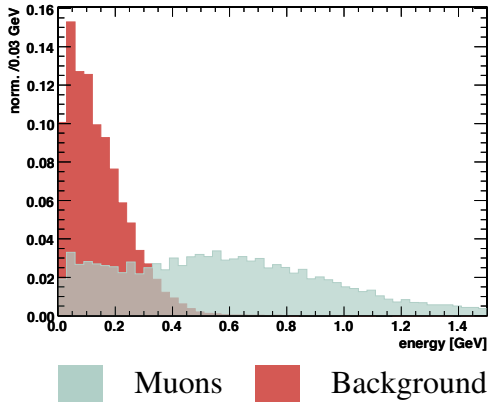


**Figure 4.10:** Associated energy deposition (normalized to integral one) of the propagated track in the outer hadronic calorimeter, which is only available in the barrel ( $|\eta| < 1.2$ ) region.

The energy deposition in the outer hadronic calorimeter is depicted in figure 4.10. To reduce noise hits a cut of 10 MeV has been applied. Muons have a broader distribution than background tracks, which are most likely punch-throughs or fake hits.

#### 4.4.5 Number of Reconstructed Muon Segments

The last input variable for the likelihood ratio is the number of reconstructed muon segments associated with the silicon tracker track. The distribution is depicted in figure 4.11.

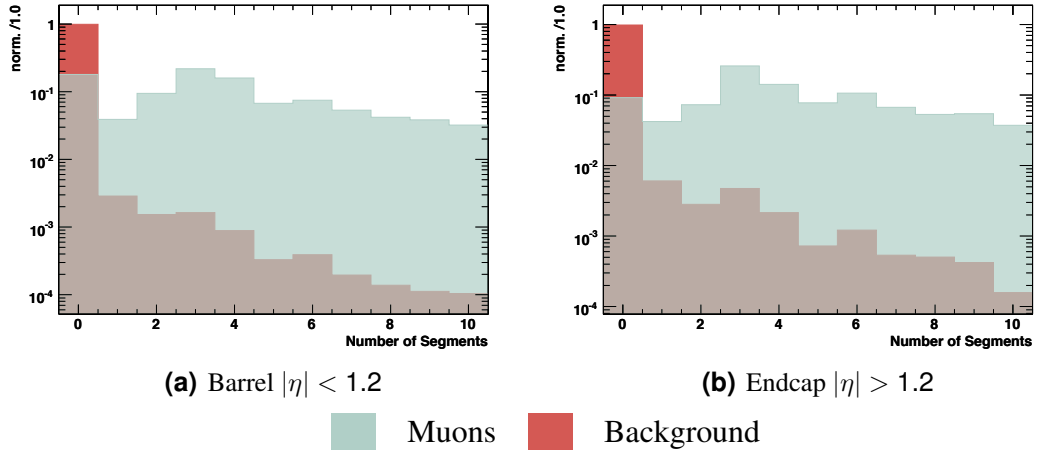


**Figure 4.11:** Number of track segments associated to the propagated track in the muon detectors separated into the barrel and endcap region.

Muons have a significant higher number of a matched reconstructed segments in the muon detector than background tracks.

#### 4.4.6 Likelihood Ratio

Considering a random variable  $x_i$  distributed according to a probability density function  $f(x_i)$ , the probability that  $x_i$  will be in the interval  $[x_i, x_i + dx_i]$  is given by  $P = f(x_i)dx_i$ . Assuming  $N$  random variables  $x_i$  which are independent from each other, than the probability that each variable  $x_i$  will be in the interval  $[x_i, x_i + dx_i]$  is given by the product

$$L = \prod_{i=1}^N f(x_i)dx_i \quad (4.4)$$

The function  $L$  is called the likelihood function [49].

The likelihood ratio, which is used to decide if an event is more signal or background like is defined as:

$$\begin{aligned} L_{\text{ratio}} &= \frac{L_{\text{signal}}}{L_{\text{Signal}} + L_{\text{Background}}} \\ &= \frac{\prod_{i=1}^N f_{\text{Signal}}(x_i)dx_i}{\prod_{i=1}^N f_{\text{Signal}}(x_i)dx_i + \prod_{i=1}^N f_{\text{Background}}(x_i)dx_i} \end{aligned} \quad (4.5)$$

This likelihood ratio can take values in the interval  $[0, 1]$ , where 0 means a track is background-like and 1 a track is signal-like.

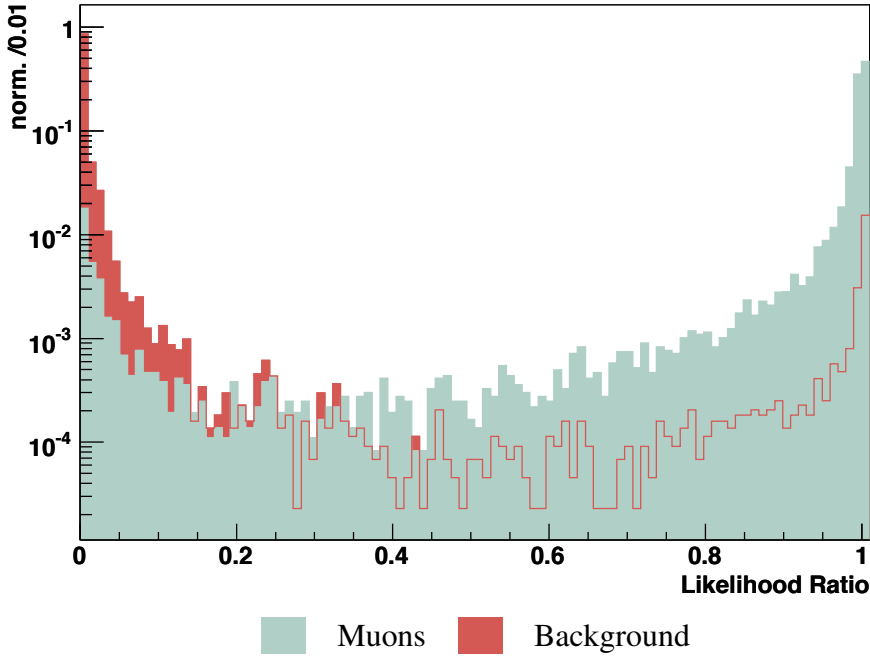


**Figure 4.12:** Distribution of the likelihood ratio with muons in light and background in dark color.

The obtained results of the alternative muon identification based on a likelihood ratio is depicted in figure 4.12. The likelihood ratio can be used to separate muons from background tracks with a high efficiency and purity. All tracks having a likelihood ratio of 0.6 or above are treated as muons. The value of the cut has been chosen by efficiency and purity optimizations.

Input Variable	Lower Cut	Upper Cut	Treatment ( $x_i >$ Upper Cut)
ECAL Energy Deposition	10 MeV	2 GeV	Background
HCAL Energy Deposition	10 MeV	11 GeV	Muon
HO Energy Deposition	10 MeV	1.5 GeV	Muon
Number of Muon Segments	-	11	Muon

**Table 4.1:** List of the applied cuts used for the likelihood ratio.

In general it is reasonable to use the likelihood ratio only in regions, where it is necessary to distinguish between signal and background. Therefore, beside the already mentioned noise reduction cuts, upper cuts have been defined. Studies have shown, that in some regions only background tracks and in other regions only signal tracks are located, these regions have been excluded from the likelihood procedure and the corresponding tracks are treated directly as background or signal. The values of the chosen cuts and the associated treatments of the tracks can be found in table 4.1.

## 4.5 Trigger

The purpose of the trigger is a fast and substantial online data reduction. Bunch crossings at the LHC take place every 25 ns, equivalent to a rate of 40 MHz. The online computing farm can only store events with a rate of up to 300 Hz. The trigger has to reduce the amount of events by roughly a factor of  $10^5$  [67, 68].

The trigger system of CMS is separated into two levels, the Level 1 trigger (L1) and the High Level Trigger (HLT). The L1 has to take a decision every 25 ns with a latency of  $3.2\ \mu\text{s}$ . It is completely based on hardware. The HLT instead is operating on a longer timescale, but still has to deal with a L1 acceptance rate of up to 100 kHz. The HLT is completely based on software, which runs on the Event Filter Farm [67, 68]. The following sections focus on the relevant muon triggers.

### 4.5.1 Level 1 Trigger

The tasks of the L1 Muon Trigger are the muon identification, the assignment of the muons to the correct beam crossing and the determination of the muon's transverse momenta and their location. Three different trigger subsystems of the muon detector are used, DTs in the barrel region, CSCs in the endcap region and the RPCs in the barrel and endcap region. At the end all results obtained from the DTs, CSCs and RPCs subsystems, and also of the calorimeter subsystems are combined by the Global Muon Trigger (GMT).

Starting point for the trigger subsystems DT and CSC is the processing of the local information for each muon and each chamber. The resulting information, which is in principle the position, the direction, the assigned bunch crossing and the quality of the muon candidate, is used by the Track Finders (TF) to produce tracks. In the overlap region between the DTs and the CSCs the information about track segments is shared. For each subsystem, the best four muon candidates with respect to quality and  $p_T$  are sent to the Global Muon Trigger. The sole local processing done in the RPCs is a cluster reduction and synchronization. Instead of local processing, the hits from all stations are collected and a muon candidate is produced if the hits are aligned along a possible muon trajectory. The  $p_T$  is assigned by comparing the observed muon candidates with predefined hit patterns for different values of  $p_T$ , which have been obtained from simulations. The four best candidates with respect to the quality and  $p_T$  are sent to the Global Muon Trigger for each barrel and endcap region.

One of the purposes of the Global Muon Trigger is the matching of DT and CSC candidates with the candidates obtained by the RPCs. If two candidates from different subsystems have a matching, they are combined to one global candidate to get the optimal precision. If no matching can be found, quality criteria are defined to decide whether the segment is kept or discarded. For the leftover candidates, informations about isolation and compatibility with a minimal ionizing particle is added using the calorimeter trigger towers. At the end, the four best muon candidates, chosen by quality and  $p_T$ , are sent to the Global Trigger [27, 68]. The trigger threshold for the low luminosity phase can be found in table 4.2.

More detailed information about the L1 Trigger can be found in [27, 67, 69].

L 1 Trigger	L1 single muon	L1 dimuon
Threshold	14 GeV	3 GeV

**Table 4.2:** *L1 Muon Trigger thresholds on  $p_T$  [27].*

### 4.5.2 High Level Trigger

The selection of muons by the High Level Trigger is done in two steps. Starting point for the first step, namely the Level 2 muon reconstruction, is the Level 1 muon seed. The Level 2 muon reconstruction uses only information from the muon system and is a confirmation of the L1 decision. The reconstruction algorithm has been described in section 4.3.2. The next step, the Level 3 muon reconstruction is seeded by the L2 muons and uses the full information available from the tracker. Since tracking is the most time consuming process, a  $p_T$  threshold is already applied to the Level 2 muon candidates in order to reduce the rate. A more detailed description of the Level 3 muon reconstruction algorithm can be found in section 4.3.3.



**Figure 4.13:** *Flowchart of the muon High Level Trigger.*

In addition to the  $p_T$  thresholds, an isolation can be required to further reduce the trigger rate, for example to lower the  $p_T$  thresholds. Calorimeter isolation can be required already at the Level 2 step, inclusion of tracker isolation is only possible after the Level 3 step.

HLT Trigger	Trigger Name	Threshold
HLT single muon (isolated)	HLT1MuonIso	19 GeV
HLT dimuon (isolated)	HLT2MuonIso	7 GeV
HLT single muon	HLT1MuonNoIso	37 GeV
HLT dimuon	HLT2MuonNoIso	10 GeV
HLT multimuon	HLTNMuonNoIso	3 GeV

**Table 4.3:** *HLT Muon Trigger  $p_T$  thresholds for the low luminosity phase*<sup>4</sup>.

The  $p_T$  thresholds applied to muons in the High Level Trigger is different for the single, the double and the multi-muon trigger. It also depends on the isolation. The  $p_T$  thresholds for low luminosity can be found in table 4.3.

### $\tau \rightarrow \mu\mu\mu$ Trigger Proposal

Since the official muon High Level Trigger is using exactly the same reconstruction algorithms as the muon reconstruction, also the HLT suffers from the issues mentioned already in section 4.4. In particular, the HLT had a problem with the matching between the reconstructed Level 2 muon and the tracker tracks, which lead to a drop of the

<sup>4</sup>The  $p_T$  thresholds for the low luminosity phase are not yet fully decided. The thresholds mentioned in table 4.3 are the thresholds as they are implemented in CMSSW\_1\_6\_12.

trigger efficiency. Therefore a dedicated  $\tau \rightarrow \mu\mu\mu$  trigger has been proposed and implemented into CMSSW\_2\_0\_x. The trigger is build on the existing displaced dimuon trigger developed by Lotte Wilke [70]. The idea to combine the two muon in this trigger with a third track was originated by Urs Langenegger [71] to trigger  $B \rightarrow \mu\mu K$  events. Within this  $\tau \rightarrow \mu\mu\mu$  study it was implemented into CMSSW\_2\_0\_x. The different steps of the  $\tau \rightarrow \mu\mu\mu$  trigger are depicted in figure 4.14.

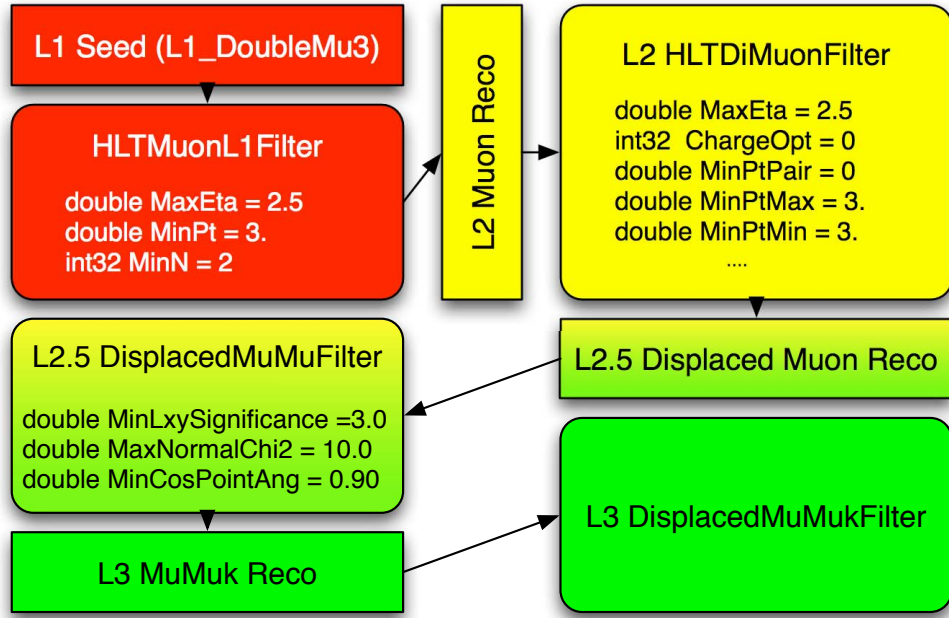


**Figure 4.14:** Flowchart of the proposed dedicated  $\tau \rightarrow \mu\mu\mu$  trigger.

Starting point is the L1 seed. It is required to have at least two muons with a transverse momentum of more than 3 GeV. The next step is the usual Level 2 muon reconstruction, which has been described in section 4.3.2. After the reconstruction it is required to have at least two muons with a  $p_T > 3$  GeV. Next the so-called Level 2.5 displaced muon reconstruction is performed. The Level 2 muon candidates are extrapolated to the silicon tracker. After the seed finding step, a track reconstruction is performed within the region of interest. A vertex fit of the two muon candidates is performed with the Kalman vertex fitter. To reduce the rate it is required that the two muon candidates are originated from the same secondary vertex ( $\chi^2 < 10$  for the vertex fit), the significance of the decay length within the xy-plane have to be  $L_{xy}/\sigma_{L_{xy}} > 3$  and the cosine of the pointing angle have to be  $\cos(p_{xy}, L_{xy}) > 0.9$ . Afterwards the Level 3 reconstruction is done, which is at moment identical to the L2.5 reconstruction. To optimize the efficiency in the future, it is possible to extend the region of interest in the L3 stage. The last step is the L3 filter, which applies the thresholds using the following fully configurable parameters.

- $-2.5 \leq \eta \leq 2.5$ ,
- $p_T \geq 3$  GeV for each track,
- $1.2 \text{ GeV} < m_{\mu\mu k} < 2.2 \text{ GeV}$ ,

- $L_{xy}/\sigma_{L_{xy}} > 3.0$  (decay length in  $xy$  plane),
- $\chi^2_{norm} < 10$  ( $\chi^2_{norm}$  of a Kalman vertex fit),
- $\cos(p_{xy}, L_{xy}) > 0.9$  (pointing angle),
- $m_k = 0.106$  GeV (input mass of the 3rd track).

A more detailed flowchart of the algorithm used is shown in figure 4.15.

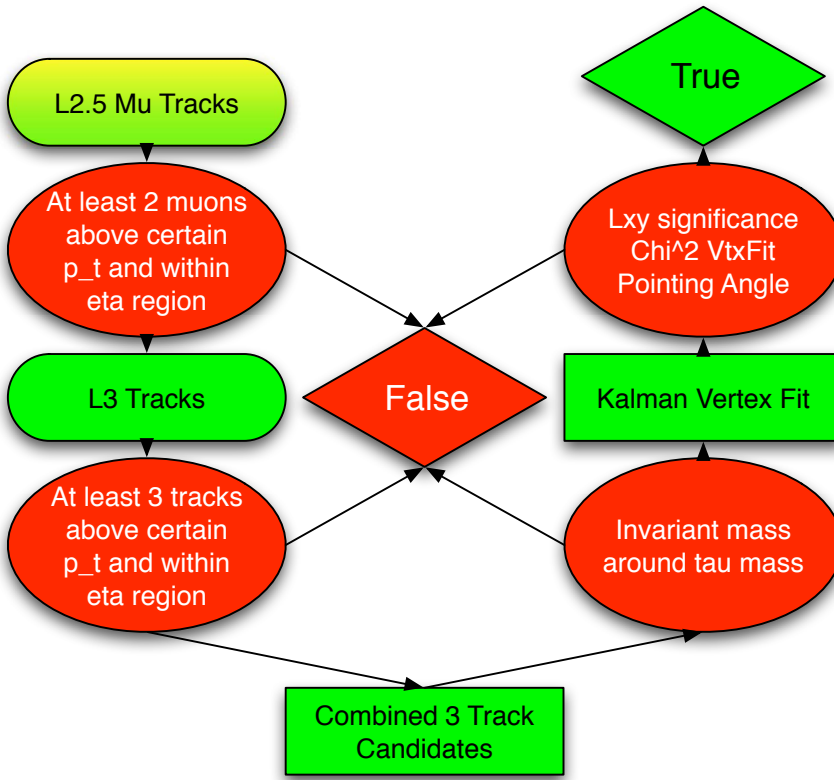


**Figure 4.15:** Detailed flowchart of the  $\tau \rightarrow \mu\mu\mu$  trigger algorithm.

Meanwhile the matching routine of the official muon High Level Trigger was improved and the efficiency has been doubled. But for  $\tau \rightarrow \mu\mu\mu$  decays originated by  $D_s$  and  $B$  mesons, the trigger  $p_T$  thresholds are still to high, so that the  $\tau \rightarrow \mu\mu\mu$  trigger can be of benefit. The trigger is meanwhile part of the official trigger menu for the startup phase of the LHC, but still needs further tuning to be competitive. Due to the lack of datasets available for CMSSW\_2\_0\_x, the  $\tau \rightarrow \mu\mu\mu$  trigger is not included in the further analysis.

# Chapter 5

## Implementation of $\tau \rightarrow \mu\mu\mu$ in the Event Generator

Since the decay  $\tau \rightarrow \mu\mu\mu$  is not implemented in the Monte Carlo event generator PYTHIA, the decay table has to be modified to add this new  $\tau$  decay. To take into account angular distributions the matrix element has been implemented into CMSSW and PYTHIA is modified through CMSSW.

### 5.1 Adding the Decay $\tau \rightarrow \mu\mu\mu$

The easiest way to implement the lepton flavour violating  $\tau$  decay  $\tau \rightarrow \mu\mu\mu$  in PYTHIA is to extend the existing  $\tau$  decay table by one additional decay channel. The range of

particle	ID decay channel	Matrixelement	Branching Ratio	decay products
$\tau$	89	42	0.178300	$e\nu_e\nu_\tau$
	$\vdots$	$\vdots$	$\vdots$	$\vdots$
	140	102	0.0	$Z_0\tau$
	141	102	0.0	$W\nu_\tau$
	142	102	0.0	$h_0\tau$
$\nu_\tau$	143	102	0.0	$Z_0\nu_\tau$
	144	102	0.0	$W\tau$

**Table 5.1:** Extract of the PYTHIA decay table before modification.

the decay table for a certain decay is defined by two parameters, the entry point and the number of total decay channels. It is necessary to have all  $\tau$  decays in one block starting from decay channel ID 89, the default entry point for  $\tau$  decays. The variable `MDCY(15, 2)=89` has to be used to set the entry point, whereby 15 is the particle ID of the  $\tau$  lepton. By default the number of total decay channels is 54, since one decay should be added, one has to set it to 55, which is possible by setting the variable `MDCY(15, 3)=55`. The new  $\tau$  decay channel with ID 143 is already used in the decay table of  $\nu_\tau$ , therefore it is necessary to move the  $\nu_\tau$  block to a free range within the decay table. Usual decay ID's starting from 4300 can be used for this purpose.

particle	ID decay channel	Matrixelement	Branching Ratio	decay products
$\tau$	89	42	0.178300	$e\nu_e\nu_\tau$
	:	:	:	:
	140	102	0.0	$Z_0\tau$
	141	102	0.0	$W\nu_\tau$
	142	102	0.0	$h_0\tau$
	143	0	1.0	$\mu\mu\mu$
$\nu_\tau$	4300	102	0.0	$Z_0\nu_\tau$
	4301	102	0.0	$W\tau$

**Table 5.2:** Extract of the PYTHIA decay table after modification.

The decay itself can be implemented using following PYTHIA variables:

```
KFDP(143,1)=13
KFDP(143,2)=-13
KFDP(143,3)=13
KFDP(143,4)=0
KFDP(143,5)=0
```

PYTHIA provides decays to up to five daughter particles. To set up the  $\tau \rightarrow \mu\mu\mu$  decay only three of them are needed. 13 is the particle ID for a muon and  $-13$  its antiparticle.

In the last step the matrix element and the branching ratio of the new decay have to be chosen. PYTHIA provides the variables `MDME(143,2)` and `BRAT(143)` for this purpose. It is useful to set the branching ratio of that decay to one using `BRAT(143)=1.0`, since it is desirable to produce a signal sample with high efficiency. For the  $Z \rightarrow \tau^+\tau^-$  source a separate production for the particle and anti-particle decaying into three muons is mandatory to avoid a lepton flavour violating decay of both  $\tau$  leptons. Therefore, the previous  $\tau$  decay channels including their branching ratios are kept and the lepton flavour violating decay of one  $\tau$  lepton is forced by enabling the  $\tau \rightarrow \mu\mu\mu$  decay channel using the `MDME(143,1)` parameter and at the same time disabling all other decay modes. Since there is no appropriate matrix element in PYTHIA, we set `MDME(143,2)=0`. PYTHIA will simulate pure phase space with a flat angular distribution.

A complete implementation in terms of a CMSSW configuration file segment can be found in the Appendix A.1.1.

## 5.2 The Matrix Element

Beyond the Standard Model a large number of theoretical models give rise to lepton flavour violation in the range of current experimental limits. Not to be limited to one specific model, the matrix element has been calculated in a model independent way by a group of RWTH theory department and a group at the University of Siegen [8, 72].

For that calculation an effective four-fermion interaction also known as a contact interaction was considered.

The effective Lagrangian is given by

$$\begin{aligned}
 \mathcal{L} = & G \left( g_{LL}^S (\bar{\mu} P_R \mu) (\bar{\mu} P_L \tau) + g_{LR}^S (\bar{\mu} P_R \mu) (\bar{\mu} P_R \tau) + g_{RL}^S (\bar{\mu} P_L \mu) (\bar{\mu} P_L \tau) + g_{RR}^S (\bar{\mu} P_L \mu) (\bar{\mu} P_R \tau) \right. \\
 & + g_{LL}^V (\bar{\mu} \gamma_\nu P_R \mu) (\bar{\mu} \gamma^\nu P_L \tau) + g_{LR}^V (\bar{\mu} \gamma_\nu P_R \mu) (\bar{\mu} \gamma^\nu P_R \tau) \\
 & + g_{RL}^V (\bar{\mu} \gamma_\nu P_L \mu) (\bar{\mu} \gamma^\nu P_L \tau) + g_{RR}^V (\bar{\mu} \gamma_\nu P_L \mu) (\bar{\mu} \gamma^\nu P_R \tau) \\
 & \left. + g_{LR}^T \left( \bar{\mu} \frac{\sigma^{\rho\nu}}{\sqrt{2}} P_R \mu \right) \left( \bar{\mu} \frac{\sigma^{\rho\nu}}{\sqrt{2}} P_R \tau \right) + g_{RL}^T \left( \bar{\mu} \frac{\sigma^{\rho\nu}}{\sqrt{2}} P_L \mu \right) \left( \bar{\mu} \frac{\sigma^{\rho\nu}}{\sqrt{2}} P_L \tau \right) \right) \\
 \equiv & G \sum_{a,b,c} g_{ab}^c (\bar{\mu} \Gamma^c \gamma^0 P_a \gamma^0 \mu) (\bar{\mu} \Gamma^c P_b \tau) \tag{5.1}
 \end{aligned}$$

Using  $\rho$  and  $\nu$  as Lorentz indices to avoid confusion with the symbol  $\mu$  being used for the muon spinors.  $P_{L/R} = (1 \mp \gamma^5)/2$  are left- and right-handed projection operators and  $\sigma^{\rho\nu} = i[\gamma^\rho, \gamma^\nu]/2$ .

The symbols  $g_{ab}^c$  label the couplings for the various chiral structures. The index  $c$  denotes the structure of the coupling  $S$  for scalar,  $V$  for vector and  $T$  for tensor couplings, so that  $\Gamma^S = 1$ ,  $\Gamma^V = \gamma^\nu$  and  $\Gamma^T = \sigma^{\rho\nu}/\sqrt{2}$ . The index  $a = \{L, R\}$  identifies the chirality of the anti-muon, since it is unambiguous to consider the anti-muon in the  $\tau^-$  decay. The index  $b = \{L, R\}$  labels the chirality of the  $\tau$  lepton.

The constant  $G$  is dimensionful, with units of  $\text{GeV}^{-2}$ . It is used to absorb any normalization of the couplings  $g_{ab}^c$  for any particular model, so that the  $g_{ab}^c$  are dimensionless numbers.

Considering that there is a pair of identical fermions in the final state, the transition matrix element is given by

$$\begin{aligned}
 \mathcal{M} = & G \sum_{a,b,c} g_{ab}^c \left( \bar{u}_{(p_{\mu_a})} \Gamma^c \gamma^0 P_a \gamma^0 \nu_{(p_{\bar{\mu}})} \bar{u}_{(p_{\mu_b})} \Gamma^c P_b u_{(p_\tau)} \right. \\
 & \left. - \bar{u}_{(p_{\mu_b})} \Gamma^c \gamma^0 P_a \gamma^0 \nu_{(p_{\bar{\mu}})} \bar{u}_{(p_{\mu_a})} \Gamma^c P_b u_{(p_\tau)} \right) \tag{5.2}
 \end{aligned}$$

$A$  and  $B$  denotes the two muons. While summing over the final state spins when squaring the matrix element, the information about the  $\tau$  polarization are kept by using  $u_{(p_\tau)} \bar{u}_{(p_\tau)} = (\not{p} + m_\tau) (1 + \gamma^5 \not{n}/2)$ , whereby  $n^\nu$  is the polarization vector of the  $\tau$  lepton.

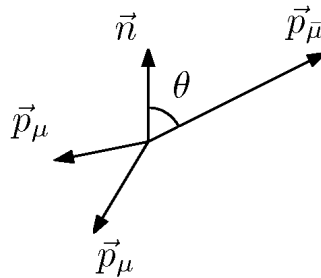


**Figure 5.1:** Definition of  $\theta$  as the angle between the  $\tau$  polarization vector  $\vec{n}$  and the momentum vector of  $\bar{\mu}$

After squaring the matrix element and integration over phase space except for the anti-muon energy and the angle  $\theta$  between the polarization of the  $\tau$  lepton and the momentum of the anti-muon, the following result for the normalized double-differential decay width is obtained:

$$\frac{1}{\Gamma} \frac{d\Gamma}{dxd\cos\theta} = \frac{6x^2(a + bx + c\cos\theta + dx\cos\theta)}{(4a + 3b)} \quad (5.3)$$

The mass of the muons is neglected and  $x = 2E_{\bar{\mu}}/m_{\tau}$  is the reduced energy of the anti-muon. The coefficients  $a, b, c$  and  $d$  are given by

$$\begin{aligned} a &= 3|g_{LL}^S|^2 + 12|g_{LL}^V|^2 + 3|g_{LR}^S|^2 + 48|g_{LR}^V|^2 + 108|g_{LR}^T|^2 + 3|g_{RL}^S|^2 + 48|g_{RL}^V|^2 \\ &\quad + 108|g_{RL}^T|^2 + 3|g_{RR}^S|^2 + 12|g_{RR}^V|^2 - 12\text{Re}(g_{LL}^S g_{LL}^{V*} + g_{RR}^V g_{RR}^{S*}) \\ &\quad - 36\text{Re}(g_{LR}^S g_{LR}^{T*} + g_{RL}^S g_{RL}^{T*}) \\ b &= -2|g_{LL}^S|^2 - 8|g_{LL}^V|^2 - 3|g_{LR}^S|^2 - 48|g_{LR}^V|^2 - 108|g_{LR}^T|^2 - 3|g_{RL}^S|^2 - 48|g_{RL}^V|^2 \\ &\quad - 108|g_{RL}^T|^2 - 2|g_{RR}^S|^2 - 8|g_{RR}^V|^2 + 8\text{Re}(g_{LL}^S g_{LL}^{V*} + g_{RR}^V g_{RR}^{S*}) \\ &\quad + 36\text{Re}(g_{LR}^S g_{LR}^{T*} + g_{RL}^S g_{RL}^{T*}) \\ c &= |g_{LL}^S|^2 + 4|g_{LL}^V|^2 - 3|g_{LR}^S|^2 - 48|g_{LR}^V|^2 - 108|g_{LR}^T|^2 + 3|g_{RL}^S|^2 + 48|g_{RL}^V|^2 \\ &\quad + 108|g_{RL}^T|^2 - |g_{RR}^S|^2 - 4|g_{RR}^V|^2 - 4\text{Re}(g_{LL}^S g_{LL}^{V*} - g_{RR}^V g_{RR}^{S*}) \\ &\quad + 36\text{Re}(g_{LR}^S g_{LR}^{T*} - g_{RL}^S g_{RL}^{T*}) \\ d &= -2|g_{LL}^S|^2 - 8|g_{LL}^V|^2 + 3|g_{LR}^S|^2 + 48|g_{LR}^V|^2 + 108|g_{LR}^T|^2 - 3|g_{RL}^S|^2 - 48|g_{RL}^V|^2 \\ &\quad - 108|g_{RL}^T|^2 - 2|g_{RR}^S|^2 + 8|g_{RR}^V|^2 + 8\text{Re}(g_{LL}^S g_{LL}^{V*} - g_{RR}^V g_{RR}^{S*}) \\ &\quad - 36\text{Re}(g_{LR}^S g_{LR}^{T*} - g_{RL}^S g_{RL}^{T*}) \end{aligned} \quad (5.4)$$

The normalized decay width in  $\cos\theta$  is given by:

$$\frac{1}{\Gamma} \frac{d\Gamma}{d\cos\theta} = \frac{1}{2} \left( 1 + \frac{4c + 3d}{4a + 3b} \cos\theta \right) \quad (5.5)$$

The same coefficients  $a, b, c$  and  $d$  as already mentioned in (5.4) are used and  $\Gamma$  labels here only the decay width of  $\tau \rightarrow \mu\mu\mu$  to save subscripts.

$$\Gamma = \frac{G^2 m_{\tau}^5}{192\pi^3} \cdot \frac{4a + 3b}{6} \quad (5.6)$$

The normalized differential decay width is independent of the absolute magnitudes of the four-fermion couplings. Muon mass effects are included in the full calculation. They are suppressed by powers of  $m_{\mu}/m_{\tau}$  and therefore numerically small. [8]

The transition matrix element is technically implemented as an object written in C++. It can be used within the CMS software framework. To compute the matrix elements following variables are required: the four vector of the  $\tau$  lepton  $p_{\tau}$ , the polarization vector  $n$  of the  $\tau$ , the four vectors of the muons in the  $\tau$  rest frame  $p_{\mu_i}$ , the global factor  $G$  and a set of coupling constants  $g_{ab}^c$  according to the considered model.

## 5.3 Treatment of the $\tau$ Polarization

Since PYTHIA does not provide information on the  $\tau$  polarization regardless of the production process, it has to be implemented into the simulation chain. We consider only  $\tau$  leptons produced in decays of electroweak gauge bosons. The majority of them come from  $W$  decays. The decay  $W^- \rightarrow \tau \bar{\nu}_\tau$  produces almost exclusively  $\tau$  leptons with left-handed helicity, due to parity violation in the couplings of  $\tau$  lepton to the  $W^-$  boson. To be exact only the chirality is determined by the charged current weak interaction. Helicity and chirality are different for massive particles. Neglecting this difference which is in the order of  $m_\tau^2/m_W^2$ , all  $\tau$  leptons produced by  $W^-$  bosons have a polarization vector antiparallel to their momentum vector and parallel for the  $W^+$ .

Considering the neutral current interaction via the  $Z$  boson exchange, the treatment of the  $\tau$  polarization is more complicated. The coupling of the  $Z$  to fermions does not have a pure  $1 - \gamma^5$  structure as for the  $W$ . The structure is  $v_f - a_f \gamma^5$ , where  $v_f$  is the vector coupling constant and  $a_f$  the axial coupling constant to fermions. The polarization of the  $\tau$  leptons is more complex. The proper way of calculating the spin state of the  $\tau$  leptons is a rigorous treatment through the spin density matrix. However in the case of production and decay of particles in the ultra relativistic limit a simplified approach is sufficient. Such an approach was developed for the KORALZ Monte-Carlo program [73]. The Monte-Carlo package TAUOLA, which decays  $\tau$  leptons including spin effects, is also using that approach taking the initial spin state of the  $\tau$  from the HEPEVT common block filled by the event generator used [74]. The approximation

Origin	$P_{\tau^+}$	$P_{\tau^-}$	Probability
Charged vector boson: $W^\pm$	$P_{\tau^+} = +1$	$P_{\tau^-} = -1$	1.0
Neutral vector boson: $Z/\gamma^*$	$P_{\tau^+} = +1$	$P_{\tau^-} = -1$	$P_Z$
	$P_{\tau^+} = -1$	$P_{\tau^-} = +1$	$1 - P_Z$
Other	$P_{\tau^+} = +1$	$P_{\tau^-} = -1$	0.5
	$P_{\tau^+} = -1$	$P_{\tau^-} = +1$	0.5

**Table 5.3:** Probability for the configurations of the longitudinal polarization of the pair of  $\tau$  leptons from different origins [75].

reconstructs information of the elementary  $2 \rightarrow 2$  body process  $q\bar{q} \rightarrow \tau^+\tau^-$ , inside a multi body process. The approach is limited to the longitudinal spin degrees only. It is randomly generated as specified in table 5.3.

The probability  $P_Z$  is calculated from the squares of the matrix element of the Born level  $2 \rightarrow 2$  process  $f\bar{f} \rightarrow \tau^+\tau^-$ , where  $f = e, \mu, u, d, c, s, b$ .

$$P_Z = \frac{|\mathcal{M}|_{f\bar{f} \rightarrow \tau^+\tau^-}^2 (+, -)}{|\mathcal{M}|_{f\bar{f} \rightarrow \tau^+\tau^-}^2 (+, -) + |\mathcal{M}|_{f\bar{f} \rightarrow \tau^+\tau^-}^2 (-, +)} \quad (5.7)$$

It can be also expressed with the help of the vector and axial couplings of fermions to

the  $Z$  boson.

$$P_Z(s, \theta) = \frac{\frac{d\sigma_{Born}}{d\cos\theta}(s, \cos\theta; +1)}{\frac{d\sigma_{Born}}{d\cos\theta}(s, \cos\theta; +1) + \frac{d\sigma_{Born}}{d\cos\theta}(s, \cos\theta; -1)} \quad (5.8)$$

$$\begin{aligned} \frac{d\sigma_{Born}}{d\cos\theta}(s, \cos\theta; p) &= (1 + \cos^2\theta) F_0(s) + 2\cos\theta F_1(s) \\ &\quad - p [(1 + \cos^2\theta) F_2(s) + 2\cos\theta F_3(s)] \end{aligned} \quad (5.9)$$

with the four form factors

$$\begin{aligned} F_0(s) &= \frac{\pi\alpha^2}{2s} \left( q_f^2 q_\tau^2 + 2\text{Re}\chi(s) q_f q_\tau v_f v_\tau + |\chi(s)|^2 (v_f^2 + a_f^2) (v_\tau^2 + a_\tau^2) \right) \\ F_1(s) &= \frac{\pi\alpha^2}{2s} \left( 2\text{Re}\chi(s) q_f q_\tau a_f a_\tau + |\chi(s)|^2 2v_f a_f 2v_\tau a_\tau \right) \\ F_2(s) &= \frac{\pi\alpha^2}{2s} \left( 2\text{Re}\chi(s) q_f q_\tau v_f a_\tau + |\chi(s)|^2 (v_f^2 + a_f^2) 2v_\tau a_\tau \right) \\ F_3(s) &= \frac{\pi\alpha^2}{2s} \left( 2\text{Re}\chi(s) q_f q_\tau a_f a_\tau + |\chi(s)|^2 (v_\tau^2 + a_\tau^2) 2v_f a_f \right) \end{aligned}$$

and

$$\chi(s) = \frac{s}{s - M_Z^2 + is\frac{\Gamma_Z}{M_Z}}$$

The angle  $\theta$  denotes the  $\tau^-$  scattering angle in the  $Z$  rest frame. It is calculated with respect to the  $e^-$ ,  $u$  or  $d$  effective beam. The  $Z$  mass is  $m_Z = 91.1882 \text{ GeV}$ ,  $\Gamma_Z = 2.49 \text{ GeV}$ ,  $\sin^2\theta_W = 0.23147$  [18] and the couplings of fermions to the  $Z$  and their numerical values are denoted in table 5.4.

Flavour: $f$	$q_f$	$v_f$	$a_f$
Leptons: $f = e, \mu, \tau$	1	$\frac{-1+4\sin^2\theta_W}{4\sin\theta_W\cos\theta_W} = -0.044$	$-\frac{1}{4\sin\theta_W\cos\theta_W} = -0.593$
Quarks: $f = u, c$	$2/3$	$\frac{1-\frac{8}{3}\sin^2\theta_W}{4\sin\theta_W\cos\theta_W} = 0.227$	$\frac{1}{4\sin\theta_W\cos\theta_W} = 0.593$
Quarks: $f = d, s, b$	$-1/3$	$\frac{-1+\frac{4}{3}\sin^2\theta_W}{4\sin\theta_W\cos\theta_W} = -0.410$	$-\frac{1}{4\sin\theta_W\cos\theta_W} = -0.593$

**Table 5.4:** The  $Z$  couplings to fermions. Lowest order approximation, the numerical values are given for the effective  $\sin^2\theta_W = 0.23147$  [75]

The  $\tau$  lepton polarization as a function of  $\cos\theta$  for different values of  $\sqrt{s}$  is depicted in figure 5.2. In 5.2(a) the distribution for up-type quarks is shown and in 5.2(b) that for down-type quarks.

For a center-of-mass energy around the  $Z$  boson mass, the  $\tau$  leptons produced in the forward as well as in the backward direction are strongly polarized. The polarization for  $\cos\theta = 0$  is close to zero. At the  $Z$  peak the contribution of  $\gamma$  exchange is rather small. The initial state couplings affects only the angular distribution of the  $\tau$  polarization and it leads to an angular asymmetry of the polarization. The larger the initial state vector couplings, the larger the angular dependence of the polarization.

For center-of-mass energies above the  $Z$  peak, the picture is quite different. The non-neglectable  $\gamma$  exchange as well as the  $\gamma - Z$  interference lead to a more complicated pattern. The polarization is negative and nearly constant over the forward hemisphere. For the high energy limit the polarization approaches zero in case of  $d\bar{d} \rightarrow \tau^+\tau^-$ . [75]

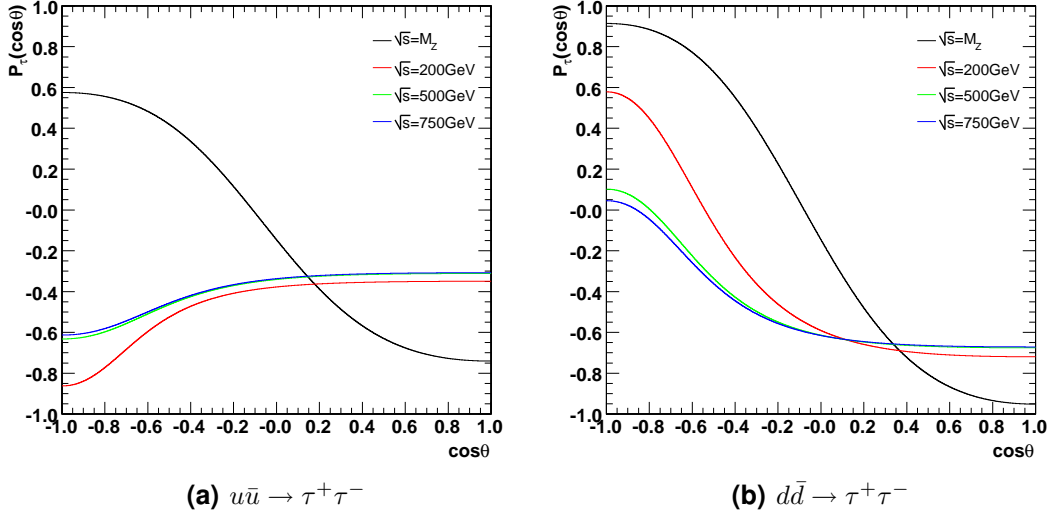


**Figure 5.2:** The  $\tau$  lepton polarization as a function of  $\cos\theta$  for different values of  $\sqrt{s}$ .

## 5.4 Implementation into CMSSW

Two things have to be implemented into CMSSW, the treatment of the  $\tau$  polarization and the matrix element of the decay. There are several ways to do it. Polarization and the matrix element can be implemented directly into the Monte Carlo generator, which is PYTHIA for the time being. Like most of the Monte Carlo generators, PYTHIA<sup>1</sup> still relies on the FORTRAN programming language. Therefore, it would be necessary to technically port the matrix element from C++ to FORTRAN. However, the main disadvantage is that this implementation would be limited to PYTHIA and would not be reusable for other generators.

The preferable alternative is to use the generator to simulate events according to the phase space distribution and to select them afterwards according to the matrix element by using a filter module. CMSSW itself provides the possibility to filter events by user criteria using a module called EDFilter. Since CMSSW is based on C++, the already available matrix element implementation can be easily used. This method is not limited to a specific generator.

### 5.4.1 Implementation of the $\tau$ Polarization

In case of the  $\tau$  production via charged current interaction the produced  $\tau$  leptons are fully polarized according to section 5.3. The polarization vector  $n$  is a four vector, that has an absolute value of one and a time-like component equal to zero. The space-like component of the polarization vector is parallel or anti-parallel to the momentum vector of the  $\tau$  in the  $W$  or  $Z$  rest frame. The following polarisation vector is used for  $\tau$  leptons produced by  $W$  bosons:

$$n = \begin{pmatrix} 0 \\ q_\tau \cdot \frac{\vec{p}_\tau}{|\vec{p}_\tau|} \end{pmatrix} \quad (5.10)$$

<sup>1</sup>The new PYTHIA version 8 has been ported to C++, but it is not yet validated for use in CMS

$q_\tau$  labels the charge of the  $\tau$  lepton.

The implementation in case of  $\tau$  production via neutral current interaction is more complicated. The probability to produce a  $\tau$  with a certain spin state is given in table 5.3. The probability is  $P_z$  for  $Z \rightarrow \tau_L^+ \tau_R^-$  and  $1 - P_z$  for  $Z \rightarrow \tau_R^+ \tau_L^-$ .  $P_z$  depends on the center-of-mass energy as well as on the decay angle  $\theta$ . To calculate the probability  $P_z$  the cross-section at Born level has to be calculated (see eq. 5.9).

This calculation is already implemented in TAUOLA as a FORTRAN function called `T_BORN`, so the easiest way is to use that function also in C++ or rather to use the FORTRAN function `PLZAP0` of TAUOLA, which calculates  $P_z$  directly. The code of `PLZAP0` and its subroutines are compiled with a usual FORTRAN compiler like `f77`. Afterwards the code can be used in C++ as an external function by linking C++ objects and FORTRAN objects properly:

```
extern "C" {
    double plzap0_(int* ide, int* idf, double* svar, double* costh0);
}
```

The parameters used are the PID of the initial state quarks producing the  $Z$  (`ide`), the PID of the final state  $\tau$  lepton (`idf`), the square of the center-of-mass energy and the cosine of the decay angle  $\theta$ . Due to how FORTRAN functions are called, it is necessary to pass the arguments from C++ by reference and not by value.

Afterwards the spin states of the  $\tau$  pair can be generated according to table 5.3 by using a hit-and-miss method. The polarization vector after that is given by

$$n = \begin{pmatrix} 0 \\ S \cdot \frac{\vec{p}_\tau}{|\vec{p}_\tau|} \end{pmatrix} \quad (5.11)$$

where  $S = \{-1, 1\}$  labels the spin state of the considered  $\tau$ .

### 5.4.2 Implementation of the Matrix Element

The calculation of the transition matrix element for the decay  $\tau \rightarrow \mu\mu\mu$  is realized as a C++ class. It can be included easily in CMSSW. CMSSW provides the possibility to filter events by using a derived class from `edm::EDFilter`. Each of these filters has a member function `filter`, which is called once per event and offers the possibility to return a true or false in case the event should be taken or not. The steering of the filter is done by a configuration file, where one can add parameters, that should be passed to the filter. In case of the matrix element implementation, a normalization factor and the specific model can be chosen.

A squared matrix element is descriptively a probability that a given combination of four vectors contributes to the total decay. The values of the matrix element range from zero to a maximum, which is characteristic for a given model. To optimize the generation according to a certain model, it is useful to treat the matrix element as a probability within an interval of  $[0, 1]$ . A normalization factor is needed. That factor is difficult to obtain analytically. Thus it is determined from the Monte Carlo generation itself. A large number of events were generated to find the maximum value of the matrix element. The obtained normalization factors are listed in table 5.5. Finally, the implementation is run once more using the hit-and-miss method to decide whether a event should be accepted or not.

The coupling constants used to evaluate the matrix element for the various studied models described in chapter 1 are listed in table 5.6.

Model	Normalization factor	Configuration parameter
R-Parity violating SUSY	$1.4 \cdot 10^4$	RPVSUSYLL (RR)
SUSY Seesaw	$3.6 \cdot 10^3$	SUSYSEESAW
Topcolor assisted Technicolor	$1.1 \cdot 10^2$	Technicolor
Little Higgs Model	$1.6 \cdot 10^3$	LittleHiggs
Top pion	$1.1 \cdot 10^4$	TopPion
Higgs triplet	$1.8 \cdot 10^3$	HiggsTriplet
Zee-Babu	$1.8 \cdot 10^3$	ZeeBabu

**Table 5.5:** Normalization factors for different models obtained using 100000 events.

Model	Coupling Constant
SUSY Seesaw	$g_{RR}^S = 1$
Higgs Triplet	$g_{RL}^V = 1$
Little Higgs	$g_{LL}^V = g_{RR}^V = 1$ or $g_{RL}^V = 1$
RPV SUSY (LL couplings)	$g_{LL}^S = 1$
RPV SUSY (RR couplings)	$g_{RR}^S = 1$
Technicolor	$g_{RL}^V = 1$ , $g_{LL}^V = g_{RR}^V = 2$ and $g_{LR}^V = 4$
Top Pion	$g_{LL}^S = g_{RR}^S = 1$ and $g_{RL}^S = g_{LR}^S = 1$
Zee-Babu	$g_{LR}^V = 1$

**Table 5.6:** The coupling constants used in the generic matrix element implementation for various studied models.

## 5.5 Results for Various Models

Since new physics models can affect physical observables like the angular distribution and the  $p_T$  distribution, it is advisable to study their influence on the detection with the CMS detector. This study is intended to get a first impression on that effects, thus it is limited to generator level so far. The following cuts are applied to the Monte Carlo data to estimate detector effects and to find the detector acceptance for the different models. The detector will be able to reconstruct muons with  $|\eta_\mu| < 2.5$  and  $p_{T_\mu} > 3 \text{ GeV}$ . For trigger purposes either 2 muons with  $p_{T_\mu} > 7 \text{ GeV}$  or one muon that passes the  $p_{T_\mu} > 19 \text{ GeV}$  threshold are required. The  $p_T$ ,  $\eta$  distribution and the distance in  $\Delta R$  between the muons are studied to evaluate the influence on the detection. Details concerning the considered models can be found in chapter 1.

The acceptance of CMS for the studied models is shown in table 5.7. The acceptance varies from 27.0% to 28.0% for the  $W$  source, and from 32.2% to 33.2% for the  $Z$  source, respectively. The different assumed models leading to the  $\tau \rightarrow \mu\mu\mu$  decay have no significant impact on the simulated acceptance of CMS. Hence a treatment with special matrix elements is not necessary.

Model	Acceptance ( $W$ source)	Acceptance ( $Z$ source)
Pure Phase Space	27.1%	32.2%
SUSY Seesaw	27.0%	32.5%
Higgs Triplet	28.0%	33.0%
Little Higgs	27.9%	32.8%
RPV SUSY (LL couplings)	27.7%	33.2%
RPV SUSY (RR couplings)	27.0%	32.5%
Technicolor	27.3%	32.8%
Top Pion	27.6%	32.7%
Zee-Babu	27.0%	32.6%

**Table 5.7:** CMS detector acceptance on Monte Carlo level for various studied models.

The angular distributions obtained for various studied models are depicted in figure 5.3 and 5.3, respectively.

### 5.5.1 Influence on the Detection Power

Now we estimate the influence of the various models on the detection power of CMS. To do that, the relevant observables for the observation of the  $\tau \rightarrow \mu\mu\mu$  decay have to be defined.  $p_T$  is one of them, because it can influence the trigger efficiency as well as the detection of the muons itself. If the  $p_T$  of the muons is to low (i.e.  $p_T < 3$  GeV), they will not reach the muon systems due to the large magnetic field and the energy loss in the calorimeters. Another important physical observable is the pseudo-rapidity  $\eta$ , since the coverage of the tracker and the muon systems are limited roughly to  $-2.5 < \eta < 2.5$ . CMS will not be able to detect muons outside of this area. In addition,  $\tau$  leptons produced in the decays of  $W$  or  $Z$  bosons have a non-neglectable boost. The muons coming from the  $\tau \rightarrow \mu\mu\mu$  decay are very close together. The distance measured as  $\Delta R$  is a crucial value to estimate the influence on the detection power. If the muons are too close together, the reconstruction of one or more muons will fail or at least gets imprecise, because the association between hits and tracks gets more complicated. Furthermore the closeness of the muons may affect the track matching between the tracker and the muon chambers, leading to wrong values of  $p_T$  or a higher  $\chi^2$  value of a combined fit. In particular the High Level Trigger is affected by wrong matching.

The distributions of the above mentioned observables are shown in figure 5.5 and 5.6, respectively. They confirm the result, which were obtained by applying detector specific cuts for each model. Different models affect the detection power of CMS only marginally. Hence no special matrix element is used for the further analysis.

On the other hand the only way to distinguish between the models is the angular distribution. Therefore, only the  $W$  source can be used and it will be necessary to distinguish between particles and anti-particles in order to determine the  $\tau$  polarization. The  $\tau$  leptons produced by other sources are not useful to distinguish between the models, because of the reduced  $\tau$  polarization is not that simple in this case. The  $\tau$  leptons from these sources only bias the signal. Considering only  $\tau$  leptons produced by electroweak gauge bosons, about 85% will be produced in  $W$  decays.  $\tau$  leptons originating in  $D$  and  $B$  decays can be neglected in that case, because they produce much softer

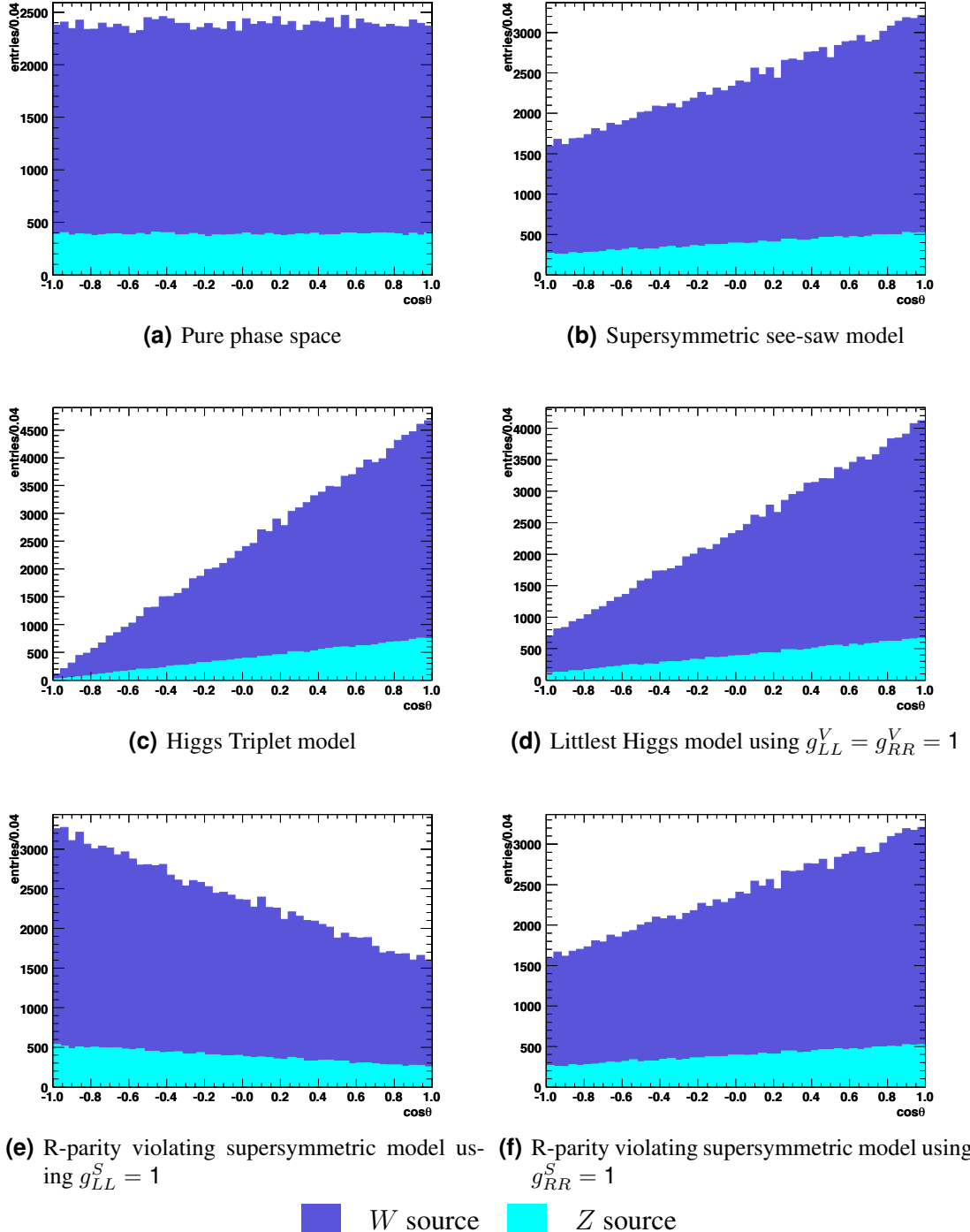


**Figure 5.3:** Resulting angular distributions for various considered models taking into account the cross-sections of the  $\tau$  production at the LHC.

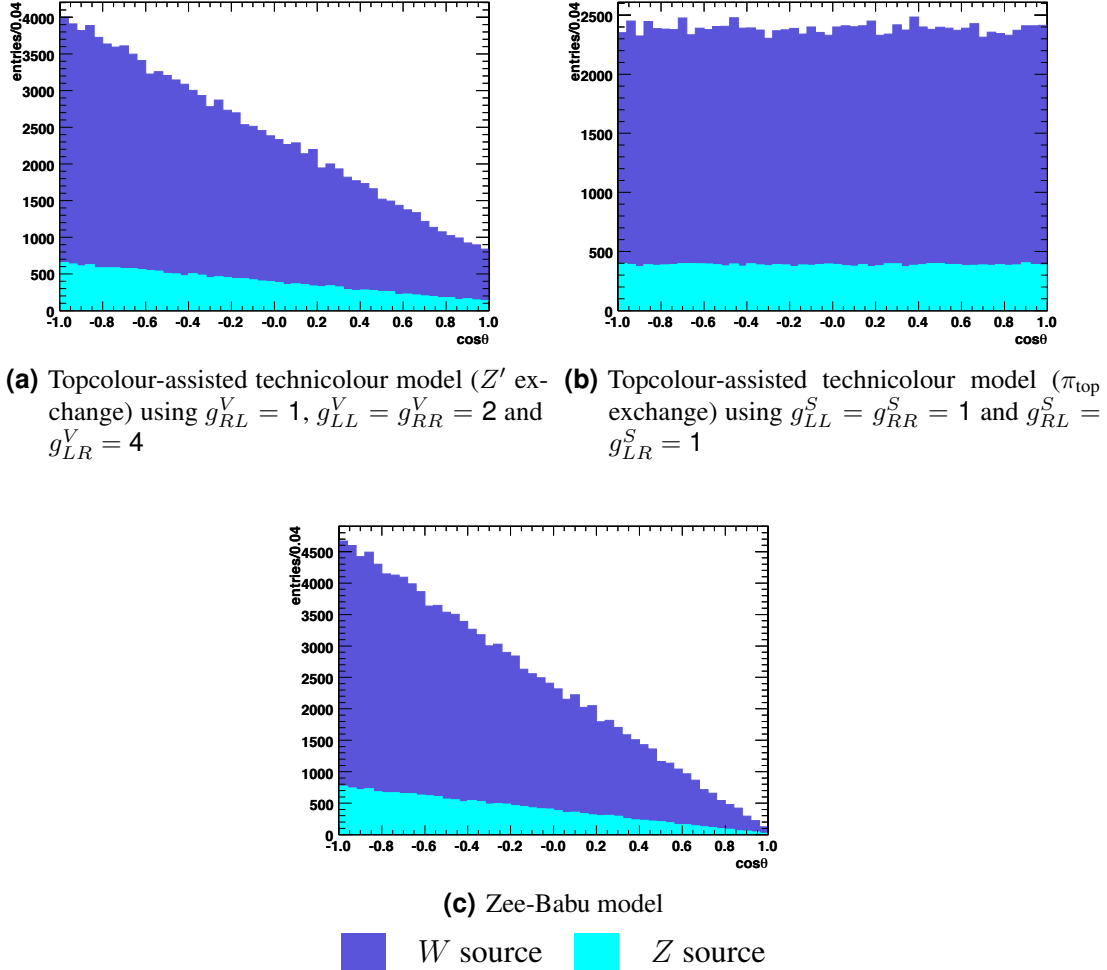


**Figure 5.4:** Resulting angular distributions for various considered models taking into account the cross-sections of the  $\tau$  production at the LHC.

muons, which are hard to trigger on and they will not pass the used background rejection cuts described in chapter 6. Nevertheless, the possibility to distinguish between the models exists in principle and a model determination might be possible according to the number of events measured. But depending on the branching ratio of  $\tau \rightarrow \mu\mu\mu$ , the LHC have to run at least few years on high luminosity to have a realistic chance to pin down a model.

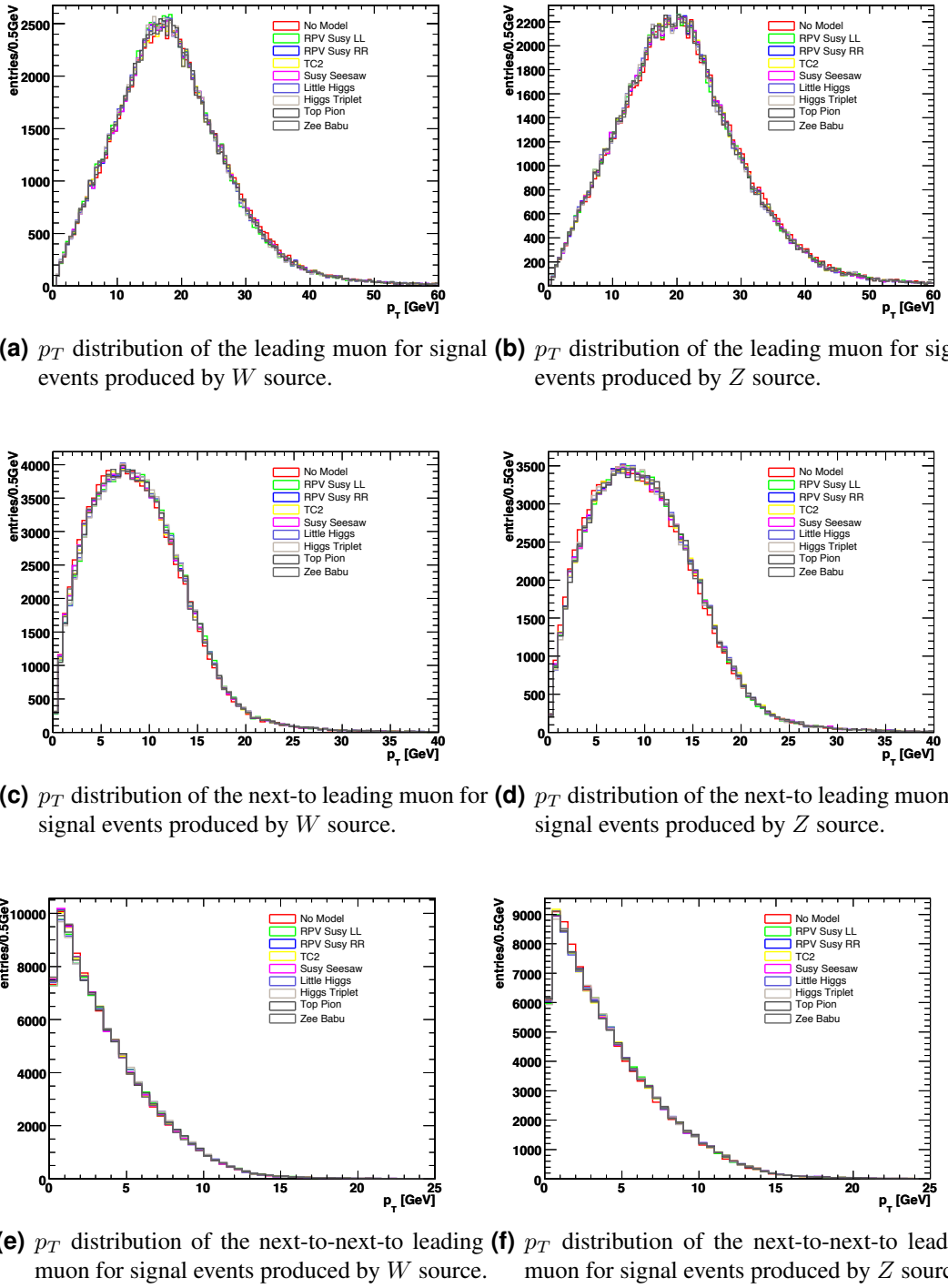
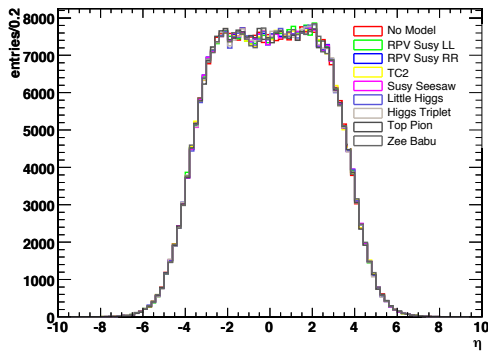
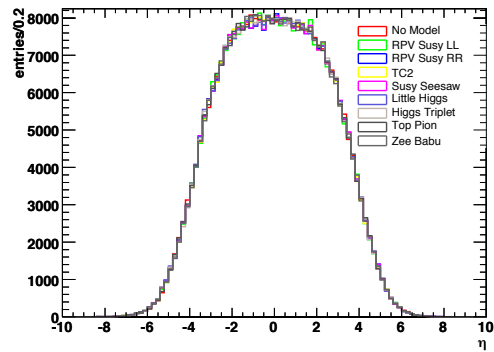


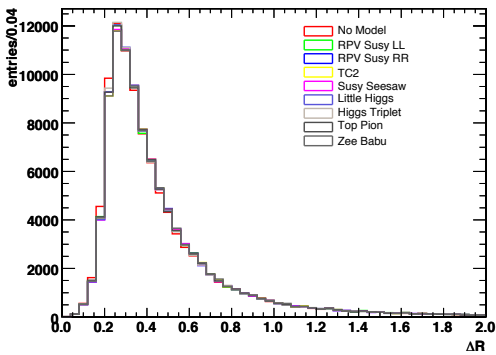
**Figure 5.5:** Influence of the different models to the transverse momenta of the three muons.



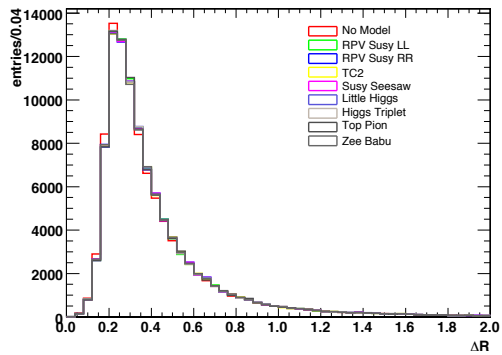
(a)  $\eta$  distribution for signal events produced by  $W$  source.



(b)  $\eta$  distribution for signal events produced by  $Z$  source.



(c)  $\Delta R$  distribution for signal events produced by  $W$  source.



(d)  $\Delta R$  distribution for signal events produced by  $Z$  source.

**Figure 5.6:** Influence of the different models to observables, which have been considered to evaluate the detection power.

# Chapter 6

## The Decay $\tau \rightarrow \mu\mu\mu$

### 6.1 The Production of $\tau$ Leptons at the LHC

The LHC offers already in the low luminosity phase an excellent possibility to study  $\tau$  leptons. The major  $\tau$  sources at the LHC are:

- the decay of the  $D_s$  meson:  $D_s \rightarrow \tau\nu_\tau$ ,
- the decay of  $B$  mesons: i.e  $B_0 \rightarrow \tau + X$ ,
- the decay of the  $W$  boson:  $W \rightarrow \tau\nu_\tau$ ,
- the decay of the  $Z$  boson:  $Z \rightarrow \tau^+\tau^-$ .

To estimate the cross-section, PYTHIA 6.325 with the parton distribution function CTEQ5L was used. Since the branching ratios of heavy meson decays in PYTHIA 6.325 are not up-to-date, the branching ratios of the implemented  $\tau$  decays have been updated from the PDG [18].

The total  $\tau$  lepton production cross-section at the LHC is  $\sigma(pp \rightarrow \tau + X) \approx 140 \mu\text{b}$ . Even in the low luminosity phase, with the conservative assumption that CMS will collect an integrated luminosity of  $10 \text{ fb}^{-1}$  per year, about  $10^{12}$   $\tau$  leptons will be produced within the CMS detector. The dominant production sources are the  $D_s$  and various  $B$  mesons decays (see table 6.1).

Meson (M)	$D_s$	$B_0$	$B^\pm$	$B_s^0$
$\sigma(M \rightarrow \tau + X) / \sigma(pp \rightarrow \tau + X)$	45%	22%	26%	7%
$N_\tau / 10 \text{ fb}^{-1}$	$6.3 \cdot 10^{11}$	$3.1 \cdot 10^{11}$	$3.6 \cdot 10^{11}$	$9.7 \cdot 10^{10}$

**Table 6.1:** Numbers of produced  $\tau$  leptons per year and the relative fraction of the  $\tau$  production via  $b$  and  $c$  mesons.

The cross-section for  $\tau$  production via the  $W$  boson  $\sigma(W \rightarrow \tau\nu_\tau)$  is  $15.4 \text{ nb}$  and therefore considerably lower. The  $\tau$  production cross section for the  $Z$  boson  $\sigma(Z \rightarrow \tau^+\tau^-)$  is  $1.47 \text{ nb}$ . The number of prompt  $\tau$  leptons produced and the relative cross sections can be found in table 6.2.

Despite the fact that the  $W$  and the  $Z$  production sources will provide considerably less  $\tau$  leptons per year, they are more energetic and due to trigger and detection issues the important sources for this study (see section 6.3).

Boson (B)	$W$	$Z$
$\sigma(B \rightarrow \tau + X) / \sigma(pp \rightarrow \tau + X)$	$1.1 \cdot 10^{-4}$	$1.1 \cdot 10^{-5}$
$N_\tau / 10 \text{ fb}^{-1}$	$1.5 \cdot 10^8$	$2.9 \cdot 10^7$

**Table 6.2:** Numbers of produced  $\tau$  leptons per year and the relative fraction of the  $\tau$  production via  $W$  and  $Z$  bosons.

Considering the current upper limit on the branching ratio  $\mathcal{B}_r < 3.2 \cdot 10^{-8}$  [18] of the lepton flavour violating neutrinoless  $\tau$  decay  $\tau \rightarrow \mu\mu\mu$ , the expected numbers of decays in CMS within one year of LHC running at low luminosity ( $\mathcal{L} = 10 \text{ fb}^{-1}/\text{year}$ ) are

$$N_{\text{expected}} = \mathcal{L} \times \mathcal{B}_r(\tau \rightarrow \mu\mu\mu) \times \sigma(X \rightarrow \tau + Y) \quad (6.1)$$

$\tau$ source	Expected number of $\tau \rightarrow \mu\mu\mu$ events
$W$ boson	$\approx 5$
$Z$ boson	$\approx 1$
$D_s$ meson	20160
$B$ mesons	24500

**Table 6.3:** Numbers of expected signal ( $\tau \rightarrow \mu\mu\mu$ ) events per year ( $10 \text{ fb}^{-1}$ ) using the current upper limit for the  $\tau \rightarrow \mu\mu\mu$  branching ratio.

## 6.2 Signal and Background Datasets

The general steps of Monte Carlo production have been described in section 3.2. Since the  $\tau \rightarrow \mu\mu\mu$  signal process is not implemented in PYTHIA, the implementation described in Chapter 5 is used. The impact of the considered models on the reconstruction of physical observables described in section 5.5 is only marginal, therefore no special model is considered for the signal process generation. For each chosen signal source, 50000 events were produced in a private production on the computing Grid. The production of signal events from  $Z$  decays was done separately for particles and antiparticles, so that the decay of one  $\tau$  was forced into three muons, whereas the other  $\tau$  decayed according to the default PYTHIA decay table.

The sources of background are coming from Standard Model decays which mimic the signal process. The main sources of muons are decays of  $D$  and  $B$  mesons which are copiously produced at LHC energies. Additional sources are in-flights decays and punch throughs of pions passing the calorimeters without being stopped. The probability to misidentify an event from pile up is small and cosmic rays can be rejected by timing. Due to the high momentum of the muons from direct  $W$  and  $Z$  decays, their contribution to the background is negligible [76–79].

Heavy quarks are produced at the LHC by gluon-gluon-fusion and quark-antiquark annihilation (see figure 6.1 for the leading order processes). The next-to-leading order processes of gluon splitting and flavour excitation give an additional contribution to the heavy flavour production (see figure 6.2). These processes are important for the heavy

flavour production at the center-of-mass energy of LHC. For example, only 10%-20% of the  $b$  production at LHC is originated by the leading order processes. The ratio is even smaller for the charm production (see figure 6.3) [50, 80]. The heavy flavour production using the PYTHIA parameter  $MSEL=4-8$  does only include the leading order processes, therefore it is necessary to produce minimum bias events using the PYTHIA parameter  $MSEL=1$  and select only events containing  $b\bar{b}$  or  $c\bar{c}$ . A simple scaling of the cross section is not enough, since the next-to-leading processes produce more collimated quark-antiquark pairs, which are important contributions to the background.

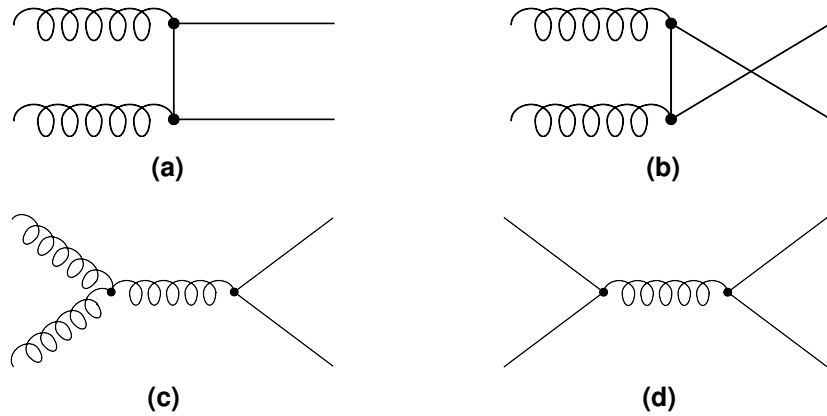


**Figure 6.1:** *Leading order contribution to the heavy quark production via gluon-gluon-fusion (a-c) and quark-antiquark-annihilation (d).*

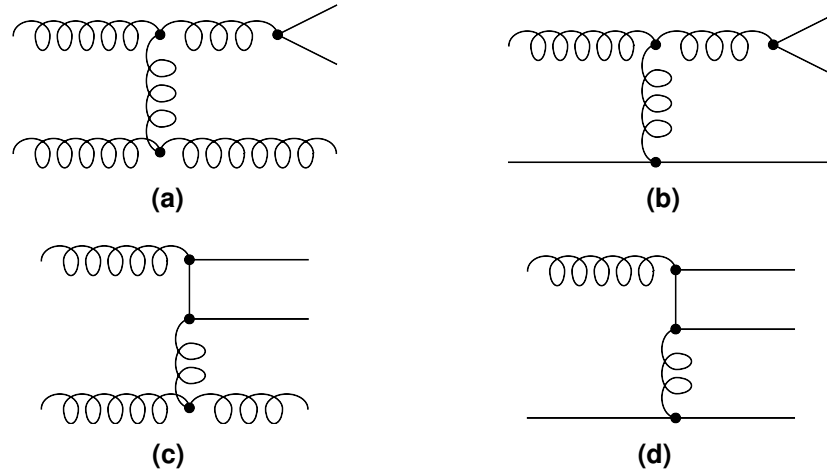


**Figure 6.2:** *Next-to-leading order contribution to the heavy quark production via gluon splitting (a,b) and flavour excitation (c,d).*

For the study of backgrounds two datasets, produced by the CMS offline group are available. A  $b\bar{b} \rightarrow \mu\mu$  sample containing around 3 million events and a  $c\bar{c} \rightarrow \mu\mu$  sample containing roughly 1 million events. To save computing power, a muon pair filter is applied during the production, requiring two muons within the detector acceptance ( $-2.5 < \eta < 2.5$ ) having a  $p_T > 2.5$  GeV. Additionally, the semi-leptonic muon decays of the  $B/D$  hadrons are forced during the production process. That has to be taken into account for the calculation of the “visible” cross section, since PYTHIA does not

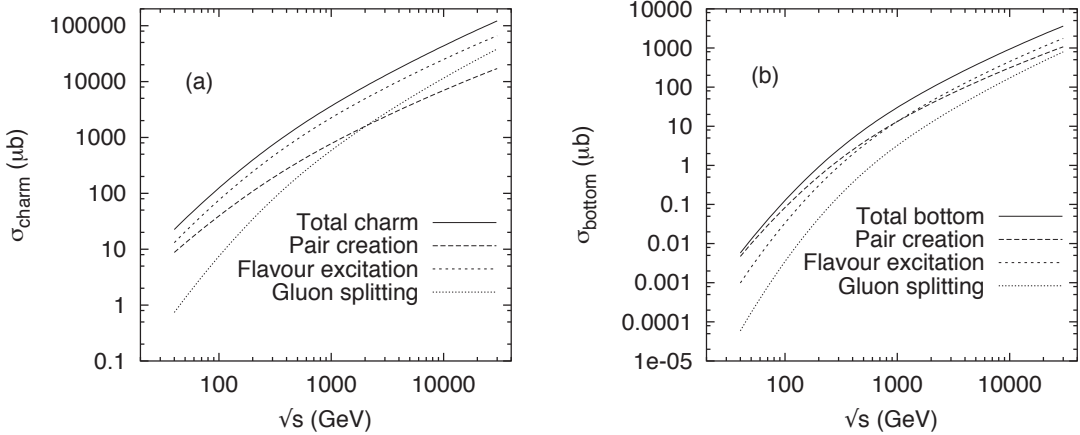


**Figure 6.3:** Contribution of the different processes to the total cross section of charm (a) and bottom (b) production at  $pp$  collider as function of the center-of-mass energy [80].

consider it for the calculation of the production cross section of minimum bias events. That means, beside the filter efficiency  $\epsilon_{\text{prod}}$  for  $b\bar{b}$  or  $c\bar{c}$  filter, the branching ratio of the semi-leptonic muon decays has to be considered for both, quark and antiquark. The branching ratio of semi-leptonic muon  $B/D$  decays was estimated to  $\mathcal{B}_r \approx 10\%$ . The “visible” cross section can be calculated using equation 6.2

$$\sigma_{\text{vis}} = \sigma_{\text{prod}} \times \epsilon_{\text{prod}} \times \mathcal{B}_{r_1} \times \mathcal{B}_{r_2}. \quad (6.2)$$

The equivalent luminosity of the generated events can be obtained using equation 6.3

$$\begin{aligned} \mathcal{L}_{\text{gen}} &= \frac{N_{\text{gen}}}{\sigma_{\text{vis}}} \\ &= \frac{N_{\text{gen}}}{\sigma_{\text{prod}} \times \epsilon_{\text{prod}} \times \mathcal{B}_{r_1} \times \mathcal{B}_{r_2}}. \end{aligned} \quad (6.3)$$

An overview over the datasets used for the analysis is shown in table 6.4. Although a large number of events are available for the  $c\bar{c}$  and  $b\bar{b}$  backgrounds, the corresponding luminosity of the generated events is still low, which results in high factors for a scaling to  $10 \text{ fb}^{-1}$ , due to their high production cross section. Additionally, one has to take into account that not all rare decays are implemented in PYTHIA. One example for a rare decay that can mimic the signal is  $D_s \rightarrow \phi \mu \nu_\mu$  followed by a decay  $\phi \rightarrow \mu\mu$ . This background can be reduced by an invariant mass cut around the  $\phi$  mass. The unimplemented radiative decay  $\phi \rightarrow \mu\mu\gamma$  survives this cut since the photon remains undetected. Although the branching ratio is only  $10^{-5}$ , this could be an irreducible background. Further examples are decays with  $\eta$  or  $\eta'$  instead of the  $\phi$  in the above decay chain. For the analysis of real data from the CMS detector, a background determination based only on simulated events, is not the optimal solution. The preferable way is the determination of background contributions from the data itself using e.g. methods exploring sidebands.

Dataset	$W$ source	$Z$ source	$bb \rightarrow 2\mu$	$c\bar{c} \rightarrow 2\mu$
$\sigma_{\text{prod}}[\text{b}]$	$1.54 \cdot 10^{-8}$	$1.467 \cdot 10^{-9}$	$5.47 \cdot 10^{-2}$	$5.47 \cdot 10^{-2}$
$\epsilon_{\text{prod}}$	1	1	$5.9 \cdot 10^{-4}$	$1.69 \cdot 10^{-4}$
$\mathcal{B}_{r_1}$	$3.2 \cdot 10^{-8}$	$3.2 \cdot 10^{-8}$	0.1	0.1
$\mathcal{B}_{r_2}$	-	-	0.1	0.1
$N_{\text{gen}}$	50000	50000	2794900	983424
$\sigma_{\text{vis}}[\text{b}]$	$4.928 \cdot 10^{-16}$	$9.389 \cdot 10^{-17}$	$3.227 \cdot 10^{-7}$	$9.244 \cdot 10^{-8}$
$\mathcal{L}_{\text{gen}}[\text{fb}^{-1}]$	$1.015 \cdot 10^5$	$5.325 \cdot 10^5$	$8.66 \cdot 10^{-3}$	$1.064 \cdot 10^{-2}$
#/ $10 \text{ fb}^{-1}$	4.928	0.939	$3.227 \cdot 10^9$	$9.244 \cdot 10^8$
Scaling $10 \text{ fb}^{-1}$	$9.856 \cdot 10^{-5}$	$1.878 \cdot 10^{-5}$	1154.71	940.012

**Table 6.4:** Generated datasets (fully reconstructed) and the corresponding number of generated events, cross sections, luminosities and scaling factors.

The background datasets were produced during the CSA07<sup>1</sup>. For the reconstruction and the simulation of the High Level Trigger, the early physics conditions for the first  $100 \text{ pb}^{-1}$  including misalignment, miscalibration and trigger tables are used. Improved limits on the decay  $\tau \rightarrow \mu\mu\mu$  are not expected during the first year of data taking, therefore the background datasets used have to be re-reconstructed using a more suitable misalignment and miscalibration scenario. Since a misalignment and miscalibration scenario for the beginning of the low luminosity phase is not yet available, the perfect alignment is used for the re-reconstruction. Also the HLT simulation has to be redone using the preliminary muon trigger table for the low luminosity phase ( $\mathcal{L} = 2 \times 10^{33} \text{ cm}^{-2} \text{ s}^{-1}$ ) before using the datasets for the analysis.

## 6.3 Study on Generator Level

The first part of the analysis is done at generator level. As already described in section 3.2, the full information of the physics process, as it could be observed by an ideal detector, is available at that stage. Important physical observables can be analysed in an easy way and their impact on the later selection and reconstruction of signal events in the real detector environment can be determined. With this approach the  $\tau$  lepton source most appropriate can be chosen for the further analysis.

### The Transverse Momentum of the Muons

One of the observables is the distribution of the transverse momentum of the three muons coming from the lepton flavour violating  $\tau \rightarrow \mu\mu\mu$  decay. The transverse momentum of the leading and next-to-leading muon is an important quantity for the trigger. As described in section 4.5, five High Level Trigger paths are currently foreseen for the low luminosity phase. The most consolidated trigger paths having the lowest thresholds are the HLT single isolated (19 GeV) path and the HLT dimuon isolated (7 GeV) path. The HLT multimuon path has been introduced recently and its availability in the low luminosity phase is not ensured. Therefore, the former ones are used to

<sup>1</sup>The Computing, Software and Analysis Challenge 2007 was a test run of the interplay of computing, software and analysis to be prepared for data taking.

estimate the impact for the different sources. In figure 6.4 the transverse momentum of the leading and next-to-leading muon and the corresponding trigger thresholds are depicted.

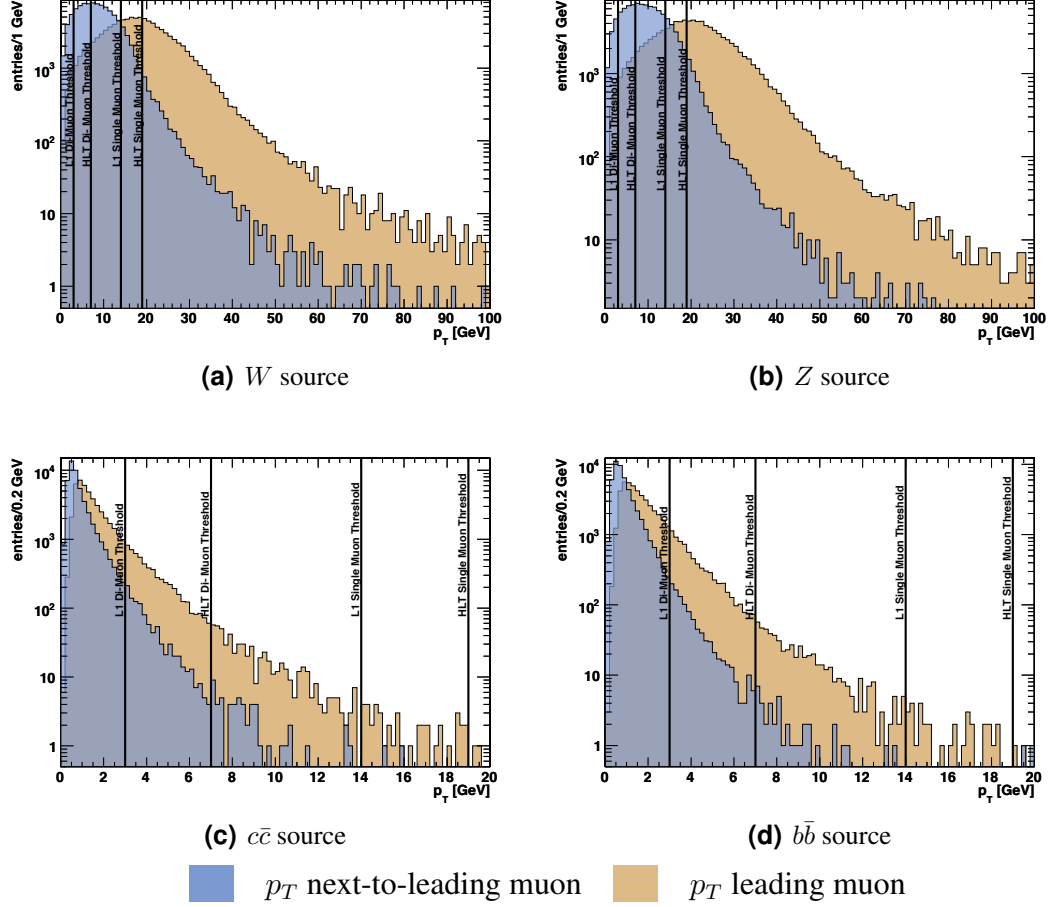


**Figure 6.4:** Transverse momentum ( $p_T$ ) of the leading and next-to-leading muon with the corresponding CMS muon trigger thresholds for the low luminosity phase.

$\tau$ source	$W$	$Z$	$D_s$	$B$ mesons
$\epsilon_{\text{single}\mu}$	45%	56%	0.02%	0.02%
$\epsilon_{\text{di-}\mu}$	60%	66%	0.11%	0.09%
$\epsilon_{\text{trigger}}$	74%	80%	0.13%	0.09%

**Table 6.5:** Trigger efficiencies obtained by applying the CMS trigger thresholds to the Monte Carlo muons separated into single muon and di-muon trigger as well as the total trigger efficiency.

Obviously the transverse momentum depends on the source of the  $\tau$  leptons.  $\tau$  leptons produced by the  $W$  and  $Z$  bosons are more energetic, than  $\tau$  leptons coming from a meson decay. The advantage of the copious  $\tau$  lepton production via meson decays has to be put into a new perspective, due to low transverse momentum of the muons. Muons from these sources will hardly be triggered. The obtained trigger efficiencies

for each source by applying the CMS trigger thresholds to the Monte Carlo muons are shown in table 6.5.

Also the transverse momentum of the next-to-next-to-leading muon is an important observable. Muons below a threshold of 3 GeV will hardly be reconstructed in CMS, due to the strong magnetic field and the huge amount of material before the first station of the muon detector. The distributions of the transverse momentum of the next-to-next-to-leading muon for the different  $\tau$  sources are depicted in figure 6.5.

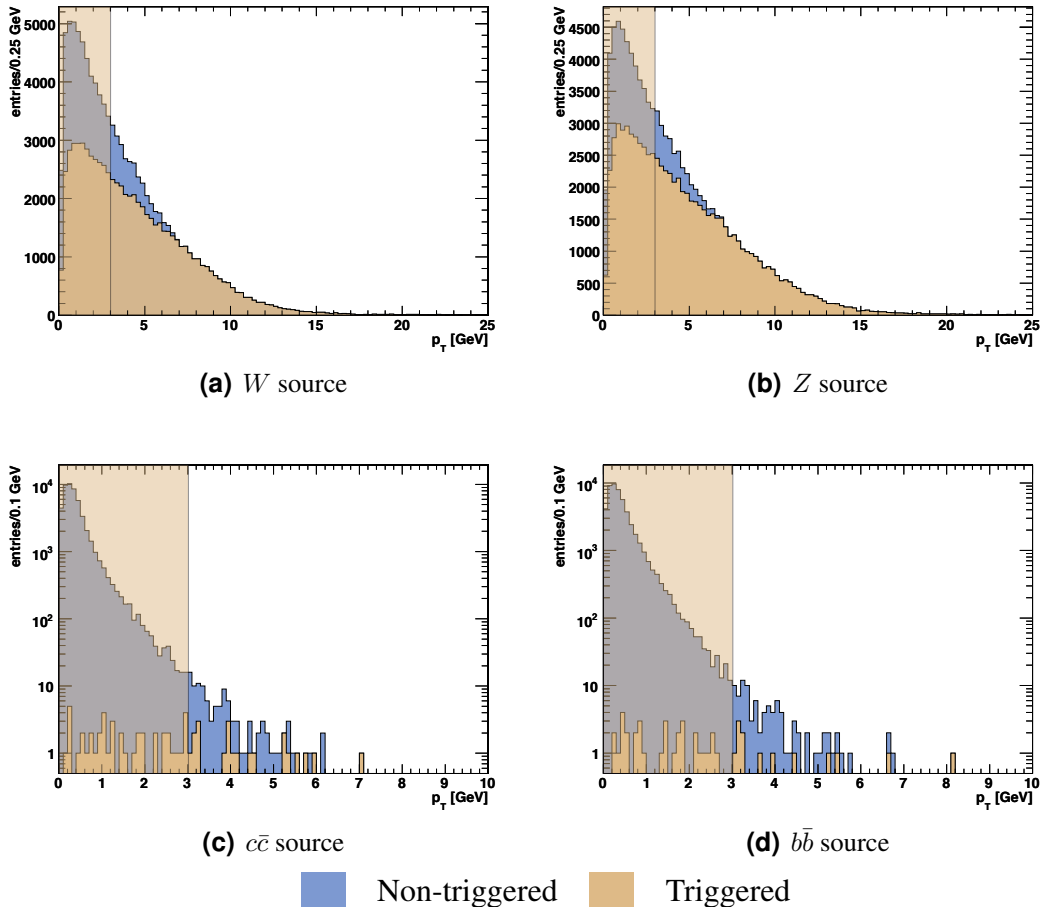


**Figure 6.5:** Transverse momentum ( $p_T$ ) of the next-to-next-to leading muon. The highlighted region marks the part of the muons, which will probably not reach the muon systems. Therefore, they will be most probable not reconstructed as global muons.

An estimate of the reconstruction efficiencies of the next-to-next-to leading muon by applying the 3 GeV reconstruction threshold to the corresponding Monte Carlo muon are shown in table 6.6.

$\tau$ source	$W$	$Z$	$D_s$	$B$ mesons
$\epsilon_{\text{reco3rd}\mu}$	50%	54%	0.2%	0.2%

**Table 6.6:** Estimated reconstruction efficiencies for the next-to-next-to leading muon obtained by applying the 3 GeV reconstruction threshold to the corresponding Monte Carlo muon.

The estimated reconstruction efficiency for the next-to-next-to leading muons of events produced via the  $W$  and  $Z$  bosons is high, whereas the reconstruction of events coming from  $\tau$  leptons produced by the  $B$  or  $D_s$  mesons is hardly possible.

### The Distribution in Pseudo-rapidity

Another important observable is the pseudo-rapidity  $\eta$ , since the coverage of the tracker and the muon system of the CMS detector is limited roughly to a pseudo rapidity in the range of  $-2.5 \leq \eta \leq 2.5$ . Particles outside of this range cannot be detected with the CMS detector. The distribution of the pseudo-rapidity for the different sources is depicted in figure 6.6.

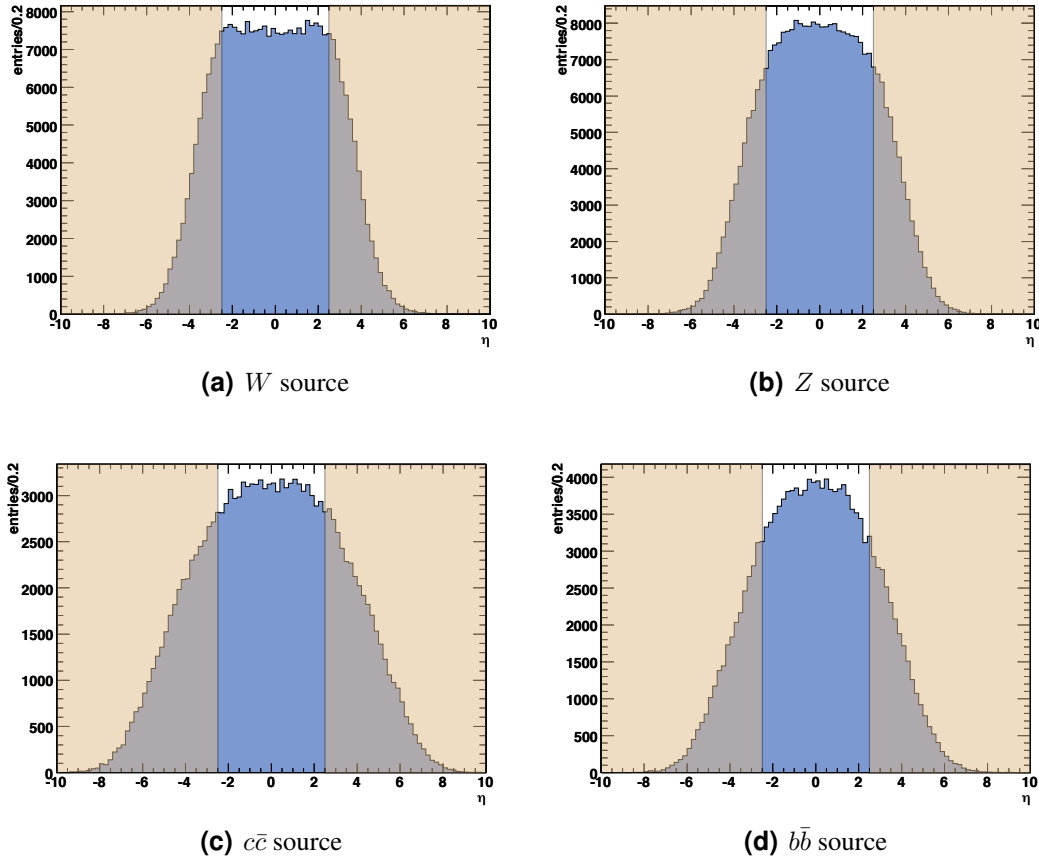


**Figure 6.6:** Pseudo-rapidity ( $\eta$ ) distribution of the muons. The highlighted region marks the muons outside of the sensitive detector volume.

The fraction of events inside of the sensitive detector volume for different  $\tau$  sources is shown in table 6.7.

$\tau$ source	$W$	$Z$	$D_s$	$B$ mesons
$\epsilon_\eta$	61%	63%	40%	50%

**Table 6.7:** Fraction of events inside of the sensitive detector volume.

Events originated by  $D_s$  or  $B$  mesons have a broader pseudo-rapidity distribution than

events coming from  $W$  and  $Z$  bosons. Therefore, the fraction of events inside of the sensitive detector volume is smaller for the  $\tau$  leptons produced by  $D_s$  and  $B$  mesons.

## Minimal and Maximal Distance Between the Muons

Due to the high  $p_T$  of  $\tau$  leptons originating from the  $W$  and  $Z$  sources, there is an additional important physical observable: the spatial distance of the muons. The problem with muons which are close together in space was already described in section 4.4. The problem in this case is the matching between the reconstructed track segment in the muon system and the reconstructed track in the silicon tracker. A missing or wrong match affects the reconstruction efficiency of muons. The distribution for the minimum and the maximum distance between two muons in an event is depicted in figure 6.7 (maximum) and figure 6.8 (minimum).

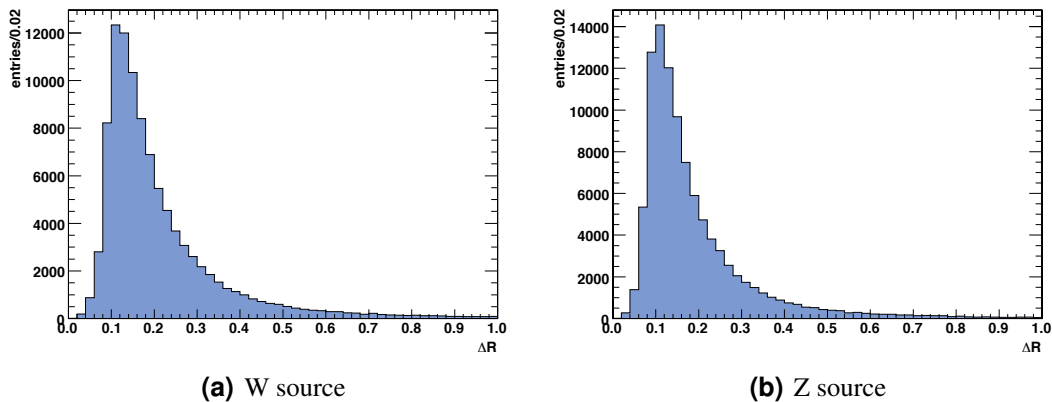


**Figure 6.7:** Distribution of the maximum distance between two muons in an event measured in  $\Delta R$ .

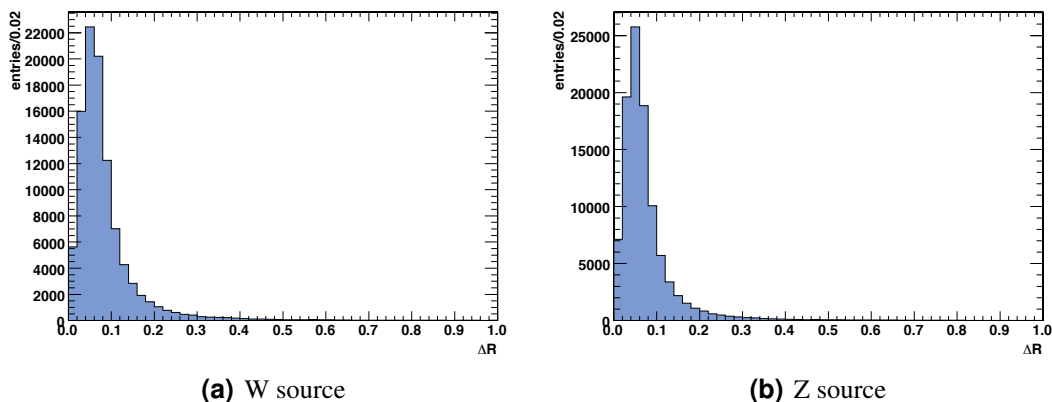


**Figure 6.8:** Distribution of the minimum distance between two muons in an event measured in  $\Delta R$ .

The failing of the reconstruction can not be fixed to a threshold on the distance of the muons, because it depends on the particular case. Therefore, no appropriate cut can be defined to estimate the effects on Monte Carlo level.

## Conclusion

To estimate the number of reconstructable events according to the physical bounds of the CMS detector, the following observables and cuts are used.

- Trigger 1 $\mu$ :  $p_T > 19 \text{ GeV}$  or
- Trigger 2 $\mu$ :  $p_T > 7 \text{ GeV}$ ,
- Detector acceptance for muons:  $-2.5 < \eta < 2.5$ ,
- All muons  $p_T > 3 \text{ GeV}$ .

The efficiency obtained by applying all of the above cuts on the Monte Carlo level is shown in table 6.8.

$\tau$ source	$W$	$Z$	$D_s$	$B$ mesons
$\epsilon_{\text{CMS}}$	27%	32%	0.03%	0.02%

**Table 6.8:** *Estimation of an upper limit on the number of events reconstructible with the CMS detector by applying the above mentioned cuts on the Monte Carlo level.*

The  $\tau$  leptons originated from the  $W$  bosons are best suited for the further analysis. Those events can be fairly well triggered and reconstructed. They have an easy, but also problematic signature in terms of reconstruction and trigger, of three highly collimated muons. Concerning that some improvements are possible by requiring only two reconstructed global muons and a third track nearby in the silicon tracker. The  $\tau$  leptons produced by  $Z$  bosons are also good candidates for the further analysis, with respect to trigger and reconstruction purposes. But about one magnitude less  $\tau$  leptons per year are produced by them. The majority of  $\tau$  leptons at CMS are coming from decays of the  $D_s$  and  $B$  mesons. Unfortunately, those events are hardly triggered and reconstructed, due to the low transverse momentum of the muons. Additionally, their signature does not allow an improvement by requiring only two reconstructed global muons and a third track nearby in the silicon tracker, since those muons are not close enough, due to the low boost of the  $\tau$  leptons.

Beside the impact on the trigger and reconstruction efficiencies, some hints for a background reduction can be obtained from this Monte Carlo study. As shown in figure 6.7 and 6.8, the distance between two muons is very small, due to the highly boosted  $\tau$ . Background processes coming from  $b\bar{b}$  and  $c\bar{c}$  production are not expected to be highly boosted, therefore the distance between the muons in space should be larger.

## 6.4 Monte Carlo Truth Matching

To associate the reconstructed muons with the corresponding muons on generator level it is necessary to match them, since a direct access is not possible. The matching is necessary to study the kinematics of the signal muons after the reconstruction in the detector to determine cuts to separate signal and background. In addition, it is needed to calculate the purity of the event selection.

The association is done by a global matching, that means the sum of  $\Delta R$  for all possible permutations of reconstructed and generator muons is calculated and the best permutation is chosen by

$$\min \left( \sum_{i=1}^N \Delta R_n \right). \quad (6.4)$$

Afterwards the quality of the best permutation is determined by using the following criteria.

- Matching by momentum:  $|p_{T_{gen}} - p_{T_{rec}}| < 0.2 \cdot p_{T_{rec}}$ ,
- Matching by charge:  $q_{rec} = q_{gen}$ ,
- Matching by  $\Delta R < 0.01$ .

All criteria have to be fulfilled to accept the best permutation as a successful matching.

## 6.5 Selection of $\tau \rightarrow \mu\mu\mu$ Signal Events

For the analysis of reconstructed events, only the output of the CMS detector can be used. In contrast to an analysis on generator level, no information about the underlying physics process is available. In order to select signal like processes a pattern recognition has to be done. The signal selection is mainly divided into two parts, the preselection to reduce the amount of data for the following event selection. The background samples are skimmed additionally during the process of re-reconstruction and redoing the HLT, described in section 6.2, to archive a data reduction already before the preselection step.

Due to the reconstruction issues described in section 4.4, which are associated with the fact that the muons from the decay of the  $\tau$  leptons originated by  $W$  and  $Z$  bosons are highly collimated, only two reconstructed global muons plus a third track in their neighbourhood are required. This improves the reconstruction efficiency of the  $\tau \rightarrow \mu\mu\mu$  decay by roughly a factor of two. Three examples for the considered cases are depicted in the following. The case were all three muons are reconstructed correctly is shown in figure 6.9.

An event having only two global muons reconstructed is depicted in figure 6.10. A zoomed view of the tracker is showing the two tracks matched to the global muons and a third track, which is to soft to be reconstructed in the muon chambers.

In the event depicted in figure 6.11 two global muons and one standalone muon are reconstructed. From the zoomed view of the tracker it is clearly evident that two tracks are really collimated, so probably one of the standalone muons is matched to a wrong track, therefore the matching of the remaining standalone muon fails.

### 6.5.1 Skimming of Background Samples

For the background samples it is reasonable to reduce the amount of data already at the stage of re-reconstruction and redoing the HLT, since the overhead is very small. The total size of the background sample used in this analysis is about 7 TB. After

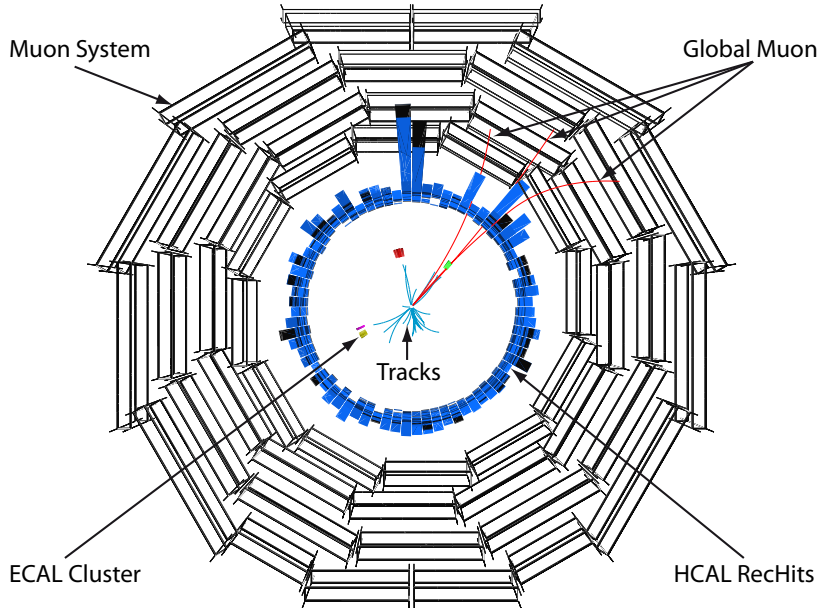


**Figure 6.9:** A  $\tau \rightarrow \mu\mu\mu$  event with three reconstructed global muons in the  $r - \phi$  view of the detector.

the process of skimming, the total amount of data left for the preselection step is only about 0.8 GB. The amount of data is reduced by roughly a factor of nine, so that the preselection is accelerated enormously.

The requirements used for the step of skimming are very loose to ensure to have a sufficient amount of events for the further steps.

- Invariant mass  $|m_\tau - m_{\mu\mu\mu}| < 5 \text{ GeV}$ ,
- Total charge  $\left| \sum_{i=1}^3 q_i \right| = 1$ .

To pass the process of skimming it is required that at least two global muons are reconstructed. In the case of more than three reconstructed global muons, all possible combinations are checked concerning their invariant mass and their total charge. If exactly three global muons are reconstructed, their invariant mass and their total charge is checked and if one of the criteria is not fulfilled, the muon furthest away from the others is removed from the collection and the following procedure for the two global muon plus a third adjacent track is applied.

In the case of two reconstructed global muons, all combination of those muons with any adjacent track is evaluated concerning their invariant mass and their total charge. A flowchart of the skimming procedure is depicted in figure 6.12.

The output format of the skimming process is a CMS EDM<sup>2</sup> root file, which still contains the full information of the accepted events.

---

<sup>2</sup>Event Data Model

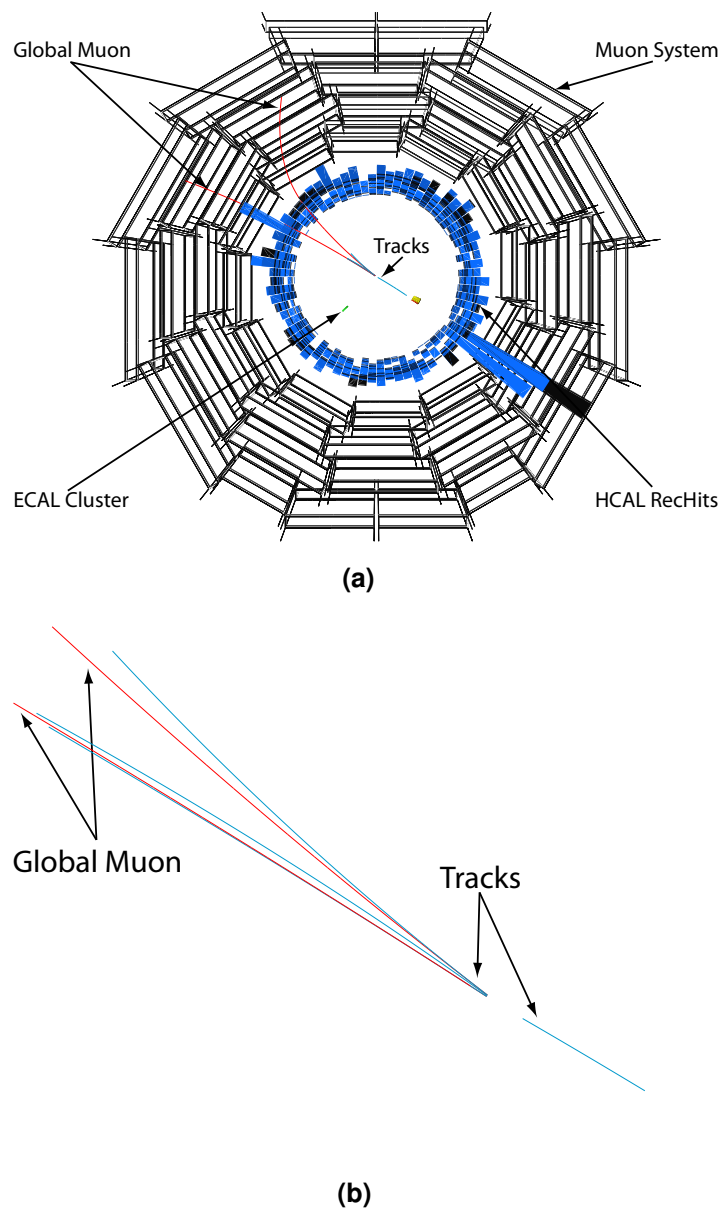


**Figure 6.10:** A  $\tau \rightarrow \mu\mu\mu$  event with two reconstructed global muons in the  $r - \phi$  view of the detector (a) and a zoomed view of the tracker (b).

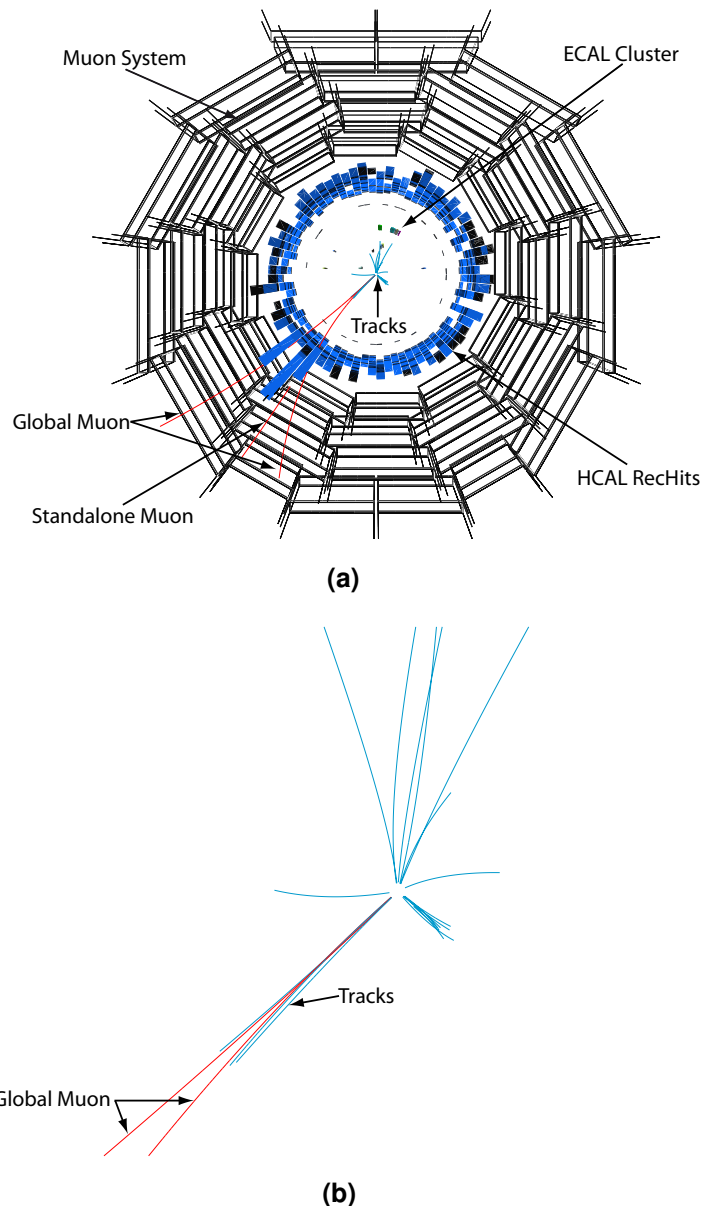


**Figure 6.11:** A  $\tau \rightarrow \mu\mu\mu$  event with two reconstructed global muons and one additional reconstructed standalone muon in the  $r - \phi$  view of the detector (a) and a zoomed view of the tracker (b).

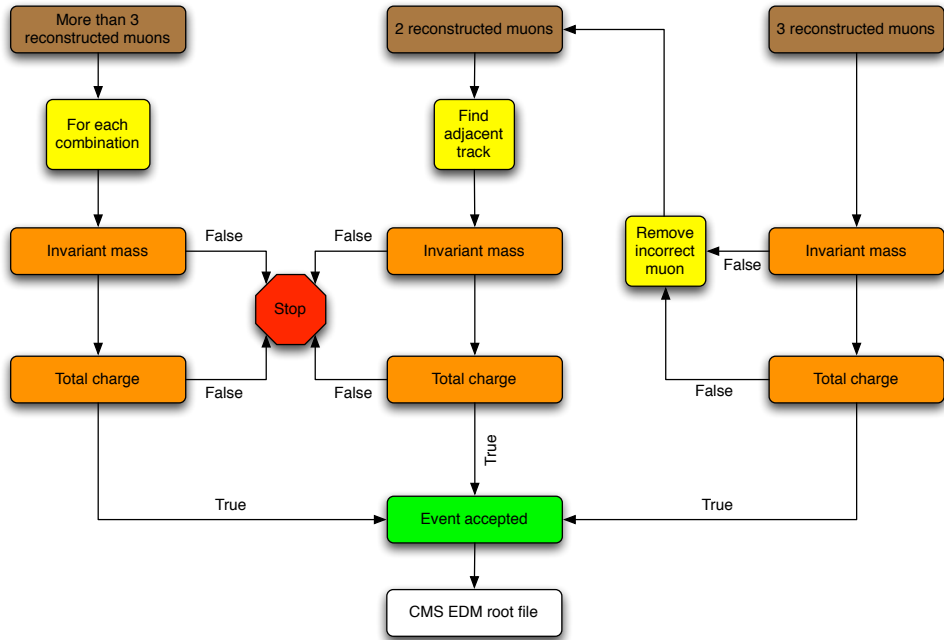


**Figure 6.12:** Flowchart of the skimming procedure.

### 6.5.2 Preselection

The next step in the event selection is the process of preselection. In the first step of the preselection the trigger decision of the HLT is evaluated. The adjoining step of event preselection is similar to the corresponding step in the skimming process. The only difference is that the cuts are tighter.

- Invariant mass  $|m_\tau - m_{\mu\mu\mu}| < 200 \text{ MeV}$ ,
- Total charge  $\left| \sum_{i=1}^3 q_i \right| = 1$ .

The step of preselection is used for both signal and background samples. Beside the reduction of the amount of data using an event filter, only the important event content for the further analysis is written to a private dataformat. This further reduces the amount of data. Also later used physical observables like secondary vertices, muon ID and isolation are calculated in the preselection step and stored in the private dataformat. A flowchart of the preselection procedure is depicted in figure 6.13.

### 6.5.3 Event Selection and Background Rejection

#### Isolation of the $\tau \rightarrow \mu\mu\mu$ Decay

Using the  $W$  and  $Z$  bosons as source of  $\tau$  leptons, the three muons coming from the  $\tau \rightarrow \mu\mu\mu$  decay are strongly collimated. The three muons are most likely isolated, due to the clean signature of those events. For the background processes  $c\bar{c} \rightarrow 2\mu$  and  $b\bar{b} \rightarrow 2\mu$  it is more likely, that the muons are surrounded by additional tracks coming from jets. For the isolation criteria a cone of 0.3 in  $\Delta R$  is used and no additional tracks

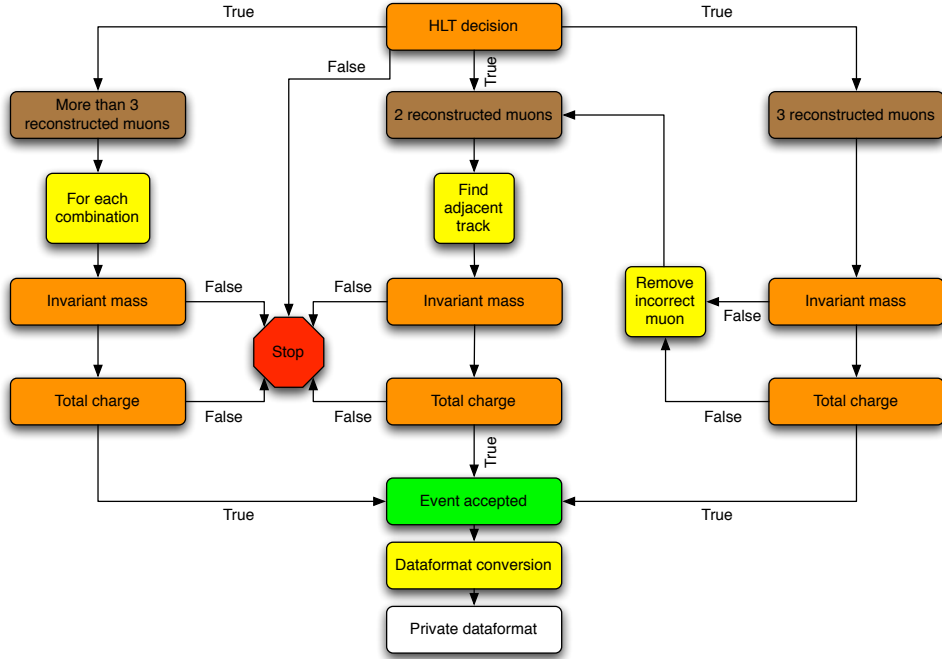


**Figure 6.13:** Flowchart of the preselection procedure.

having a  $p_T > 1 \text{ GeV}$  are accepted for the event selection. The number of tracks inside the isolation cone are depicted in figure 6.14(b) before applying additional cuts for the event selection. The  $N-1$  representation, which means that all other cuts are already applied before the considered one, is shown in figure 6.14(a).

Obviously most of the signal events are surviving the isolation criteria and on the other hand the background rejection power is substantial.

### Result from the Likelihood Based Muon ID

At least two reconstructed global muons are required for the event selection to increase the signal efficiency significantly. On the other hand the number of background events passing the event selection is also increased by that strategy. In section 4.4 an alternative muon identification for the additional tracks has been described using a likelihood ratio to obtain the muon likeness of that track. The input variables of this likelihood ratio are the energy deposition in the ECAL, HCAL and HO, and the number of reconstructed muon segments in the muon system. All events having a third track with  $p_\mu < 0.6$  are rejected. The cut value has been optimized by maximizing the product of efficiency and purity.

In figure 6.15 only events are considered, which have a  $2\mu + \text{track}$  signature, since this cut is not reasonable for all other events. In figure 6.15(a) the muon likeness of the third track is depicted before applying additional cuts, whereas in figure 6.15(b) the  $N-1$  representation is shown.

The alternative muon identification has a large background rejection power, but also a major part of the additional gained signal events are denied. But nevertheless, there is still an advantage for the signal selection efficiency by using the  $2\mu + \text{track}$  strategy.

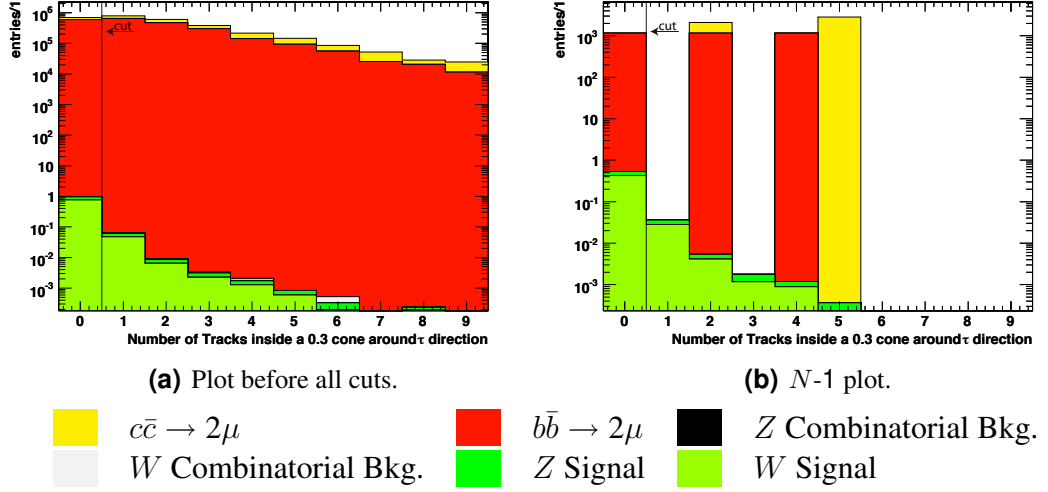


**Figure 6.14:** Number of additional tracks in a  $\Delta R = 0.3$  isolation cone around the  $\tau$  flight direction.

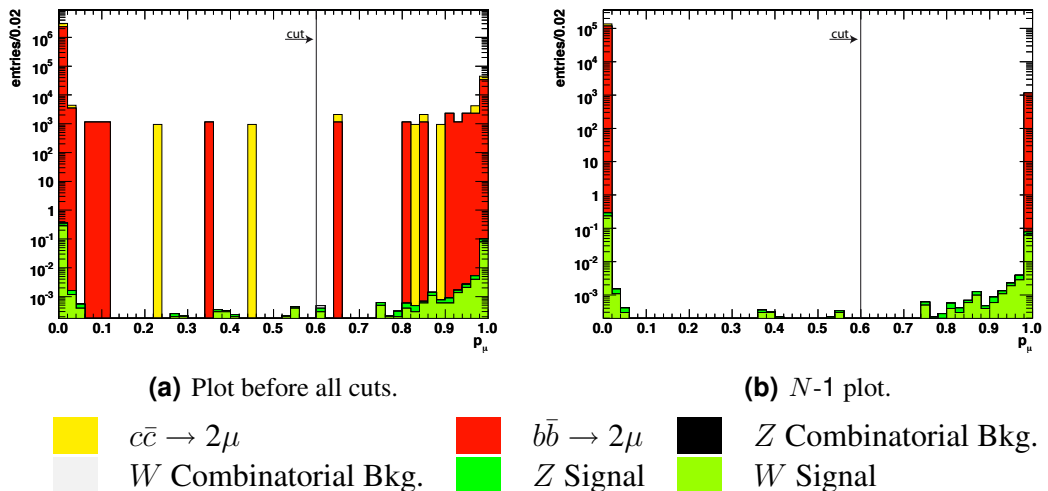


**Figure 6.15:** Distribution of the likelihood ratio for the implemented alternative muon identification described in section 4.4. Only events fulfilling the  $2\mu +$  track criteria are depicted in the figures above.

### Number of Tracks Compatible with the Secondary Vertex Fit

The  $\tau$  lepton travels a short distance through the detector before it decays, due to its lifetime of  $2.9 \cdot 10^{-13}$  s. The primary vertex of the event and the  $\tau$  decay vertex should be separable. The adaptive vertex described in section 4.2 is used to find the secondary vertex of the  $\tau \rightarrow \mu\mu\mu$  decay. For signal events it is expected to reconstruct a secondary vertex which consists of three tracks. The adaptive vertex fitter is able to down-weight outlying tracks with a weight  $w_i$ . All tracks having a weight of  $w_i < 0.5$  are treated as outlying tracks, that are not compatible with the reconstructed vertex. The number of tracks compatible with the vertex fit for signal and backgrounds is depicted in figure 6.16(a) before applying additional cuts and figure 6.16(b) is showing the  $N-1$  representation.

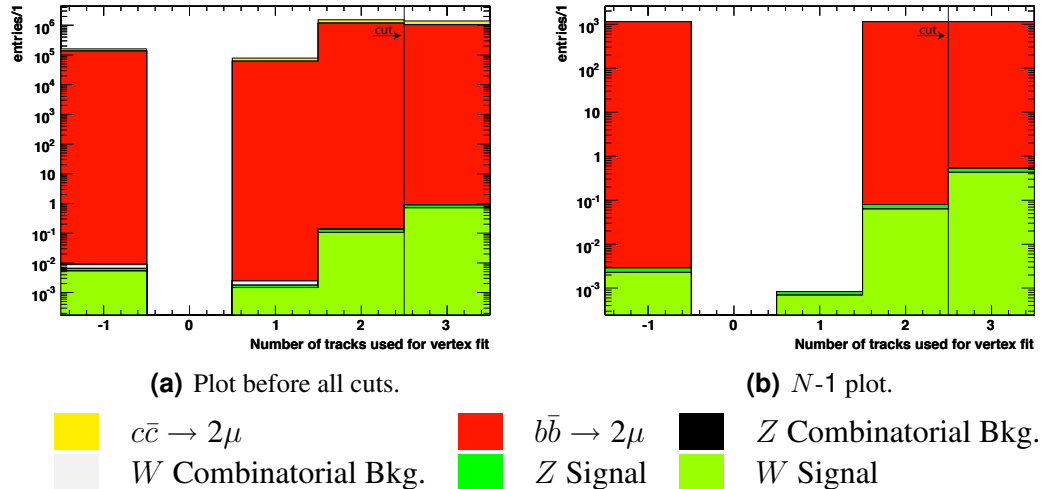


**Figure 6.16:** Number of tracks having a track weight of  $w_i > 0.5$  in the adaptive vertex fit. The entries in the first bin ( $-1$ ) are events where the adaptive vertex fit failed for various reasons.

All events having less than three tracks are rejected by this cut. The background rejection power of this cut is good without loosing too much of the signal events. The required cut value of three tracks compatible with the reconstructed vertex is natural and therefore no optimization based on efficiency and purity is applied.

### Reconstructed $\tau$ Mass

The invariant mass of the three muons coming from the  $\tau \rightarrow \mu\mu\mu$  decay is very close to the  $\tau$  mass. The  $\tau$  mass resolution of CMS for  $\tau \rightarrow \mu\mu\mu$  events originated by the  $W$  source is depicted in figure 6.17. The mass resolution obtained by a gaussian fit to the distribution is about 17 MeV, which ensures a good capability to reduce background events.

The reconstructed invariant mass of the three muons is depicted in figure 6.18(a) before applying any cut. Figure 6.18(b) is showing the  $N-1$  representation.

All events located outside the range of  $|m_\tau - m_{3\mu}| < 80$  MeV are rejected by this cut.

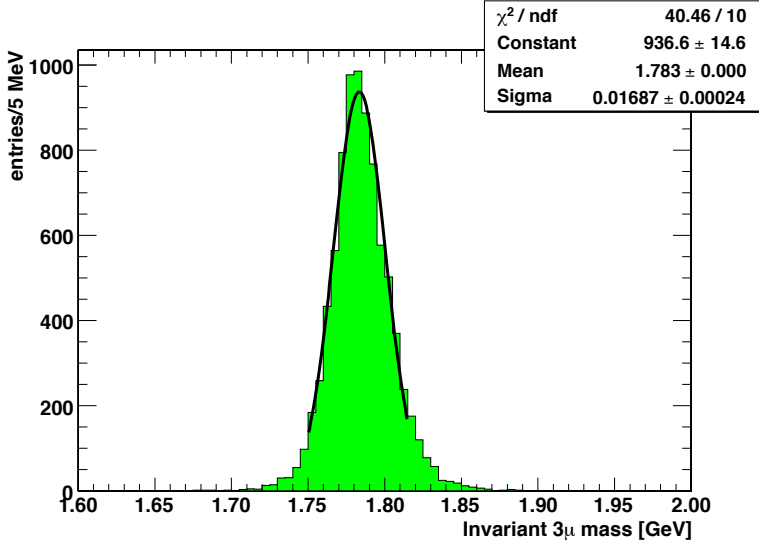


**Figure 6.17:**  $\tau \rightarrow \mu\mu\mu$  mass resolution for  $\tau$  leptons originated by  $W$  bosons obtained by gaussian fit.

### $\chi^2$ of the Secondary Vertex Fit

Beside the number of tracks compatible with the reconstructed secondary vertex, the  $\chi^2/\text{ndf}$  value of the vertex fit is an alternative approach and can be used additionally to reject backgrounds. Due to the high cross section of the background processes and the limited number of available background events, it is not reasonable to use this cut in the further analysis, since the number of background events passing the event selection is not reduced. Nevertheless this cut can be important later on, when the backgrounds are determined from the data itself and a high enough statistic is available. The  $\chi^2/\text{ndf}$  value of the fitted secondary vertex is depicted in figure 6.19(a) before applying any cut. Figure 6.19(b) is showing the  $N$ -1 representation.

The cut value of  $\chi^2/\text{ndf} < 4$  has been optimized by maximizing the product of efficiency and purity.

### $\phi$ Mass Exclusion Cut

The mass difference between the  $\phi$  mass and the invariant mass of any opposite charge di-muon combination can be used to reject one of the rare decays that mimic the signal,  $D_s \rightarrow \phi \mu \nu_\mu$  followed by a decay  $\phi \rightarrow \mu \mu$ . For each event, three invariant di-muon masses can be calculated, therefore each event is represented by two entries in the distribution depicted in figure 6.20.

Similar to the previous cut, no additional background events are rejected, due to the limited number of background events available. For the analysis of real data this cut becomes important, due to the higher number of expected  $\phi \rightarrow \mu \mu$  events.

The mass difference between the  $\phi$  mass and the invariant mass of any di-muon combination is depicted in figure 6.20(a) before any other is applied. The  $N$ -1 representation is shown in figure 6.20(b).

Due to the sharp  $\phi$  resonance of  $m_\phi = 1019 \pm 0.019$  MeV it is only necessary to reject a small region of  $|m_{2\mu} - m_\phi| < 10$  MeV. The value of the cut has been optimized by

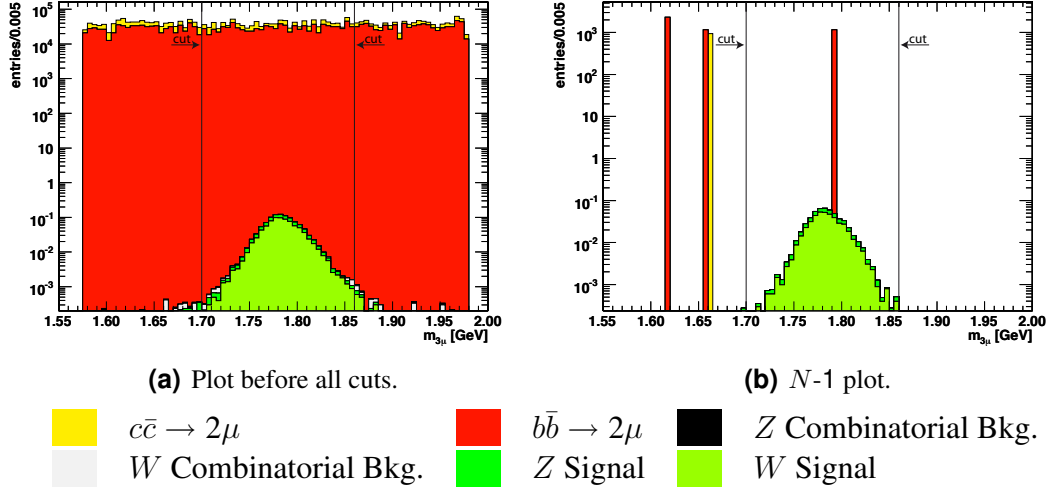


**Figure 6.18:** Invariant mass of the three reconstructed muons  $m_{3\mu}$ .

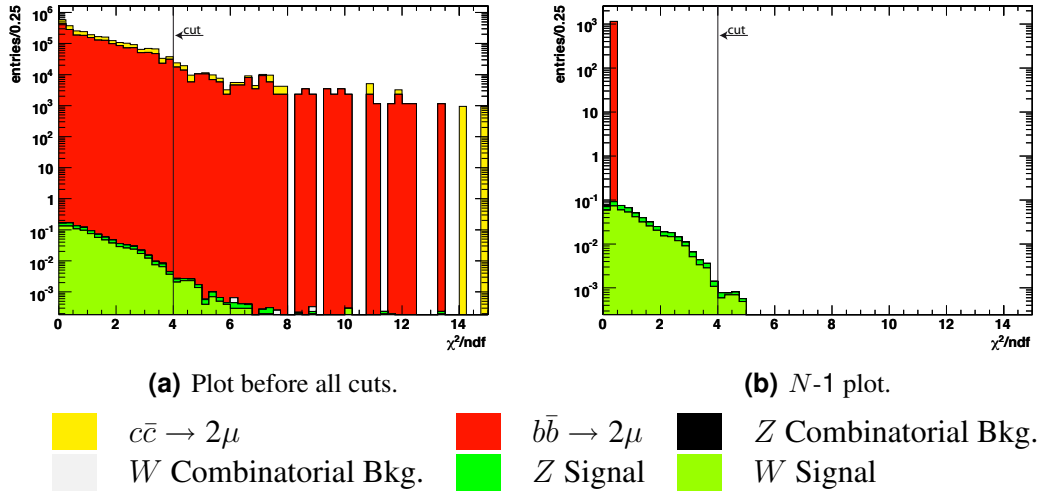


**Figure 6.19:** The  $\chi^2/\text{ndf}$  value of the fitted secondary vertex.

maximizing the product of efficiency and purity.

### Collimation of the Three Reconstructed Muons

As described in section 6.3 the three muons originated by the  $\tau \rightarrow \mu\mu\mu$  decay are very collimated. The sum over the distance measured in  $\Delta R$  between any combination of two muons offers a good opportunity to reject backgrounds, where at least one muon has a large distance to the remaining ones. This cut has also no influence on the number of remaining background events. For the later analysis of real data this cut can be taken into account as an additional possibility for a background rejection.

In figure 6.21(a) the sum over the distance measured in  $\Delta R$  is depicted before any other cut is applied. The  $N-1$  representation is shown in figure 6.21(b).

The value of the cut has been optimized by maximizing the product of efficiency and purity. All events having a  $\sum \Delta R_{ij} > 0.4$  are rejected.

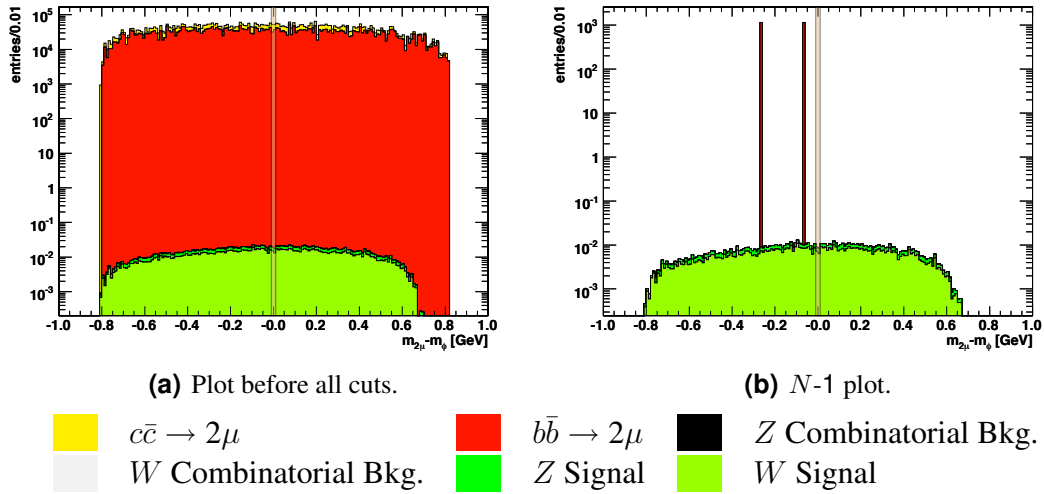


**Figure 6.20:** Mass difference between the  $\phi$  mass and the invariant mass of any opposite charge di-muon combination. The rejected region is highlighted.

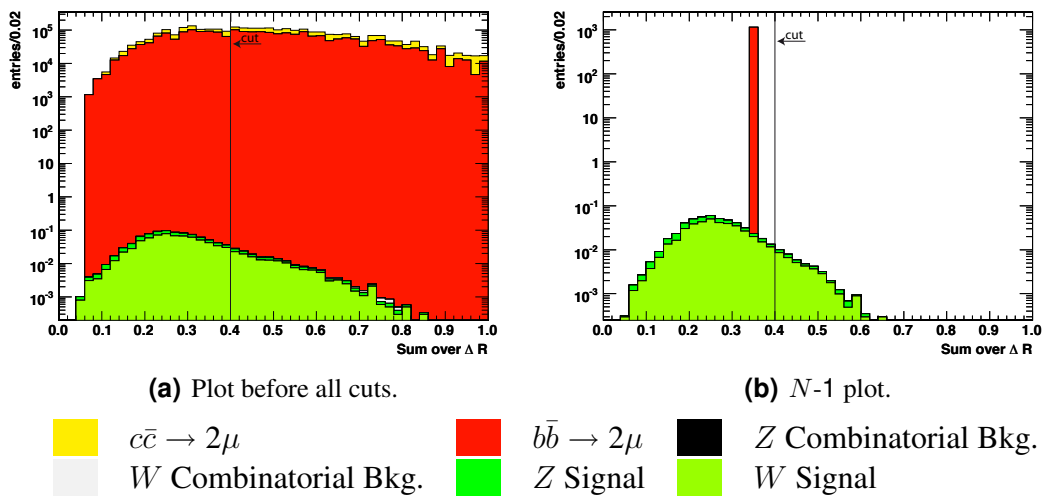


**Figure 6.21:** Sum over the distance measured in  $\Delta R$  between any combination of two muons.

A summary about the events passing the particular steps in the event selection process is given in table 6.9 and the corresponding progress of the signal-to-noise ratio is shown in table 6.10.

Process	$W$ source		$Z$ source	
	# events	ratio	# events	ratio
Production	50000	100%	50000	100%
Skimming	50000	100%	50000	100%
Trigger	10075	20.2%	13080	26.2%
Preselection	8527	17.1%	11044	22.1%
Selection	4358	8.7%	5472	10.9%
Selection (scaled to $10 \text{ fb}^{-1}$ )	0.43		0.10	
Process	$c\bar{c} \rightarrow 2\mu$		$b\bar{b} \rightarrow 2\mu$	
	# events	ratio	# events	ratio
Production	983424	100%	2794900	100%
Skimming	130576	13.3%	314325	11.2%
Trigger	4025	0.4%	11758	0.4%
Preselection	793	$8 \times 10^{-4}$	2097	$7.5 \times 10^{-4}$
Selection	0	0%	1	$3.6 \times 10^{-8}$
Selection (scaled to $10 \text{ fb}^{-1}$ )	0		1155	

**Table 6.9:** Summary of the total process of event selection. The combinatorial backgrounds of the  $W$  and  $Z$  sources which are related to the  $2\mu + \text{track}$  strategy are completely negligible.

Process	$S/N$
Production	$1.4 \times 10^{-9}$
Skimming	$1.2 \times 10^{-8}$
Trigger	$7.1 \times 10^{-8}$
Preselection	$3.3 \times 10^{-7}$
Selection	$4.6 \times 10^{-4}$

**Table 6.10:** Progress of the signal-to-noise ratio after each step in the event selection.

## 6.6 The Remaining Background Event

There is one background event passing the signal selection. It has been studied to understand the underlying physics process. It is important to know, whether it is originated by a physics process that mimics the signal and was not considered before or if the event accidentally passes the signal selection.

The remaining background event belongs to the  $b\bar{b} \rightarrow 2\mu$  background sample. It is the following decay cascade of a  $B^-$  meson.

$$\begin{aligned}
B^- &\rightarrow \bar{D}_2^{0*} \mu^- \nu_\mu \\
&\hookrightarrow \pi^- D^+ \\
&\hookrightarrow \bar{K}^0 \mu^+ \nu_\mu
\end{aligned}$$

The event has two reconstructed global muons and the third track found in the surrounding of both is associated to the pion. The alternative muon identification described in section 4.4 returns a likelihood ratio of  $p_\mu = 1.0$ , therefore the pion is clearly identified as muon. The following input variables are used to obtain the likelihood ratio of the alternative muon identification

- ECAL energy: 0.46 GeV,
- HCAL energy: 4.26 GeV,
- Number of reconstructed muon segments: 6,
- Pseudo-rapidity:  $\eta$ : 2.0.

Comparing these input variables with the distributions shown in section 4.4, it is obvious that the pion is identified as muon by the likelihood. The reason for the muon-like input variables is visible in the event display of the background event depicted in figure 6.22.

The reconstructed track of the pion is very close to one of the reconstructed muons. In order to obtain the calorimeter energy entries and the number of muon segments associated with the track, it is necessary to propagate it through the entire detector. As described in section 4.4 the TrackAssociator and the SteppingHelixPropagator, respectively, is used for that purpose. The TrackAssociator is using certain cones around the propagated track to do the association between calorimeter energies, reconstructed muon segments and the track. Since the pion is very close to the muon, most probably the resulting input variables for the likelihood ratio refer to the muon. Thus the pion is mistakenly identified as a muon.

Also for the other cuts used in the signal selection the background event is very signal-like. It is reasonable to claim that the background event accidentally passes the signal selection and it is not originated by a physics process which mimics the signal.

## 6.7 Uncertainties of the Study

Considering the statistical error  $n_{\text{bg}} = 1 \pm 1$  background events passing the selection criteria. Due to the huge scaling factors for the background processes the number of background events scaled to an integrated luminosity of  $10 \text{ fb}^{-1}$  including the statistical error is  $n_{\text{bg}_{\text{scaled}}} = 1155 \pm 1155$ . Thus the analysis is currently limited through the low background Monte Carlo statistic. The preferable way for the later analysis on data is the determination of background contributions from the data itself using sidebands.

The number of signal events passing the selection criteria including the statistical error is  $n_{\text{signal}_W} = 4358 \pm 66$  for the  $W$  source and  $n_{\text{signal}_Z} = 5472 \pm 74$  for the  $Z$  source, respectively. Scaled to an integrated luminosity of  $10 \text{ fb}^{-1}$  the number signal

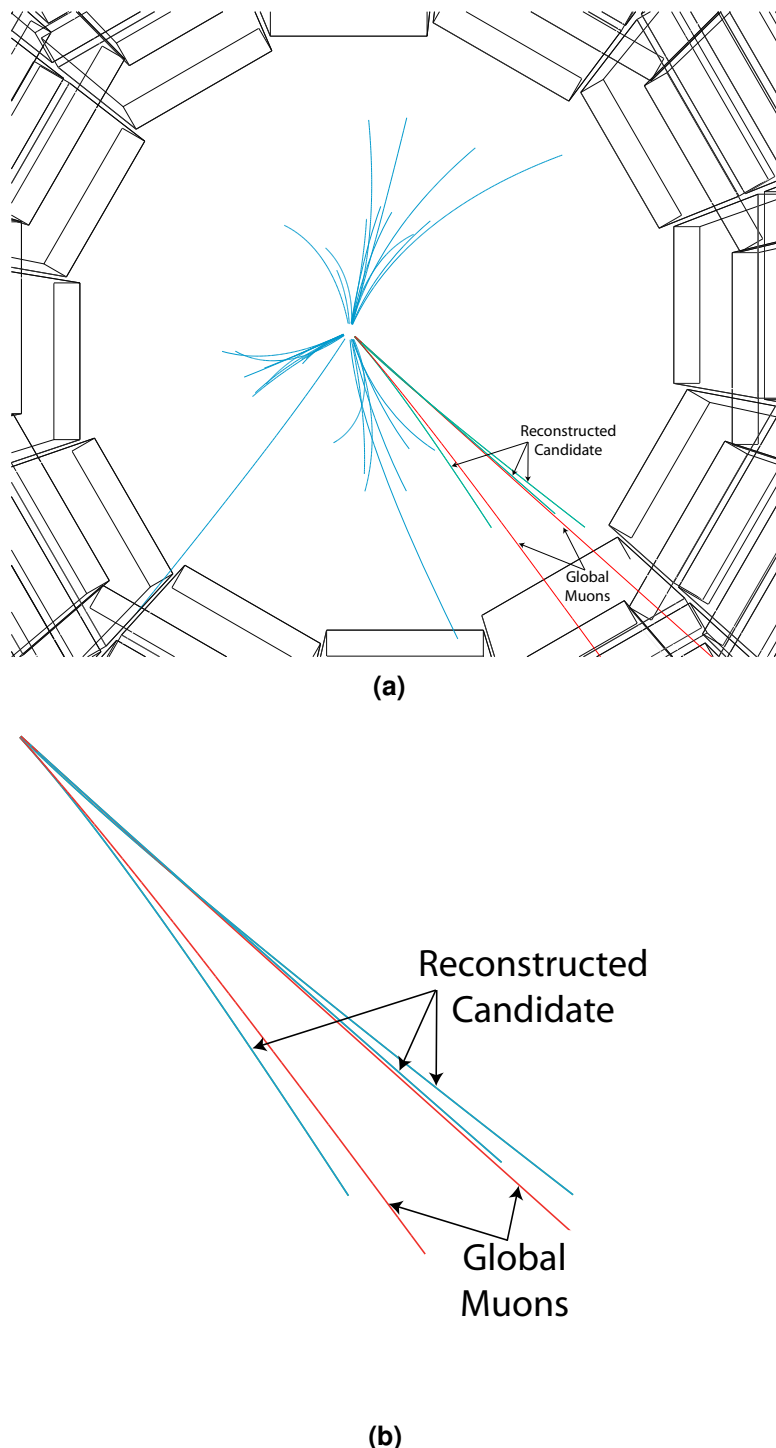


**Figure 6.22:** Event display of the background event mistakenly passing the event selection.

events passing the selection is  $n_{\text{signal}_W} = 0.430 \pm 0.007$  and  $n_{\text{signal}_Z} = 0.103 \pm 0.001$ . The signal efficiency of the total selection process including statistical uncertainties is  $8.72 \pm 0.13\%$  for the  $W$  source and  $10.99 \pm 0.15\%$  for the  $Z$  source. In comparison to the statistical uncertainties on the number of background events mistakenly passing the selection criteria, the statistical uncertainties on the signal selection are completely negligible.

To estimate the systematic uncertainties of this analysis a variation of the cuts is done. Only one cut is varied at a time by  $\pm 10\%$ , all other used cuts are applied with their usual thresholds mentioned in section 6.5.3. The variation of cuts is only done for the signal events so far, since a variation for the background samples is not changing the number of events mistakenly passing the event selection, due to the lack of background Monte Carlo statistics. However, assuming that the systematic uncertainties are in the same order of magnitude as for the signal events, they are completely negligible in comparison to the statistical uncertainties of the background samples. The results obtained for the signal samples are shown in table 6.11.

Cut variation	$W$ source		$Z$ source	
	$-10\%$	$+10\%$	$-10\%$	$+10\%$
Muon ID	+0.07%	-0.07%	+0.13%	-0.13%
$3\mu$ invariant mass	+0.14%	-0.09%	+0.07%	-0.24%
Isolation $p_T$	+0.37%	-0.34%	+0.53%	-0.35%
Isolation Cone	+0.80%	-0.18%	+0.62%	-0.58%

**Table 6.11:** *Relative deviations of the number of events passing the event selection from mean value obtained by a variation of the particular cut. A variation of  $-10\%$  means to loosen a cut by 10%, whereas a variation of  $+10\%$  means to tighten a cut by 10%.*

Only the cuts applied in the current event selection are varied to estimate the systematic uncertainties. For the cut on the number of tracks compatible with the secondary vertex fit, a variation of  $\pm 10\%$  is not applicable, because this cut contains only integer values and it is not reasonable to require only two vertex compatible tracks for this analysis. For the required signal isolation, the  $p_T$  threshold of allowed tracks inside the signal isolation cone and the radius of that cone have been varied independent from each other by  $\pm 10\%$ , instead of a variation of the number of tracks inside the signal isolation cone.

To determine a global systematic uncertainty  $\sigma_{\text{sys}}$  from each uncertainty obtained by the individual cut variation, the conservative approach of a quadratic sum over the individual systematic uncertainties  $\sigma_{\text{sys}_i}$  is used.

$$\sigma_{\text{sys}} = \sqrt{\sum_i \sigma_{\text{sys}_i}^2}$$

The number of signal events passing the event selection including the statistical and systematic uncertainties is

$$n_{\text{signal}_W} = 4358^{+39}_{-17}(\text{sys.}) \pm 66(\text{stat.})$$

for the  $W$  source and

$$n_{\text{signal}_Z} = 5472^{+45}_{-40}(\text{sys.}) \pm 74(\text{stat.})$$

for the  $Z$  source, respectively. Scaled to an integrated luminosity of  $10 \text{ fb}^{-1}$ , this is equivalent to

$$n_{\text{signal}_W} = 0.430^{+0.004}_{-0.002}(\text{sys.}) \pm 0.007(\text{stat.})$$

and

$$n_{\text{signal}_Z} = 0.1028^{+0.0008}_{-0.0008}(\text{sys.}) \pm 0.0014(\text{stat.}).$$

The signal efficiency of the total selection process including statistical and systematic uncertainties is

$$8.72^{+0.08}_{-0.03}(\text{sys.}) \pm 0.13(\text{stat.})\%$$

for the  $W$  source and

$$10.99^{+0.09}_{-0.08}(\text{sys.}) \pm 0.15(\text{stat.})\%$$

for the  $Z$  source. The statistical and the systematic uncertainties are roughly in the same order of magnitude for the signal events. However, the uncertainties of the background events are clearly dominated by statistical error. For the following calculation of the upper limit on the  $\tau \rightarrow \mu\mu\mu$  branching ratio, the statistical error on the background is dominating, therefore the statistical and the systematic uncertainties on the signal events is neglected.

## 6.8 Determination of an Upper Limit

The primary goal of this analysis is to determine the sensitivity of CMS to the neutrinoless  $\tau \rightarrow \mu\mu\mu$  decay. The physical observable to measure is the branching ratio  $\mathcal{B}_r$  of the decay.

Even if the signal-to-background ratio can be improved from  $S/B = 1.4 \times 10^{-9}$  before applying the event selection to  $S/B = 4.6 \times 10^{-4}$  after applying the event selection, the  $\tau \rightarrow \mu\mu\mu$  decay cannot be observed directly in CMS. Therefore an upper limit on the branching ratio is calculated to obtain the sensitivity of the analysis.

The upper limit on the average number of signal events  $\langle n_{\text{sig}} \rangle$  compatible with the background expectation depends on three parameters, the number of expected background events  $n_{\text{bg}}$ , the number of observed events  $n_{\text{obs}}$  and the required confidence level. Therefore, the upper limit depends on the considered luminosity.

For small numbers of expected background events the unified approach to the classical statistical analysis of small signals by Feldman and Cousins [81] is used. This approach is technically implemented in the `TFeldmanCousins` class of the root analysis framework [82]. For the calculation of the upper confidence belt, the three mentioned parameters are needed. The confidence level (CL) used for the limit calculation is set to  $CL = 90\%$ . The number of expected background event can be obtained from the number of background events mistakenly accepted by the event selection. The last parameter, the number of observed events, is varied over a reasonable range in order to obtain the upper confidence belt.

For a number of expected background events of around 70 it has turned out that it is more reasonable to use the classical approach to determine the upper confidence belt, since the results are comparable and the necessary CPU power is much lower. In the classical approach the error on the number of measured events  $N$  is given by  $\sigma = \sqrt{N}$ ,

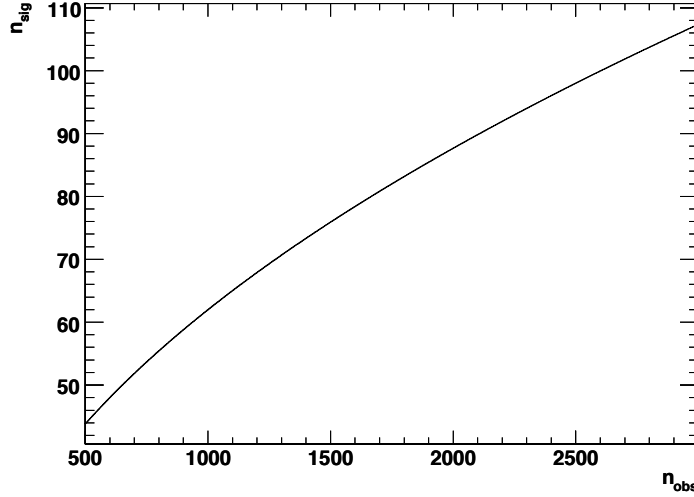


**Figure 6.23:** *Upper confidence belt obtained by the classical approach for a confidence level of  $CL = 90\%$ .*

which is equivalent to a confidence level of  $CL = 68\%$ . The upper confidence belt at the favoured confidence level is given by

$$\alpha \cdot \sqrt{N} \quad \text{with } \alpha > 0.$$

The factor is  $\alpha = 1.96$  for a confidence level of  $CL = 90\%$  (see figure 6.23).

To calculate the average upper limit for the number of signal events  $\langle n_{\text{sig}} \rangle$  compatible with the background expectations, the upper confidence belt is convolved with a Poisson distribution and integrated over a reasonable range.

$$\langle n_{\text{sig}} \rangle = \sum_{n_{\text{obs}}} UL_{90\%CL}(n_{\text{obs}}) \times P(n_{\text{obs}} | n_{\text{bg}} = 1155) \times \Delta n_{\text{step}} \quad (6.5)$$

To get the average upper limit on the branching ratio  $\langle \mathcal{B}_r \rangle$  the following relation is used.

$$\langle \mathcal{B}_r \rangle = \frac{\langle n_{\text{sig}} \rangle}{N_\tau \times \epsilon_{\text{analysis}}} \quad (6.6)$$

The number of expected background events for an integrated luminosity of  $10 \text{ fb}^{-1}$  is  $1155 \pm 1155$ . The problem is the statistical uncertainty. Only one  $b\bar{b} \rightarrow 2\mu$  background event survives the event selection. Therefore, the statistical error is large, due to a scaling factor of roughly 1155.

For the  $\tau \rightarrow \mu\mu\mu$  decays originated by the  $W$  boson a signal efficiency of 8.7% is expected. The number of  $\tau$  leptons produced by  $W$  decays is  $1.5 \cdot 10^8$  for an integrated luminosity of  $10 \text{ fb}^{-1}$ . The average upper limit for the number of signal events compatible with the background expectations is  $\langle n_{\text{sig}} \rangle = 66.6$  obtained by using equation 6.5. With equation 6.6 the average upper limit on the  $\tau \rightarrow \mu\mu\mu$  decay can be obtained. Including the statistical uncertainties, the average upper limit is

$$\mathcal{B}_r = 5.1_{-4.9}^{+2.1} \cdot 10^{-6}$$

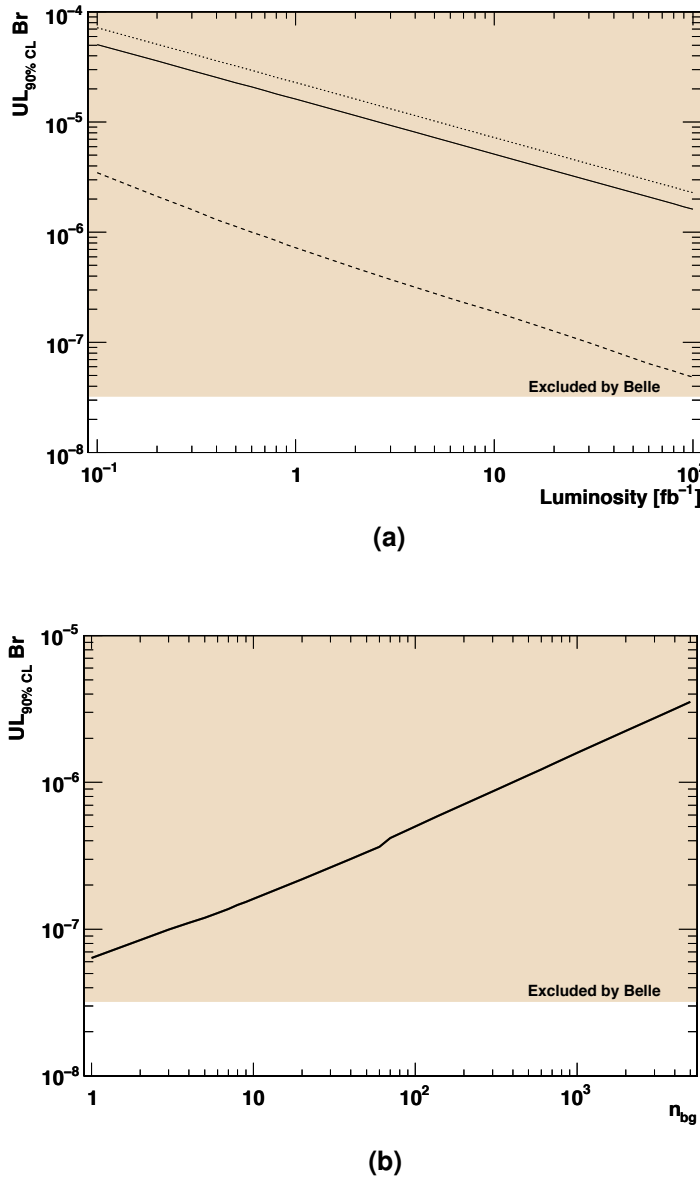


**Figure 6.24:** Average upper limit for the branching ratio of  $\tau \rightarrow \mu\mu\mu$  originated by the  $W$  source as function of the integrated luminosity (a) and as function of the number of background events for an integrated luminosity of  $30 \text{ fb}^{-1}$  (b). The solid line represents the mean value ( $n_{bg} = 1155$ ), whereas the dotted and the dashed line representing the statistical uncertainty.

for an integrated luminosity of  $10 \text{ fb}^{-1}$  using only  $\tau$  leptons produced by  $W$  decays. The achievable upper limit as function of the integrated luminosity is depicted in figure 6.24(a). Due to the low number of background events expected for the dashed line, the approach of Feldman and Cousins is used to calculate the upper confidence belt. Since this analysis is done for the low luminosity phase of LHC it is reasonable to consider only integrated luminosities up to  $100 \text{ fb}^{-1}$ . This assumes an integrated luminosity of roughly  $33 \text{ fb}^{-1}$  per year and a running time of three years at a luminosity of  $\mathcal{L} = 2 \times 10^{33} \text{ cm}^{-2} \text{ s}^{-1}$ , which is a very optimistic scenario. To obtain an upper limit for integrated luminosities beyond  $100 \text{ fb}^{-1}$ , the more stringent trigger thresholds and increasing pile-up have to be considered. The achievable upper limit as function of the background expectation for an integrated luminosity of  $30 \text{ fb}^{-1}$  is shown in figure 6.24(b). The bend in the curve between  $n_{bg} = 70\text{--}80$  is referable to the transition from the approach of Feldman and Cousins to the classical approach.

From both plots in figure 6.24 it is evident, that sensitivity of the analysis is not competitive to the recently published results of Belle. However, this study is limited to the low luminosity phase of the LHC, due to the assumption made for the trigger paths and the missing pile-up events in the Monte Carlo simulation. An improvement of the sensitivity during the high luminosity phase ( $\mathcal{L} = 10^{34} \text{ cm}^{-2} \text{ s}^{-1}$ ) might be possible and needs to be studied in the future. To reduce the statistical error on the number of background events passing the event selection it is preferable to determine the background contributions from the data itself.

The upper limit for  $\tau \rightarrow \mu\mu\mu$  decay originated by  $Z$  bosons is calculated in a similar way. The result for the upper limit on the branching ratio including statistical uncertainties is

$$\mathcal{B}_r = 2.1_{-2.0}^{+0.9} \cdot 10^{-5}$$

for an integrated luminosity of  $10 \text{ fb}^{-1}$  using only  $\tau$  leptons produced by  $Z$  decays. The achievable upper limit as function of the integrated luminosity as well as the upper limit as function of the number of expected background events is depicted in figure A.4.

The combined results for the upper limit including statistical uncertainties is

$$\mathcal{B}_r = 4.1_{-4.0}^{+1.7} \cdot 10^{-6}$$

for an integrated luminosity of  $10 \text{ fb}^{-1}$ . The achievable upper limit as function of the integrated luminosity as well as the upper limit as function of the number of expected background events is depicted in figure A.3.

Integrated luminosity	$1 \text{ fb}^{-1}$	$10 \text{ fb}^{-1}$	$30 \text{ fb}^{-1}$	$100 \text{ fb}^{-1}$
Upper limit $\mathcal{B}_r$ ( $W$ source)	$1.6 \times 10^{-5}$	$5.1 \times 10^{-6}$	$3.0 \times 10^{-6}$	$1.6 \times 10^{-6}$
Upper limit $\mathcal{B}_r$ ( $Z$ source)	$6.7 \times 10^{-5}$	$2.1 \times 10^{-5}$	$1.2 \times 10^{-5}$	$6.7 \times 10^{-6}$
Upper limit $\mathcal{B}_r$ (combined)	$1.3 \times 10^{-5}$	$4.1 \times 10^{-6}$	$2.4 \times 10^{-6}$	$1.3 \times 10^{-6}$

**Table 6.12:** Average upper limit on the branching ratio  $\mathcal{B}_r(\tau \rightarrow \mu\mu\mu)$  for various sources and integrated luminosities.

An overview of the achievable upper limits (mean values only) for various integrated luminosities is shown in table 6.12.



# Chapter 7

## Summary and Outlook

This thesis deals with the neutrinoless and therefore lepton flavour violating  $\tau$  decay  $\tau \rightarrow \mu\mu\mu$  and in particular with the sensitivity of the CMS experiment to this decay. About  $10^{12}$   $\tau$  leptons are produced per year already during the low luminosity ( $\mathcal{L} = 2 \times 10^{33} \text{ cm}^{-2} \text{ s}^{-1}$ ) phase of LHC. The copious  $\tau$  production at the LHC provides an excellent potential for the search of lepton flavour violation in  $\tau$  decays. The dominant sources of  $\tau$  leptons at the LHC are the  $D_s$  and various  $B$  mesons. Unfortunately, those events are hardly triggered and reconstructed, due to their low transverse momentum of the muons. The  $W$  and the  $Z$  sources will provide considerably less  $\tau$  leptons per year ( $\sim 10^8$ ), but at higher energies which is an advantage for the efficient detection of their decay products. The  $\tau$  leptons originated by  $W$  bosons turned out to be best suited for the analysis.

For a realistic Monte Carlo simulation including the model dependent angular distributions, the decay  $\tau \rightarrow \mu\mu\mu$  was implemented into the event generator PYTHIA using various matrix elements, which have been calculated in a model independent approach using a generic Lagrangian by theory groups of the RWTH Aachen and the University of Siegen. The impact on relevant physical distributions has been studied on generator level for different extensions of the Standard Model. For this study, detector acceptance cuts were defined and it turned out, that the assumed models leading to the  $\tau \rightarrow \mu\mu\mu$  decay have no significant impact on the detection power of CMS. In addition, a possible separation of these models was discussed. The only way to do a model separation is the angular distribution of the models. Due to the dependency of the angular distribution from the  $\tau$  polarization, only the  $W$  source can be used in order to distinguish between the models. However, depending on the branching ratio of the  $\tau \rightarrow \mu\mu\mu$  decay, the LHC have to run at least a few years on high luminosity to be able to pin down a model.

Three muons in the final state actually provide a clean signature from the reconstruction and trigger point of view. However, the three muons are highly collimated, at least for the  $W$  and  $Z$  sources, and the softest muon has mostly a low transverse momentum. The standard muon reconstruction is often not working for these tracks. The reconstruction efficiency of the  $\tau \rightarrow \mu\mu\mu$  decay can be improved by roughly a factor of two, if only two global reconstructed muons and a third adjacent track in the silicon tracker is required. To reduce the raising backgrounds, an alternative muon identification based on a likelihood ratio has been developed, using the energy depositions in the

calorimeter and the number of reconstructed segments in the muon system. Also the High Level Trigger is affected by the above mentioned reconstruction issues, since the official muon HLT is using the same reconstruction algorithms as the muon reconstruction. In particular, a failed matching between the reconstructed segment in the muon system and the track in the silicon tracker leads to a drop of the trigger efficiency. Therefore, a dedicated  $\tau \rightarrow \mu\mu\mu$  trigger algorithm with lower  $p_T$  thresholds and a changed Level 3 reconstruction has been implemented into CMSSW, which is now part of the official trigger menu. However, this trigger needs further improvements, also with respect to a possible enhancement of the trigger efficiency of  $\tau \rightarrow \mu\mu\mu$  decays originated by  $D_s$  and  $B$  mesons.

The sources of backgrounds are Standard Model decays which mimic the signal process. The main backgrounds are decays of various  $D$  and  $B$  mesons which are copiously produced at the LHC. One example for such a decay that mimic the signal is  $D_s \rightarrow \phi\mu\nu_\mu$  followed by a decay  $\phi \rightarrow \mu\mu$  or the radiative decay  $\phi \rightarrow \mu\mu\gamma$ . The considered background samples in this study are the  $c\bar{c} \rightarrow 2\mu + X$  and  $b\bar{b} \rightarrow 2\mu + X$  datasets. The preferable way for the latter analysis, is the determination of the background contributions from the data itself using sidebands, since not all of those decays are implemented in the event generators.

The primary goal of this study is the determination of the sensitivity of CMS to the neutrinoless  $\tau \rightarrow \mu\mu\mu$  decay. The study is currently limited by the Monte Carlo statistic for the background events. After applying the event selection, one background event is mistakenly passing the cuts. However, the scaling factor to an integrated luminosity of  $10 \text{ fb}^{-1}$  is 1155, the expected number of background events for  $10 \text{ fb}^{-1}$  including the statistical error is  $n_{bg} = 1155 \pm 1155$ . Statistical uncertainties for the signal samples and the systematic uncertainties can be neglected for the calculation of an upper limit on the branching ratio. Using  $\tau \rightarrow \mu\mu\mu$  events originated by the  $W$  source and assume an integrated luminosity of  $10 \text{ fb}^{-1}$ , the achievable upper limit with a confidence level of  $CL = 90\%$  is  $\mathcal{B}_r(\tau \rightarrow \mu\mu\mu) = 5.1_{-4.9}^{+2.1} \cdot 10^{-6}$  with a high statistical uncertainty, due to the low Monte Carlo statistic of background events. Compared to the current upper limit published by the  $b$  factories of  $\mathcal{B}_r(\tau \rightarrow \mu\mu\mu) = 3.2 \cdot 10^{-8}$ , the analysis is currently not competitive with them. However, this study is limited to the low luminosity phase of the LHC, due to the assumption made for the trigger paths and the missing pile-up events in the Monte Carlo simulation. An improvement of the sensitivity during the high luminosity phase ( $\mathcal{L} = 10^{34} \text{ cm}^{-2} \text{ s}^{-1}$ ) might be possible and needs to be studied in the future. Additionally, the reconstruction and the trigger algorithms can be further improved in the future, also with respect to the copious  $\tau$  production sources at the LHC, the  $D_s$  and the  $B$  mesons. To reduce the statistical error on the number of background events passing the event selection it is preferable to determine the background contributions from the data itself.

# Appendix A

## Physics Add-Ons

### A.1 CMSSW Configurations

#### A.1.1 $\tau \rightarrow \mu\mu\mu$ Implementation

```
vstring pythia_Tau3mu =
{
    #Add tau->mu mu mu decay

    "MDCY(15, 2)=89",
    "MDCY(15, 3)=55",

    "MDCY(16, 2)=4300",
    "MDCY(16, 3)=2",

    "KFDP(143, 1)=13",
    "KFDP(143, 2)=-13",
    "KFDP(143, 3)=13",
    "KFDP(143, 4)=0",
    "KFDP(143, 5)=0",

    "MDME(143, 2)=0           !no special matrix element",
    "BRAT(143)=1.0           !BR=1",

    "KFDP(4300, 1)=23",
    "KFDP(4300, 2)=16",
    "KFDP(4300, 3)=0",
    "KFDP(4300, 4)=0",
    "KFDP(4300, 5)=0",
    "BRAT(4300)=0.0",
    "MDME(4300, 2)=102",
    "MDME(4300, 1)=1",

    "KFDP(4301, 1)=24",
    "KFDP(4301, 2)=15",
    "KFDP(4301, 3)=0",
    "KFDP(4301, 4)=0",
    "KFDP(4301, 5)=0",
    "BRAT(4301)=0.0",
    "MDME(4301, 2)=102",
    "MDME(4301, 1)=1"
}
```

## A.2 Muon Resolution

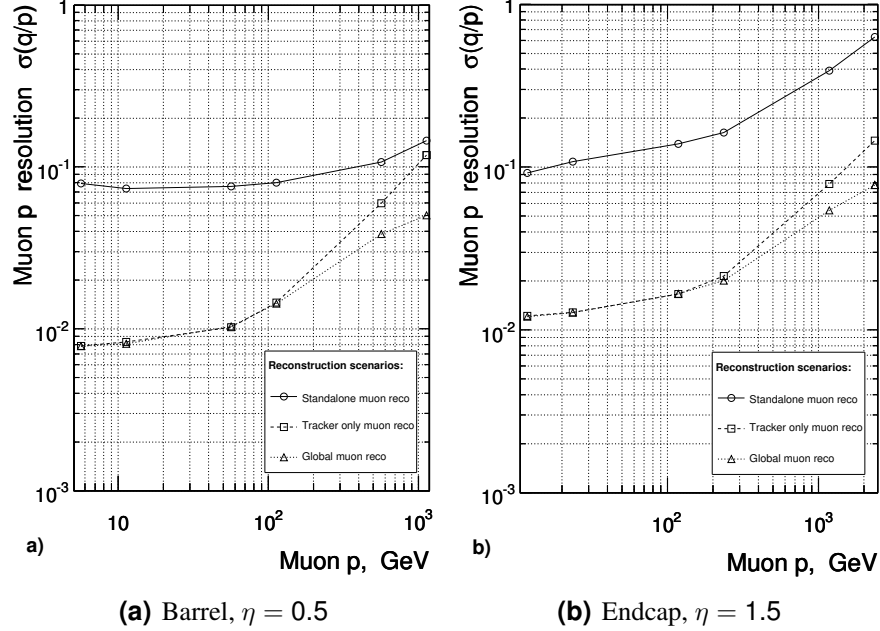


**Figure A.1:** Resolution of  $1/p$  versus  $p$  for standalone, global and tracker-only reconstructed muons [27].

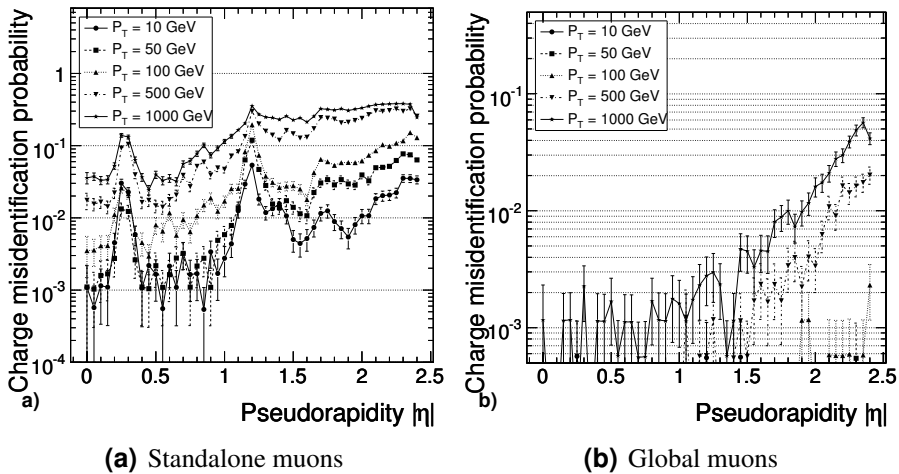


**Figure A.2:** Charge misidentification probability for muons as function of the pseudo-rapidity [27].

### A.3 Limit Calculation

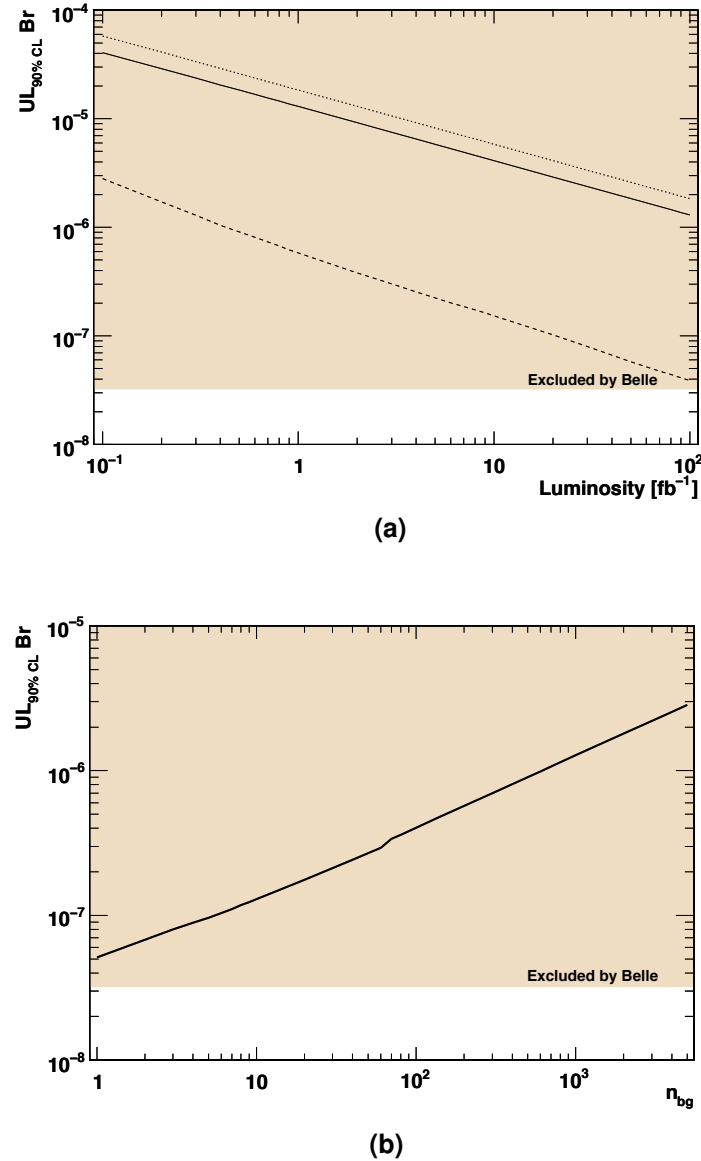


**Figure A.3:** Average upper limit for the branching ratio of  $\tau \rightarrow \mu\mu\mu$  for the combination of the  $W$  and the  $Z$  source as function of the integrated luminosity (a) and as function of the number of background events for an integrated luminosity of  $30 \text{ fb}^{-1}$  (b). The solid line represents the mean value ( $n_{bg} = 1155$ ), whereas the dotted and the dashed line representing the statistical uncertainty.

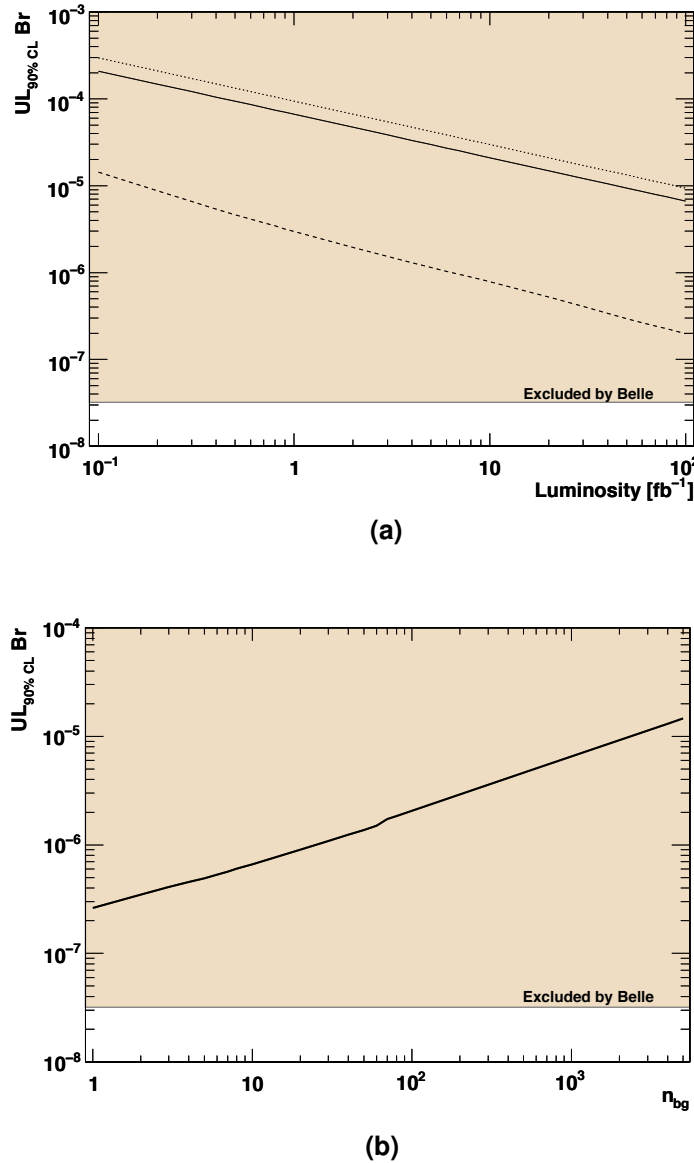


**Figure A.4:** Average upper limit for the branching ratio of  $\tau \rightarrow \mu\mu\mu$  originated by the  $Z$  source as function of the integrated luminosity (a) and as function of the number of background events for an integrated luminosity of  $30 \text{ fb}^{-1}$  (b). The solid line represents the mean value ( $n_{bg} = 1155$ ), whereas the dotted and the dashed line representing the statistical uncertainty.

# List of Figures

1.1	Particles of the Standard Model and their masses in GeV . . . . .	1
1.2	Feynman diagram for the $\tau \rightarrow \mu\mu\mu$ decay in the Standard Model . . . . .	4
1.3	Feynman diagram for the $\tau \rightarrow \mu\mu\mu$ decay in a SUSY Seesaw model . . . . .	5
1.4	Feynman diagram for the $\tau \rightarrow \mu\mu\mu$ decay in a RPV SUSY model . . . . .	6
1.5	Feynman diagram for the $\tau \rightarrow \mu\mu\mu$ decay in the Littlest Higgs Model . . . . .	6
1.6	Feynman diagram for the $\tau \rightarrow \mu\mu\mu$ decay in TC2 models . . . . .	7
1.7	Feynman diagram for the $\tau \rightarrow \mu\mu\mu$ decay in models with doubly-charged Higgs bosons . . . . .	8
2.1	The Large Hadron Collider . . . . .	9
2.2	Cross-sections and event rates of physics processes at hadron colliders . . . . .	11
2.3	The CMS detector . . . . .	13
2.4	The layout of the silicon pixel detector used in the CMS detector . . . . .	14
2.5	The layout of the Silicon Strip Detector of CMS . . . . .	15
2.6	The layout of the electromagnetic calorimeter of CMS . . . . .	16
2.7	The layout of the hadronic calorimeter of CMS . . . . .	17
2.8	The $r$ - $z$ view of a quarter of the CMS muon system . . . . .	19
3.1	The hit-and-miss method . . . . .	22
3.2	Production chain with the CMSSW framework in the version 1_6_x . . . . .	23
3.3	Tiered structure of the LHC computing grid . . . . .	25
3.4	The structure of the Grid Analysis Tool . . . . .	27
3.5	A screenshot of the Job Monitoring tool JoMo . . . . .	28
4.1	Track finding efficiency for muons and pions . . . . .	32
4.2	Resolution of the transverse impact parameter $d_0$ for muons . . . . .	32
4.3	The weight function of the adaptive vertex fitter . . . . .	34
4.4	Spatial deviation of the fitted secondary vertex to the generated vertex . . . . .	35
4.5	The layout of a DT chamber inside a muon barrel station . . . . .	36
4.6	Muon reconstruction efficiency as a function of $\eta$ . . . . .	39
4.7	The resolution of standalone and global muons as function of $\eta$ . . . . .	40
4.8	Associated energy deposition of the propagated track in the ECAL . . . . .	41
4.9	Associated energy deposition of the propagated track in the HCAL . . . . .	42
4.10	Associated energy deposition of the propagated track in the HO . . . . .	42
4.11	Track segments associated to the propagated track in the muon detectors . . . . .	43
4.12	Distribution of the likelihood ratio with muons and background . . . . .	44
4.13	Flowchart of the muon High Level Trigger . . . . .	46
4.14	Flowchart of the proposed dedicated $\tau \rightarrow \mu\mu\mu$ trigger . . . . .	47

4.15	Detailed flowchart of the $\tau \rightarrow \mu\mu\mu$ trigger algorithm . . . . .	48
5.1	Definition of the angle $\theta$ . . . . .	51
5.2	The $\tau$ lepton polarization as function of $\cos \theta$ for different values of $\sqrt{s}$	55
5.3	Resulting angular distributions for various considered models . . . . .	59
5.4	Resulting angular distributions for various considered models . . . . .	60
5.5	Influence of the different models to the transverse momenta . . . . .	61
5.6	Influence of the different models to observables considered to evaluate the detection power . . . . .	62
6.1	Leading order contribution to the heavy quark production . . . . .	65
6.2	Next-to-leading order contribution to the heavy quark production . . .	65
6.3	Contribution to the total cross section of charm and bottom production	66
6.4	Transverse momentum of the leading and next-to-leading muon . . . .	68
6.5	Transverse momentum of the next-to-next-to leading muon . . . . .	69
6.6	Pseudo-rapidity distribution of the muons . . . . .	70
6.7	Distribution of the maximum distance between two muons . . . . .	71
6.8	Distribution of the minimum distance between two muons . . . . .	71
6.9	A $\tau \rightarrow \mu\mu\mu$ event with three reconstructed global muons . . . . .	74
6.10	A $\tau \rightarrow \mu\mu\mu$ event with two reconstructed global muons . . . . .	75
6.11	A $\tau \rightarrow \mu\mu\mu$ event with two reconstructed global muons and one additional reconstructed standalone muon . . . . .	76
6.12	Flowchart of the skimming procedure . . . . .	77
6.13	Flowchart of the preselection procedure . . . . .	78
6.14	Number of additional tracks in a $\Delta R = 0.3$ isolation cone . . . . .	79
6.15	Distribution of the likelihood ratio . . . . .	79
6.16	Number of tracks having a track weight of $w_i > 0.5$ in the adaptive vertex fit . . . . .	80
6.17	$\tau \rightarrow \mu\mu\mu$ mass resolution for $\tau$ leptons originated by $W$ bosons . . .	81
6.18	Invariant mass of the three reconstructed muons $m_{3\mu}$ . . . . .	82
6.19	The $\chi^2/\text{ndf}$ value of the fitted secondary vertex . . . . .	82
6.20	Mass difference between the $\phi$ mass and the invariant mass of any opposite charge di-muon combination . . . . .	83
6.21	Sum over the distance measured in $\Delta R$ . . . . .	83
6.22	The background event mistakenly passing the event selection . . . . .	86
6.23	Upper confidence belt obtained by the classical approach . . . . .	89
6.24	Average upper limit for the branching ratio of $\tau \rightarrow \mu\mu\mu$ originated by the $W$ source . . . . .	90
A.1	Resolution of $1/p$ versus $p$ for standalone, global and tracker-only reconstructed muons. . . . .	96
A.2	Charge misidentification probability for muons as function of the pseudo-rapidity. . . . .	96
A.3	Average upper limit for the branching ratio of $\tau \rightarrow \mu\mu\mu$ $W$ and $Z$ combined . . . . .	97
A.4	Average upper limit for the branching ratio of $\tau \rightarrow \mu\mu\mu$ originated by the $Z$ source . . . . .	98

# List of Tables

4.1	List of the applied cuts used for the likelihood ratio. . . . .	44
4.2	L1 Muon Trigger thresholds on $p_T$ . . . . .	46
4.3	HLT Muon Trigger $p_T$ thresholds for the low luminosity phase . . . . .	46
5.1	Extract of the PYTHIA decay table before modification . . . . .	49
5.2	Extract of the PYTHIA decay table after modification . . . . .	50
5.3	Probability for the configurations of the longitudinal $\tau$ polarization . .	53
5.4	The $Z$ couplings to fermions in the lowest order approximation. . . . .	54
5.5	Normalization factors for different models obtained using 100000 events	57
5.6	The coupling constants used in the generic matrix element implementation for various studied models . . . . .	57
5.7	CMS detector acceptance on MC level for various studied models . .	58
6.1	Numbers of produced $\tau$ leptons per year originated by $b$ and $c$ mesons	63
6.2	Numbers of produced $\tau$ leptons per year originated by $W$ and $Z$ mesons	64
6.3	Numbers of expected signal events per year . . . . .	64
6.4	Generated datasets available for analysis purposes . . . . .	67
6.5	Trigger efficiencies obtained by applying the CMS trigger thresholds to the Monte Carlo muons . . . . .	68
6.6	Estimated reconstruction efficiencies for the next-to-next-to leading muon . . . . .	69
6.7	Fraction of events inside of the sensitive detector volume . . . . .	70
6.8	Estimation of an upper limit on the number of events reconstructible with the CMS detector . . . . .	72
6.9	Summary of the total process of event selection . . . . .	84
6.10	Progress of the signal-to-noise ratio after each step in the event selection	84
6.11	Relative deviations of the number of events passing the event selection from mean value obtained by a variation of the particular cut . . . . .	87
6.12	Average upper limit on the branching ratio $\mathcal{B}_r(\tau \rightarrow \mu\mu\mu)$ . . . . .	91



# Bibliography

- [1] DESY. **TESLA**. Hamburg, 2000. [http://tesla.desy.de/new\\_pages/TDR\\_CD/brochure/tesla\\_ed.pdf](http://tesla.desy.de/new_pages/TDR_CD/brochure/tesla_ed.pdf).
- [2] E. NOETHER AND M. A. TAVEL. **Invariant Variation Problems**, 2005.
- [3] E. J. KONOPINSKI AND H. M. MAHMOUD. **The Universal Fermi Interaction**. *Phys. Rev.*, **92** (1953), 1024.
- [4] D. GRIFFITHS. **Introduction into elementary particles**. John Wiley & Sons inc., 1987, ISBN 0-471-60386-4.
- [5] R. DAVIS. **Report on the Homestake solar neutrino experiment**. *Front. Phys.*, **5** (1993), 47–60.
- [6] B. AHARMIM ET AL. **Measurement of the nu/e and total B-8 solar neutrino fluxes with the Sudbury Neutrino Observatory phase I data set**. *Phys. Rev.*, **C75** (2007), 045502.
- [7] T. KAJITA. **Atmospheric neutrino results from Super-Kamiokande and Kamiokande: Evidence for nu/mu oscillations**. *Nucl. Phys. Proc. Suppl.*, **77** (1999), 123–132.
- [8] M. GIFFELS, J. KALLARACKAL, M. KRÄMER, B. O’LEARY AND A. STAHL. **The lepton-flavour violating decay  $\tau \rightarrow \mu\mu\bar{\mu}$  at the LHC**. <http://arxiv.org/pdf/0802.0049>, (2008).
- [9] K. MAZUMDAR. **Lepton Flavour Violation at the LHC**. CMS CR 2004/013, May 2004, CERN.
- [10] J. KALARACKAL. **Lepton-Familien-Zahl-Verletzende Modelle**. Diploma thesis, Institut für Theoretische Physik, RWTH Aachen, Aug. 2007.
- [11] S. P. MARTIN. **A supersymmetry primer**. <http://arxiv.org/pdf/hep-ph/9709356>, (1997).
- [12] K. S. BABU AND C. KOLDA. **Higgs-Mediated  $\tau \rightarrow \mu\mu\mu$  in the Supersymmetric Seesaw Model**. *Phys. Rev. Lett.*, **89** (2002), 241802.
- [13] R. BARBIER, C. BERAT, M. BESANCON, M. CHEMTOB, A. DEANDREA, E. DUDAS, P. FAYET, S. LAVIGNAC, G. MOREAU, E. PEREZ, AND Y. SIROIS. **R-parity violating supersymmetry**. *Physics Reports*, **420** (2005), 1.

- [14] H.-C. CHENG AND I. LOW. **TeV symmetry and the little hierarchy problem.** *JHEP*, **09** (2003), 051. hep-ph/0308199.
- [15] N. ARKANI-HAMED, A. G. COHEN, T. GREGOIRE, E. KATZ, A. E. NELSON, AND J. G. WACKER. **The Minimal Moose for a Little Higgs.** *JHEP*, **0208** (2002), 021.
- [16] M. BLANKE, A. J. BURAS, B. DULING, A. POSCHENRIEDER, AND C. TARANTINO. **Charged Lepton Flavour Violation and (g-2)<sub>μ</sub> in the Littlest Higgs Model with T-Parity: a clear Distinction from Supersymmetry.** *JHEP*, **05** (2007), 013.
- [17] K. LANE. **Two lectures on technicolor.** <http://arXiv.org/pdf/hep-ph/0202255>, (2002).
- [18] C. AMSLER ET AL. **Review of Particle Physics**, 2008. Available on the PDG webpages (URL: <http://pdg.lbl.gov/>).
- [19] C. T. HILL. **Topcolor.** <http://arXiv.org/pdf/hep-ph/9702320>, (1996).
- [20] C. YUE, Y. ZHANG, AND L. LIU. **Non-universal gauge bosons  $Z'$  and lepton flavor-violation tau decays.** *Physics Letters B*, **547** (2002), 252.
- [21] C.-X. YUE, Z.-J. ZONG, L. ZHOU, AND S. YANG. **Lepton flavor violating signals of the neutral top-pion in future lepton colliders.** *Physical Review D*, **71** (2005), 115011.
- [22] A. G. AKEROYD, M. AOKI, AND Y. OKADA. **Lepton Flavour Violating tau Decays in the Left-Right Symmetric Model.** *Phys. Rev.*, **D76** (2007), 013004.
- [23] J. SCHECHTER AND J. W. F. VALLE. **Neutrino Masses in  $SU(2) \times U(1)$  Theories.** *Phys. Rev.*, **D22** (1980), 2227.
- [24] A. ZEE. **Quantum Numbers Of Majorana Neutrino Masses.** *Nucl. Phys.*, **B264** (1986), 99.
- [25] K. S. BABU. **Model of 'Calculable' Majorana Neutrino Masses.** *Phys. Lett.*, **B203** (1988), 132.
- [26] S. KASSELMANN. **Top Quark Mass Measurement in the Lepton+Jets Channel using Full Simulation of the CMS Detector.** PhD thesis, III. Physikalisches Institut, RWTH Aachen University, Germany, Nov. 2007.
- [27] THE CMS COLLABORATION. **CMS Physics Technical Design Report Vol I: Detector Performance and Software.** CERN/LHCC 2006-001, feb 2006.
- [28] O. S. BRÜNIG ET AL. **The LHC Design Report, Volume 1: The LHC Main Ring.** CERN 2004-003-v1, 1995/2004. URL: <http://ab-div.web.cern.ch/ab-div/Publications/LHC-DesignReport.html>.

- [29] O. S. BRÜNING ET AL. **The LHC Design Report, Volume 2: The LHC Infrastructure and General Services.** CERN 2004-003-v2, 1995/2004. URL: <http://ab-div.web.cern.ch/ab-div/Publications/LHC-DesignReport.html>.
- [30] O. S. BRÜNING ET AL. **The LHC Design Report, Volume 3: The LHC Injector Chain.** CERN 2004-003-v3, 1995/2004. URL: <http://ab-div.web.cern.ch/ab-div/Publications/LHC-DesignReport.html>.
- [31] L. EVANS AND P. BRYANT. **LHC Machine.** *J. Instrum.*, **3** (2008), S08001. 164 p. This report is an abridged version of the LHC Design Report (CERN-2004-003).
- [32] THE ALICE COLLABORATION. **Technical Proposal**, 1995.
- [33] THE ATLAS COLLABORATION. **Technical Proposal**, 1994.
- [34] THE CMS COLLABORATION. **Technical Proposal**, 1994.
- [35] THE LHCb COLLABORATION. **Technical Proposal**, 1998.
- [36] M.L.MANGANO(ED.) AND G. ALTARELLI(ED.). **Workshop on Standard Model Physics (and more) at the LHC.** Yellow report, 2000–2004, cern 2000, 1999.
- [37] O. ADRIANI ET AL. **The LHCf detector at the CERN Large Hadron Collider.** *J. Instrum.*, **3** (2008), S08006.
- [38] M. DEILE. **TOTEM: Forward Physics at the LHC.** hep-ex 0410084, Oct. 2004, URL: <http://arXiv.org/abs/hep-ex/0410084>.
- [39] THE CMS COLLABORATION. **CMS Physics Technical Design Report Vol II: Physics Performance.** CERN/LHCC 2006-021, June 2006.
- [40] THE CMS COLLABORATION. **The Tracker Project, Technical Design Report.** CERN/LHCC 98-6, Apr. 1998.
- [41] THE CMS COLLABORATION. **The Electromagnetic Calorimeter, Technical Design Report.** CERN/LHCC 97-33, Dec. 1998.
- [42] P. ADZIC ET AL. **Energy Resolution of the Barrel of the CMS Electromagnetic Calorimeter.** CMS Note 2006/148, Nov. 2006, CERN.
- [43] S. BANERJEE. **Simulation Geometry for the CMS HCAL.** CMS Note 2005/016, Sept. 2005.
- [44] THE CMS COLLABORATION. **The Hadron Calorimeter, Technical Design Report.** CERN/LHCC 97-31, June 1997.
- [45] D. FROIDEVAUX AND P. SPHICAS. **General-purpose detectors for the Large Hadron Collider.** *Ann. Rev. Nucl. Part. Sci.*, **56** (2006), 375–440.

- [46] THE CMS COLLABORATION. **The Magnet Project, Technical Design Report.** CERN/LHCC 97-10, May 1997.
- [47] THE CMS COLLABORATION. **The Muon Project, Technical Design Report.** CERN/LHCC 97-32, Dec. 1997.
- [48] I. FOSTER AND C. KESSELMAN. **The Grid: Blueprint for a New Computing Infrastructure.** Elsevier, 2004, ISBN 1-55860-933-4.
- [49] G. COWAN. **Statistical Data Analysis.** Oxford Science Publications, 1998, ISBN 0-19-850156-0.
- [50] T. SJOSTRAND, S. MRENNA, AND P. SKANDS. **PYTHIA 6.4 physics and manual.** <http://arxiv.org/pdf/hep-ph/0603175>, 2006.
- [51] S. AGOSTINELLI ET AL. **GEANT4: A simulation toolkit.** *Nucl. Instrum. Meth.*, **A506** (2003), 250–303.
- [52] C. ECK ET AL. **LHC computing Grid: Technical Design Report.** CERN-LHCC-2005-024, jun 2005.
- [53] THE CMS COLLABORATION. **The Computing Project Technical Design Report.** CERN/LHCC 2005-23, jun 2005.
- [54] **Qt Reference Documentation.** Oslo, Norway, 2004.
- [55] W. ADAM, B. MANGANO, T. SPEER, AND T. TODOROV. **Track reconstruction in the CMS tracker.** CMS Note 2006/041, Dec. 2005, CERN.
- [56] S. CUCCIARELLI, D. KOTLINSKY, AND T. TODOROV. **Position Determination of the Pixel Hits.** CMS Note 2002/049, Nov. 2002, CERN.
- [57] S. CUCCIARELLI, M. KONECKI, D. KOTLINSKI, AND T. TODOROV. **Track reconstruction, primary vertex finding and seed generation with the Pixel Detector.** CMS Note 2006/026, Jan. 2006, CERN.
- [58] F.-P. SCHILLING. **Track Reconstruction and Alignment with the CMS Silicon Tracker.** CMS CR 2006/061, Sept. 2006, CERN.
- [59] T. SPEER, K. PROKOFIEV, R. FRÜHWIRTH, W. WALTENBERGER, AND P. VANLAER. **Vertex Fitting in the CMS Tracker.** CMS Note 2006/032, Feb. 2006, CERN.
- [60] R. FRÜHWIRTH, P. KUBINEC, W. MITAROFF, AND M. REGLER. **Vertex reconstruction and track bundling at the LEP collider using robust algorithms.** *Computer Physics Communications*, **96** (1996), 189–208.
- [61] R. FRÜHWIRTH, W. WALTENBERGER, AND P. VANLAER. **Adaptive Vertex Fitting.** CMS Note 2007/008, Mar. 2007, CERN.
- [62] G. BRUNO, P. COX, S. LACAPRARA, N. NEUMEISTER, B. V. DE VYVER, S. VILLA, AND R. WILKINSON. **Local reconstruction in the muon detectors.** CMS Note 2002/043, Dec. 2002, CERN.

- [63] I. BELOTELOV AND N. NEUMEISTER. **Performance of the CMS offline muon reconstruction software**. CMS AN 2005/010, June 2005, CERN.
- [64] E. GATTI ET AL. **Analysis of the position resolution in centroid measurements in MWPC**. Nucl. Instr. and Methods 188, 327-346, 1981.
- [65] V. INNOCENTE ET AL. **GEANE, Average Tracking and Error Propagation Package**. CERN Program Library W5013-E, 1991.
- [66] E. JAMES, Y. MARAVIN, M. MULDERS, AND N. NEUMEISTER. **Muon Identification in CMS**. CMS Note 2006/010, Jan. 2006, CERN.
- [67] THE CMS COLLABORATION. **The Trigger and Data Acquisition Project, Volume I. The Level 1 Trigger, Technical Design Report**. CERN/LHCC 2000-38, Dec. 2000.
- [68] THE CMS COLLABORATION. **CMS High Level Trigger**. CERN/LHCC 2007-021, June 2007, CERN.
- [69] THE CMS COLLABORATION. **The Trigger and Data Acquisition Project, Volume II. Data Acquisition and High-Level Trigger, Technical Design Report**. CERN/LHCC 2002-26, Dec. 2002.
- [70] L. WILKE. private communication, Jan. 2008. Universität Zürich.
- [71] U. LANGENEGGER. private communication, June 2007. ETH Zürich.
- [72] B. M. DASSINGER, T. FELDMANN, T. MANNEL, AND S. TURCZYK. **Model-independent Analysis of Lepton Flavour Violating Tau Decays**. *JHEP*, **10** (2007), 039.
- [73] S. JADACH, B.F.L. WARD AND Z. WAS. **The Monte Carlo program KORALZ version 4.0 for lepton or quark pair production at LEP/SLC energies**. *Computer Physics Communications*, **79** (1994), 503–522.
- [74] S. JADACH, Z. WAS, R. DECKER, AND JOHANN H. KUHN. **The  $\tau$  decay library TAUOLA: Version 2.4**. *Computer Physics Communications*, **76** (1993), 361–380.
- [75] T. PIERZCHALLA, E. RICHTER-WAS, Z. WAS AND M. WOREK. **Spin effects in  $\tau$  lepton pair production at LHC**. <http://arxiv.org/pdf/hep-ph/0101311>, (January 2001).
- [76] R. SANTINELLI AND M. BIASINI. **First study of the CMS sensitivity to the neutrinoless decay  $\tau \rightarrow \mu^+ \mu^+ \mu^-$** . CMS Note 2002/037, Nov. 2002, CERN.
- [77] R. SANTINELLI. **Study of CMS sensitivity to neutrinoless tau decay at LHC**. *eConf*, **C0209101** (2002), WE14. <http://arxiv.org/pdf/hep-ex/0210033>.
- [78] M. RAIDAL ET AL. **Flavour physics of leptons and dipole moments**. <http://arxiv.org/pdf/0801.1826>, (2008).

- [79] L. PERCHALLA. **Leptonzahlverletzung mit  $\tau$ -Leptonen beim CMS-Experiment.** Diploma thesis, III. Physikalisches Institut B, RWTH Aachen, 2007.
- [80] E. NORRBIN AND T. SJOSTRAND. **Production and hadronization of heavy quarks.** *Eur. Phys. J.*, **C17** (2000), 137–161.
- [81] G. J. FELDMAN AND R. D. COUSINS. **A Unified Approach to the Classical Statistical Analysis of Small Signals.** *Physical Review D*, **57** (1998), 3873.
- [82] R. BRUN, F. RADEMARKERS, ET AL. **ROOT - An Object Oriented Data Analysis Framework, Ver. 5.20**, June 2008.

# Acknowledgment

The last words of this thesis are dedicated to all people that supported and encouraged me during the last years. In particular, I would like to thank:

- PROF. DR. ACHIM STAHL who gave me the opportunity to work in his CMS group on the interesting field of  $\tau$  physics. Thank you for your support and your trust during the past years.
- PROF. DR. MICHAEL KRÄMER for being the second referee of this thesis. Thank you for the calculations of the model independent matrix element of the  $\tau \rightarrow \mu\mu\mu$  decay.
- JIM KALLARACKAL and BENJAMIN O'LEARY, PHD for the calculations of the model independent matrix element of the  $\tau \rightarrow \mu\mu\mu$  decay, for answering all of my questions concerning the considered models and for proof-reading parts of this thesis.
- DR. THOMAS KRESS who always supported me during the last years. Thank you for all your suggestions and for proof-reading this thesis. In addition, you gave me also the opportunity to work on grid computing. Thank you very much.
- DR. HEIKO GEENEN and DR. MARC HENNING ZÖLLER for the introduction into limit calculation, for the fruitful discussions about my analysis and for answering all of my questions.
- DR. THOMAS HERMANN for patiently answering all my questions regarding physics. I really enjoyed our regular meetings on the golf course together with DR. ALEXANDER LINN.
- The remaining members of the Aachen CMS  $\tau$  Physics Group LARS PERCHALLA and PHILIP SAUERLAND. It was a pleasure to work with you.
- All my colleagues and former colleagues at the III. Physikalisches Institut B. It was pleasure to work with you and I always enjoyed the friendly atmosphere. In particular, I would like to thank DR. STEFAN KASSELMANN, DR. GORDON KAUSSEN, YVONNE KÜSSEL, DR. MICHAEL PÖTTGENS and DAISKE TORNIER.
- PROF. DR. URS LANGENEGGER who is the former convener of the CMS Heavy Flavour Physics Group and who always supported my analysis. Thank you very much.

- My family. Thank you very much for your everlasting support in all possible ways. Thank you for being with me.

# Lebenslauf

## Persönliche Daten

Name	Manuel Giffels
Geburtsdatum	18. Mai 1979
Geburtsort	Würselen
Staatsangehörigkeit	deutsch
Familienstand	ledig
Konfession	römisch-katholisch

## Schulausbildung

1985 – 1989	Grundschule Alsdorf-Ofden
1989 – 1998	Gustav-Heinemann-Gesamtschule Alsdorf
Juni 1998	Allgemeine Hochschulreife

## Grundwehrdienst

September –	Luftwaffenausbildungsregiment 1, Holzdorf
Oktober 1998	
November 1998 –	Luftwaffenwerft 81, Mechernich
Juni 1999	

## Studium

1999 – 2005	Physikstudium an der Rheinisch-Westfälischen Technischen Hochschule Aachen
Oktober 2001	Vordiplom in Physik mit dem Nebenfach Differentialgleichungen/Numerik und Informatik
Februar 2005	Beginn der Diplomarbeit mit dem Titel “Entwicklung der Auslesesoftware für den Kalibrationsteststand einer TPC” am III. Physikalischen Institut B der RWTH Aachen
März 2005	Diplom-Physiker mit dem Schwerpunkt fach Elementarteilchenphysik

## Promotion

Seit Mai 2005 Wissenschaftlicher Angestellter am III. Physikalischen Institut B der RWTH Aachen und Promotionstudium im Fach Physik

November 2007 – Aufenthalt am Europäischen Kernforschungszentrum  
Februar 2008 CERN in Genf als Mitglied der CMS Kollaboration

Seit Mai 2008 LHC-D Flavour Physik Convenor für CMS

08.01.2009 Einreichen des Promotionsgesuchs

27.02.2009 Mündliche Prüfung